



University of Pretoria

**DESIGNING AND DEVELOPING A FREE FALL ABSOLUTE GRAVITY
MEASURING SYSTEM USING PNEUMATIC ACTUATORS**

TLOU STEPHEN MOKOBODI

A DISSERTATION SUBMITTED TO THE FACULTY OF ENGINEERING, BUILT
ENVIRONMENT AND INFORMATION TECHNOLOGY OF THE UNIVERSITY OF
PRETORIA IN FULFILMENT OF THE REQUIREMENTS OF THE DEGREE OF
MASTERS IN MECHANICAL ENGINEERING

UNIVERSITY OF PRETORIA

2017



University of Pretoria

Author

Student : Tlou Mokobodi
Academic institution : University of Pretoria
Research institution : NMISA
Faculty : Engineering
Department : Mechanical Engineering
Student number : 29467013
E-Mail : u29467013@tuks.co.za

Advisers

Supervisor : Prof. Nicolaas Theron (University of Pretoria)
Co-Supervisor : Mr Pieter Greeff (NMISA)

2017

ABSTRACT

Title: **Designing and developing a free fall absolute gravity measuring system, using pneumatic actuators**

Supervisor: Prof. Nico Theron

Co-supervisor: Mr Pieter Greeff

Institution: University of Pretoria

Faculty: Engineering

Department: Mechanical and Aeronautical Engineering

Qualification: Masters of Engineering

A gravimeter is an instrument that measures gravitational force F_g (N) or acceleration g (m/s^2). Absolute gravity measurements are preferred in metrology, due to the shortest traceability links to the SI base units of length and time, realising acceleration. The investigation on the suitable method of gravity measurement was performed at the National Metrology Institute of South Africa (NMISA). The free fall gravity measuring system was adopted for development.

The metrological need on redefining the kilogramme standard using the watt balance, supported the decision to mandate this project. Free fall gravimeters were researched. The new concept of fully pneumatic controlled vacuum chamber was invented and manufactured. Pneumatic actuators were used on the vacuum chamber to align, launch, capture and reposition the falling test mass. Laser interferometer and high-speed digitiser with embedded accurate clock module, were used in realising displacement and time, through numerical computations. Using stabilised He-Ne Laser red with wavelength $\lambda=633$ nm interferometer, free-falling test mass displacements were traceable to length standard.

Interference intensity signal produced from experimental free fall drops were converted to A digital voltage signal enabling processing. Post signal processing algorithms were applied to the signal to extract the displacement and time coordinates of the free-falling object, using a zero-crossing detection method in a LabView environment. The final prototype setup measured the value 9.786041 m/s^2 with uncertainty of 0.0000705 m/s^2 at the vacuum pressure of 0.05 Pa. It was validated and compared with the Council of Geophysics' measured value of the site of 9.7860985 m/s^2 .

ACKNOWLEDGEMENT

I would like to acknowledge the following individuals for the continuous support provided during the period of the project:

- Prof. Nicolaas Theron for guidance provided throughout the project; in researching, designing, construction and testing of the prototype.
- Mr Pieter Greeff for guidance provided during the project, support in metrological application and the introduction to programmable logic controller in automations.
- Dr Abrie Oberholster for help provided in signal processing techniques.
- Dr Aletta Karsten for assistance provided on laser technology in theory and applications.
- Ms Faith Hungwe for support provided about laser optics and interferometry.
- Mr Oelof Kruger for providing constant support in design and construction of the prototype.

Special thanks:

- Mr Ian Veldman for providing constant support on interferometer setup and laser alignment process used in performing measurements.
- Mr Roko Popish, Mr Rudy Maruping and Mr Edwin Mohale for support provided in manufacturing the prototype.
- My language editor, Liza Marx from Academic and Professional Editing Services (APES) for her input, copy-editing and proofreading my work.

I would like to thank NMISA for the support provided ensuring that I complete the project.

TABLE OF CONTENTS

ABSTRACT.....	i
ACKNOWLEDGEMENT.....	ii
TABLE OF CONTENTS.....	iii
LIST OF FIGURES.....	vi
LIST OF TABLES.....	viii
CHAPTER 1 INTRODUCTION.....	1
1.1 Overview: Measurements and metrology.....	1
1.2 The history of human interest in gravity.....	2
1.3 Gravity measuring equipment.....	3
1.4 Discussions of gravity measuring methods.....	7
1.4.1 Relative gravimeters.....	7
1.4.2 Absolute gravimeters.....	8
1.4.3 Accuracies and application requirements.....	8
1.5 Development in NMISA.....	9
1.6 Study outline.....	9
CHAPTER 2 Free fall gravimeters: A literature review.....	11
2.1 Gravitational acceleration measurements in metrology.....	11
2.1.1 Force, pressure and gravity in metrology.....	11
2.1.2 Electromechanical balances and gravity in metrology.....	11
2.2 Free fall gravimeter.....	13
2.2.1 Direct free fall.....	15
2.2.2 Rise and fall.....	16
2.3 Fundamental governing equations of free-falling motion.....	17
2.4 Free fall systematic errors.....	19
2.4.1 Vacuum pressure.....	19
2.4.2 Electromagnetic fields.....	20
2.4.3 Test mass rotation and translation.....	20
2.4.4 Time delays associated with travelling light-wave.....	20
2.5 Interferometer.....	21
2.5.1 Light interference.....	21
2.5.2 Division of amplitude interference.....	22
2.5.3 Detector.....	28
2.6 Zero-crossing detection method.....	29

CHAPTER 3	Design and manufacturing of the prototype	31
3.1	Background.....	31
3.1.1	Electrical controlled actuators	32
3.1.2	Pneumatic controlled actuators.....	32
3.2	Overview: Pneumatic systems	33
3.2.1	Linear actuators	34
3.2.2	Rotary actuator	35
3.3	NMISA gravimeter.....	36
3.3.1	Conceptual design	36
3.3.2	Prototype design.....	37
3.3.3	Manufactured prototype	41
3.4	Test mass	42
3.5	System parameters and constraints.....	44
3.5.1	Dynamic parameters.....	44
3.5.2	Electronics capabilities.....	45
3.6	Intensity signal processing method	47
3.7	Systems requirements	48
3.8	NMISA DFFG-01 system components	49
3.8.1	Mechanical and pneumatics components	49
3.8.2	Pneumatic and electrical interface components	50
3.8.3	Electronics components.....	50
3.8.4	Vacuum pump station	50
3.9	Complete prototype system setup overview	50
3.9.1	System hardware setup	50
3.9.2	Sub-systems interface diagram.....	53
CHAPTER 4	Simulations.....	54
4.1	Simulation setup	54
4.2	Simulation results.....	58
4.2.1	Ideal gravitational acceleration calculation	58
CHAPTER 5	Prototype evaluations and results.....	59
5.1	Experimental procedure	59
5.2	NMISA DFFG-01 results	65
5.3	Results comparisons and validations	69
5.3.1	Universal gravity equation.....	69
5.3.2	Council for Geoscience gravimeter	69
5.3.3	CG-5 Autograv VS NMISA DFFG-01	70

5.4	System improvements	71
5.5	Prototype results discussions.....	76
CHAPTER 6 Conclusions and recommendation		79
6.1	Conclusions	79
6.2	Recommendations.....	80
6.2.1	Vacuum chamber pressure regulation and control	80
6.2.2	Mechanical improvements	81
6.2.3	Test mass improvement.....	82
6.2.4	Optical system improvement.....	83
6.2.5	Electronics and software	83
6.2.6	The Isolation system	84
REFERENCES		85
APPENDICES.....		89

LIST OF FIGURES

Figure 1-1: Pendulum gravimeter	4
Figure 1-2: First spring coil type gravimeter.....	5
Figure 1-3: Free fall gravity meter (Niebauer, 1995). (JILA)	6
Figure 1-4 : Superconducting gravimeters (Sachie, 2008)	7
Figure 1-5 : Accuracy of historical gravimeter designs (Torge, 1989)	9
Figure 2-1: The comparison graph of the kilogramme standard artefacts (LI, 2012)	12
Figure 2-2: Static phase experiment of the watt balance.....	12
Figure 2-3: Dynamic phase experiment of the watt balance.....	13
Figure 2-4: Rise and fall basic set up (Zabek et al., 2004)	17
Figure 2-5: Displacement and time graph for free-falling objects and gravitational acceleration models	19
Figure 2-6: Michelson interferometer optical configuration.....	25
Figure 2-7: Thin Film two beam interference geometry	26
Figure 2-8: Conceptual rearrangement of Michelson interferometer.....	27
Figure 2-9: Light intensity signal indicating frequency modulated signal.....	29
Figure 3-1: Pneumatic linear cylinder actuator	34
Figure 3-2: Semi-Rotary rack and pinion actuator	35
Figure 3-3: Pneumatic swivel cylinder actuator	35
Figure 3-4: Rotating vacuum chamber concept using pneumatic actuators.....	36
Figure 3-5: Vacuum chamber Solidworks model	38
Figure 3-6: Parallel gripper mechanism	39
Figure 3-7: The movement of the jaws during the gripping and releasing of the test mass	40
Figure 3-8: The gripper mechanism position during capturing of the test mass.....	40
Figure 3-9: The vacuum chamber with the stand indicating all mechanical components	41
Figure 3-10: Mechanical structure of the vacuum chamber of the developed gravimeters at NMISA .	42
Figure 3-11: Test mass: A, designed concept and B, Manufactured.....	43
Figure 3-12: Test mass with location of optical center OC_1 and OC_2 , and COM indicated	43
Figure 3-13: Photo-detector output signal (Baumann et al., 2015).....	46
Figure 3-14: System setup and electronics: A Hardware and B Electronics and Software	49
Figure 3-15: Vacuum chamber and structural stand.....	51
Figure 3-16: Optical table with Interferometer setup, extended to the vacuum chamber: A-The complete setup overview, B-Vertical laser beam alignment	51
Figure 3-17: NMISA DFFG-01 prototype setup [Partial sub-systems arrangements in A and B].....	52
Figure 3-18: NMISA DFFG-01 full sub-system integration network for measurement process control	53
Figure 4-1: Displacement of the test mass over the projectile period.....	56
Figure 4-2: Velocity of the test mass over the projectile period	57
Figure 4-3: Frequency of the light intensity signal over the projectile period.....	57

Figure 5-1: A: Interferometer optical setup and B: Produced intensity signal from the initial system setup	60
Figure 5-2: Second interferometer setup used on the NMISA DFFG-01, A: Polytec optical sensor head setup B: Produced intensity signal.....	60
Figure 5-3: Gravitation acceleration measured at different operating vacuum chamber pressure.....	64
Figure 5-4: Segments used in evaluating the effect of the signal frequency on the calculated gravitational acceleration and measurements standard deviation	66
Figure 5-5: Gravitational acceleration of set signals, analysed at different falling positions	66
Figure 5-6: Standard deviation of set signals analysed at different falling positions	67
Figure 5-7: Comparison of the three-processing method used on NMISA DFFG-01	68
Figure 5-8: Gravitational acceleration comparison graph with uncertainty measurements	70
Figure 5-9: Gravitational acceleration computed from intensity comparison of the USB and PXI	72
Figure 5-10: The displacement-time residual graph	73
Figure 5-11: Gravitational acceleration comparison graph with uncertainty measurements over changing operating pressure	74
Figure 5-12: Gravitational acceleration comparison graph with uncertainty measurements	75
Figure 5-13: CUSB and CPXI measured gravitational acceleration value and their standard deviation	76
Figure 5-14: Pressure comparison graph of actual measurements performed using the prototype and CPXI system setup with variation in pressure	77
Figure A-1: <i>Geometrical proof of optical path difference.</i>	89
Figure B-1: <i>Vacuum chamber positions</i>	92
Figure B-2: <i>Positions of the grippers without test mass.</i>	94
Figure B-3: <i>Positions of the grippers with test mass.</i>	95
Figure B-4: <i>A-Vacuum chamber, B- Deactivated knobs, and C- Activated knobs.</i>	97

LIST OF TABLES

Table 2-1: Force, pressure and gravity relationship (Ambaum, 2008)	11
Table 3-1: Advantages and disadvantages of electrical controlled actuators.....	32
Table 3-2: Advantages and disadvantages of using pneumatics actuators	32
Table 4-1: Intensity signal major properties	54
Table 5-1: Gravitational acceleration error calculation as a function of vacuum chamber operating pressure	63
Table 5-2: Gravitational acceleration measured whilst controlling the vacuum chamber pressure.....	64
Table 5-3: Gravitational acceleration measurements drops performed at 0.05 Pa pressure during day time on the isolation table	68
Table 5-4: Gravitational acceleration measurements performed at 0.05 Pa pressure during day time on the isolation table using PXI digitising card	74
Table 5-5: Performance specification	75
Table B-1: <i>Vacuum chamber components names</i>	90
Table B-2: <i>Position of Gripper 1 and 2 without test mass representation symbols</i>	95
Table B-3 : <i>Movement sequence of grippers without test mass</i>	95
Table B-4 : <i>Position of Gripper 1 and 2 with test mass representation symbols</i>	96
Table B-5: <i>Movement sequence of grippers without test mass</i>	96
Table B-6: <i>State representation of mechanical knobs for each gripper</i>	96
Table B-7: <i>Position of the vacuum chamber and state of the mechanical knobs</i>	98
Table C-1: <i>Motion parameters of the vacuum chamber as a function of time</i>	101
Table D-1: <i>Gravitational acceleration measurements drops performed in the atmospheric pressure during the day time without the isolation system</i>	102
Table D-2: <i>Gravitational acceleration measurements experimental drops performed in the atmospheric pressure during day time with solation system</i>	103
Table D-3: <i>Gravitational acceleration measurements experimental drops performed in the atmospheric pressure during night time with solation system</i>	104

CHAPTER 1

INTRODUCTION

Measurement is defined as “a number (information) used to relate a state of physical quantity to a particular reference physical quantity.” These quantities are therefore used to maintain control on the existence and development of all living creatures. Measurements are performed to guide organisms’ decisions and actions. This chapter provides the overview of the origin of measurements and scientific measurements, resulting in metrology, defined as scientific study of measurements. The significance of gravitational measurements and the impact of these systems on global development is discussed.

1.1 Overview: Measurements and metrology

According to the historians, the science of measurements dates to 3000 BC, when length measurements were performed, using body parts. Mass measurements were performed using stones, grains and balances. Volume measurements were accomplished with vessels, filled with grains and water. Periods of the sun, moon and stars measured time (Bucher, 2012). Time and length were the two measures and quantities of major interest. A rapid development is signified in the methods and systems used in performing their measurements. Different states globally used various types of measurement methods, resulting with difficulties in the global trade.

In the late 1600s, philosopher John Wilkins proposed using consistent decimal measurement system in England as universal system. This proposal led to inventing an international system of units, (SI), introduced in 1886. Gabriel Mouton (1690) proposed the metric system for measurements to standardise the measurement systems. Despite the 1690’s proposal, 1870 marks the year when standardised units of measurements, with the birth of scientific metrology, were globalised.

A conference was arranged in France for scientists’ representations from countries globally. In 1875 (Metre convention), a treaty signed by 17 countries during the committee establishment, providing the official recognition of the metric system (Francaise, 2009). Metre convention resulted from the formation of “*Bureau International des Poids et Mesures (BIPM)*” committee. The countries’ representatives’ agreement led to formulation of metrology committees.

The International Committee for Weight and Measures (CIPM) and General Conference on Weight and Measures (CGPM) committees were formed. The CIPM and CGPM were mandated to support the BIPM; the committees eventually led to the formation of National Metrology Institutes (NMIs).

In 1960 the CGPM defined and introduced the SI units and it was accepted. The SI units comprised seven base units by 1971, such as length, mass, time, electric current, temperature, volume of substance, and luminous intensity. Other fundamental quantities indicated, acceleration, velocity, force and density, forming the derived units linked to base units through mathematical formulation.

1.2 The history of human interest in gravity

The focus in this study is aimed at realising gravitational acceleration, represented by symbol 'g' in most scientific literature and the SI m/s^2 unit. The basic understanding of gravitational acceleration is described by phenomenon of gravity, which addresses the question of how all things are kept together in the universe. In the scientific fields, gravitational force F_g and g are often measured. These quantities relate to each other through mathematical equations. Gravitational force is scientifically defined as "a fundamental physical force field responsible for attractions between all the particles of matter to each other." Gravitational acceleration describes the rate of change of velocity of the objects, falling in the direction of the gravitational force. A brief history of gravity and its human interest is provided.

Realisation of gravity interested philosophers 2000 years prior to the 1500s when Aristotle questioned science behind falling objects (IPAC, 1986). The first scientific studies were performed, using practical experiments on free-falling objects by Galilei (1632). As Galileo commenced experimental investigations on free-falling objects, he discovered that objects of different mass free-falling under comparable environmental conditions, manufactured from the same material falls, signified the same velocity and acceleration. He could not provide mathematical and physical relations on these observations (Wolfram, 2002).

Sir Isaac Newton (in the mid-1600s) investigated planetary motions (work on relativity). At the end of the 16th century he explained free fall motion of objects, using mathematical and physical equations. The ability to present the observations by Galileo using physics and mathematics, gave Newton recognition for discovering gravity. Isaac Newton formulated the universal law of gravity as:

$$F_g = \frac{Gm_1m_2}{r^2} \quad (1-1)$$

where F_g is the force of attraction between the two particles, the universal gravitational constant G , $G=6.6725 \times 10^{-11} \text{ m}^3 \text{ kg}^{-1} \text{ s}^{-2}$, m_1 and m_2 are masses of Particle 1 and 2 attracting each other, and r

indicates the distance between the two particles. Newton's second law of motion is formulated as follows:

$$F = ma \quad (1-2)$$

where F is net force applied on the particle of mass m and the particle is accelerated by a , equations (1-1) and (1-2) are mathematically manipulated deriving the gravitational acceleration equation. The g is realised through distance and time measurements as indicated above. The unit Gal is universally used in the gravimetry field, honouring Galileo. One Gal is equivalent to 0.01 m/s^2 in SI units (Seigel, 1995; Schubert, 2007).

The scientific studies use gravitational force and acceleration in several scientific fields, due to their significance. Major scientific fields' functions such as metrology, geodesy and geophysics require in depth gravity knowledge (Marson, 2012; Schubert, 2007).

Gravitational acceleration knowledge in metrology is significant, because it enables the realisation of other derived standards, such as force and pressure (Wallard et al., 2006). The underway metrological project of redefining the standard SI base unit kilogramme, also perceived the essential need in g measurement, in supporting the watt balance (Li et al., 2012). In geodesy it is used for measuring and tracking the change in the shape of the planet, using change in gravitational force between locations globally. The morphology of the geoid within the planet can be studied using these measured differences. Geophysics is the study of the structure of the earth on the surface and subsurface. The gravitational measurements determine the shape and mass distribution of subsurface material minerals on the earth (Niebauer et al., 1992).

In developing research from various professional fields, scientists realised a need to measure gravity. Certain fields require measuring the F_g , relative gravity whilst certain fields require g , absolute gravity (Kryniski, 2012). Various methods are available in gravitational measurements. These methods include instrumentation devises and mathematical equations. The available methods attain various levels of measurement accuracies. This factor determines the method to use depending on the application (Torge, 1989).

1.3 Gravity measuring equipment

Methods of measuring gravity include: pendulums, spring coils, free fall and superconducting gravimeters. The basics of operational principles of these methods are provided:

Pendulum gravimeters

Pendulum gravimeters are absolute gravimeters in which the length L of the pendulum is accurately measured. The time is determined by measuring period T of the pendulum. The model of a simple pendulum is provided in Figure 1-1 and the mathematical formulation to determine g value is provided alongside.

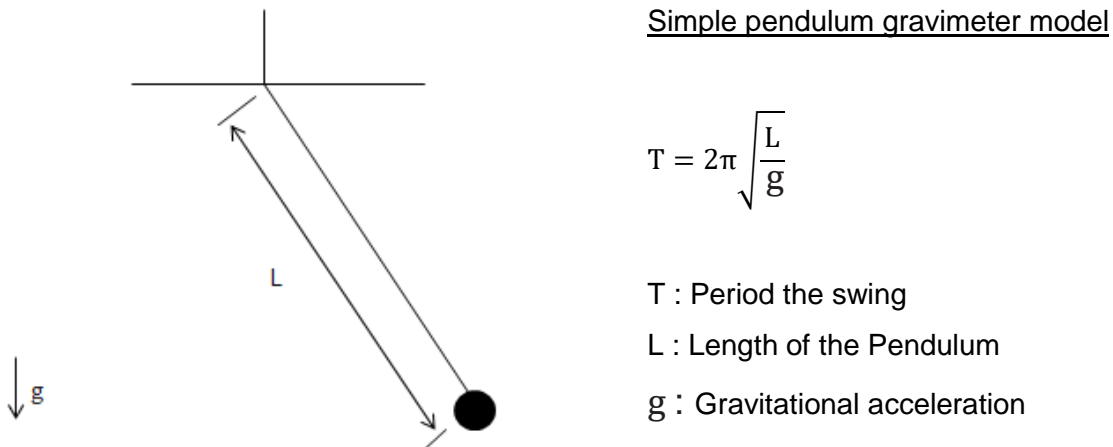
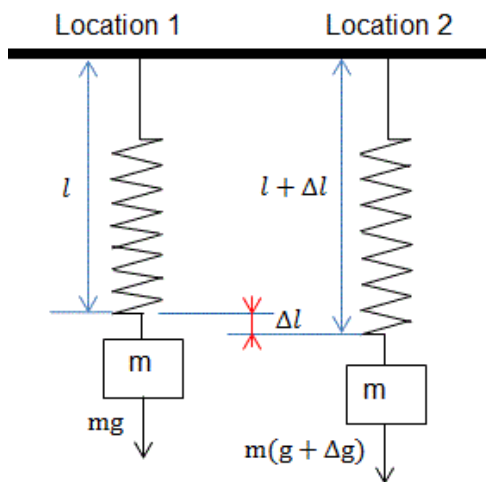


Figure 1-1: Pendulum gravimeter

The accuracy of the simple pendulum gravimeters is limited to 0.01 m/s^2 . This is due to the inaccurate methods used for measuring length and period of the pendulum swing. Henry Kater developed a reversible pendulum in 1818, improving measuring the length of the pendulum with the accuracy of measurements from 10^{-2} m/s^2 to 10^{-3} m/s^2 (Nabighian et al., 2005).

Spring coil type gravimeters

Spring coil type gravimeters are relative gravimeters. The principle of operation of this type of gravimeter follows Hooke's law on the elasticity of spring coil. The gravitational force at Location 1 balances the spring coil force. The equipment is moved to Location 2, performing similar tests. The elongation of the spring coil at Location 1 and 2 are compared to evaluate the change in length from Location 1 to Location 2. Relative gravimeters are easy to operate, because only length of elongation is measured. However relative gravimeters require the knowledge of absolute g of the reference location for comparison. Figure 1-2 indicates the principle of spring coil gravimeters.



Simple spring coil type gravimeter model

$$K\Delta x = mg$$

Figure 1-2: First spring coil type gravimeter

The spring coil force is used to calculate the force of gravity. The gravitational acceleration can be calculated through mathematical operations. The accuracy of the spring coil type method indicated $5 \times 10^{-6} \text{ m/s}^2$. The rate of measurements also increased, compared to the pendulum (Torge, 1989).

Lucien LaCoste invented a zero-length spring coil, improving the precision of spring coil gravimeters from $5 \times 10^{-6} \text{ m/s}^2$ to $5 \times 10^{-7} \text{ m/s}^2$ (Krynski, 2012).

The techniques in length and time measurement systems were advancing, with non-physical contact methods of length measurements, allowing new improved ways of measuring gravity with absolute gravimeters.

Free fall gravimeters

The free fall methods are absolute gravimeters. These instruments use the direct measurement of change in displacement and time, forming displacement-time coordinates of the free-falling object used with motion equations in computing free fall acceleration. The improved displacement measurements are referenced to the light wavelength, using principles of interference. Figure 1-3 indicates the typical setup of the free fall gravimeters comprising a dropping chamber, an interferometer and an isolation system.

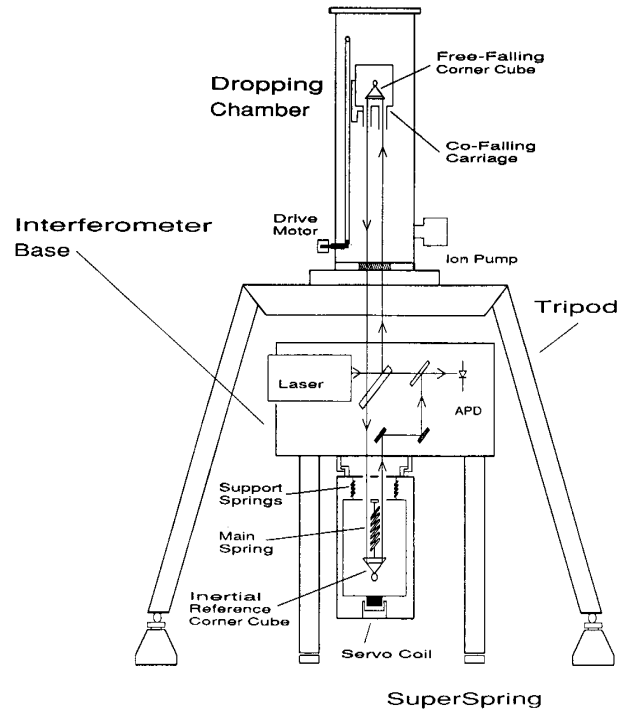


Figure 1-3: Free fall gravity meter (Niebauer, 1995). (JILA)

The accuracy of the free fall gravimeters improved detecting absolute g from 10^{-3} m/s^2 of pendulum gravimeters to 10^{-9} m/s^2 . The method of measurements using free fall gravimeters, is preferred in metrology, above the invented gravimeters. It provides direct measurements of two fundamental base SI units in deriving acceleration.

Studies of superconducting materials also advanced, resulting inventing new spring coil types with non-physical contact, improving relative gravimeters significantly.

Superconducting gravimeters

Superconducting gravimeters are relative gravimeters. They use the principle of the spring coil type gravimeters. Levitation is used as a non-contact spring, replacing mechanical spring coils used in spring coil type gravity measurement systems (Sachie, 2008). Figure 1-4 indicates schematic cross sections of superconducting mass with sphere, held by levitation coils (Hinderer et al., 2007).

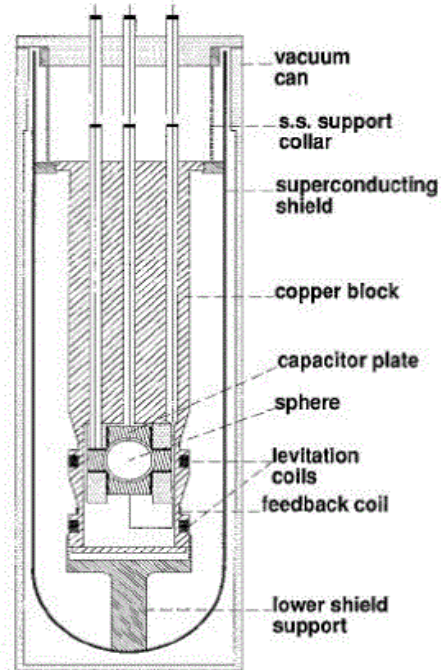


Figure 1-4 : Superconducting gravimeters (Sachie, 2008)

The superconducting gravimeters' design improved the accuracy of the relative gravity measurements from $5 \times 10^{-6} \text{ m/s}^2$ of the zero-length spring coil gravimeters, to $1 \times 10^{-10} \text{ m/s}^2$.

1.4 Discussions of gravity measuring methods

1.4.1 Relative gravimeters

Mechanical spring coil are used to construct the spring coil type gravimeters, suspending the test mass during the experiments. Major technical difficulties encountered with spring coil type gravimeters are mainly on the mechanical properties variation, associated with the spring. The properties of the spring coil changes with the environmental conditions and with the period of use (Dicke et al., 1969). These variations are difficult to account for in modelling and calculating the systematic error compensations, due to their random distribution behaviour (Ando & Carbone, 2009).

The superconducting gravimeters induced the solution to the major difficulties on mechanical spring coil type gravimeters. The test mass in the superconducting gravimeters are suspended using levitation. The electric current provides magnetic field, suspending the test mass. The operating temperature could be controlled to less than 10 Kelvin, allowing stable magnetic field production, achieving adequate levitation control (Hinderer et al., 2007). This instrument recorded the limitations of the superconducting gravimeters to be minimal. However these types mostly suffer

unstable random tare when moved between locations (Schubert, 2007). Relative gravimeters are generally precise but inaccurate.

1.4.2 Absolute gravimeters

The absolute gravimeters measures g with shortest traceability chain to the SI base units (Cook, 1965). In pendulum gravimeters, vibrations of the system and mechanical resistance of the pivotal point of the pendulum are the sources of major errors on measurements (Meyer, 2006). Developing non-contact length measurements, using light wavelength, resulted in a robust way of measuring gravity with direct measurements of time and distance (Rothleitner et al., 2014). The free fall gravimeters of non-contact measurement became the most preferred method of measuring gravity. Absolute gravimeters are generally precise and accurate, and do not suffer instrumental drift. Base SI units of length and time are used. Superiority of absolute over relative gravimeters indicates that measurements hold the shortest traceability for SI based standards (Niebauer, 2007).

1.4.3 Accuracies and application requirements

Gravity knowledge is required in various fields of gravimetry application, with certain levels of accuracy and uncertainty. The variation in gravitational acceleration between locations is mostly required in fields of geodesy and geophysics, enabling their functions; relative measurements are used.

In metrology, gravitation measurements knowledge is required with uncertainty less than 10^{-6} enables the duties in the force and pressure laboratories. The redefinition of a kilogramme standard project requires the knowledge of absolute gravitational acceleration with uncertainty of 10^{-9} or less, to enable mass measurements. Figure 1-5 indicates the uncertainty of measurements of major recognised gravimeters designed invented from 1800s to 2000s.

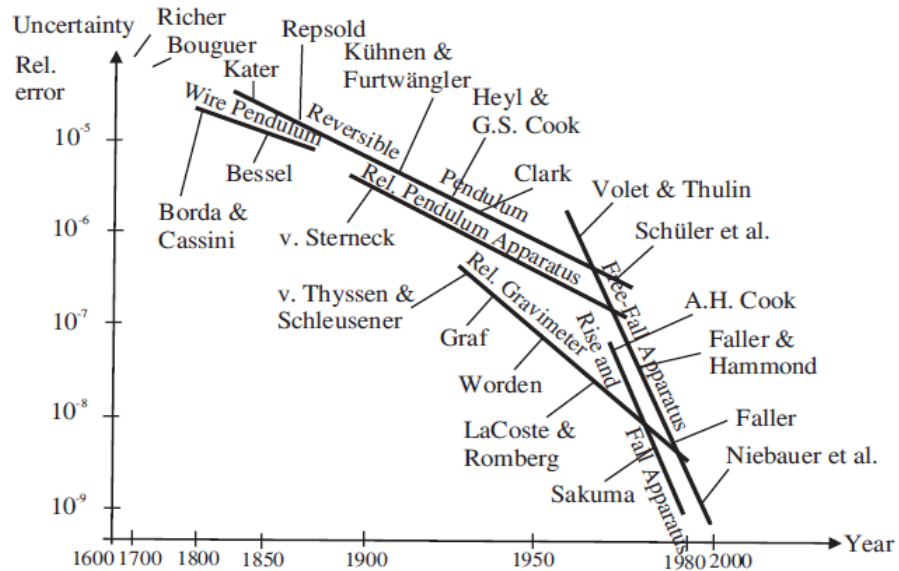


Figure 1-5 : Accuracy of historical gravimeter designs (Torge, 1989)

1.5 Development in NMISA

The absolute gravimeters are directly traced to the base SI units of time and length. The derived SI unit of acceleration is calculated directly from these two base units. Using improved accurate displacement detection and time keeping electronics methods, would impact the determination of the gravitational acceleration directly.

NMISA is tasked with two important missions in the metrological society: measuring to ensure traceability to SI units and continuously improving the measurement systems. Developing free fall gravimeter for gravitational measurements within the organisation was investigated to form part of continuous improvement of measurements' capabilities at the NMISA. This development aims to support the force and pressure standards transfer laboratories, and to form a close integral of the watt balance project underway at NMISA. Free fall gravimeter prototype was designed at NMISA. This study discusses the investigated, designed, constructed and tested prototype.

1.6 Study outline

This document reports the work accomplished on a fully pneumatic powered mechanical controlled gravimeter prototype, employing the direct free fall system setup. The prototype designed used a double-sided test mass prism, invented specifically to suit the functional procedure of the prototype. The design comprises a new concept proposed for NMISA, indicating a rotating vacuum chamber,

used to reposition the test mass. The displacement measurement of the test mass is achieved using the traditionally method of light interference of a two-laser beam interferometer.

CHAPTER 1 discusses the brief history of measurements and metrology. Gravity measurement methods are presented above with various principles used in the application fields. CHAPTER 2 discusses the literature reviews on free fall gravity measurements systems. Details are provided on the advantages and disadvantages between two inventions of free fall gravimeters: rise and fall, and direct free fall. CHAPTER 3 provides the design process of the NMISA gravity metre. The test mass handling mechanism is described, including the details of the rotating vacuum chamber, launching mechanisms and test mass reposition method. A detailed functional procedure used on the proposed mechanisms is provided in Appendix B. CHAPTER 4 describes evaluating numerical simulations of gravitational computations algorithms used and simulation results. CHAPTER 5 details the results, measurements of the NMISA gravimeter prototype experimental tests are analysed, using the algorithms from the simulation of CHAPTER 4. CHAPTER 6 discusses the prototype performance, conclusion on the findings and recommendations for future work on this project subject.

CHAPTER 2

Free fall gravimeters: A literature review

Gravitational measurements in metrology are significant in calibration of force and pressure equipment. NMISA designed and developed free-falling gravity metre prototype within the organisation to evaluate the possibilities of developing a system to serve as the standard of gravity, and for calibration of industrial applications. This project also supports the organisational responsibilities, current and future strategic plans. A newly invented method of controlling the test mass on a direct free fall gravimeter is designed.

2.1 Gravitational acceleration measurements in metrology

The gravitational acceleration measurements in metrology are used in mass calibrations equipment, force and pressure calibrations. The underway watt balance project requires the knowledge of the gravitational acceleration g for mass measurements.

2.1.1 Force, pressure and gravity in metrology

Pressure and force are closely related physical quantities. Pressure is defined as force applied over a surface area. In metrology, load cells provide force for calibration of pressure and force measuring equipment. Table 2-1 provides the role of the local g in realisation of force using mass of the load cells. Mathematical relationships between force, pressure and g are provided (Ambaum, 2008).

Table 2-1: Force, pressure and gravity relationship (Ambaum, 2008)

Gravity (g) and force	Force and pressure
$F = mg$ [N]	$P = F/A$ [N/m ²]
F- Force (Weight) m-Mass g –Gravitational acceleration	P -Pressure A –Area

2.1.2 Electromechanical balances and gravity in metrology

The standard of mass kilogramme is defined, using an artefact stored in Paris, BIPM, signifies a master reference. The duplicates of this artefact are distributed to several NMIs, including NMISA. Since the 1880s, the replicas are measured and compared to the master reference kilogramme and

to each other. Over a period, noticeable drift are noticed on the mass pieces compared. The comparison of national prototypes indicates relative drifts of a few parts in 10^8 with a variance of order of a few parts in 10^7 (Stock, 2011). Figure 2-1 specifies the drift graph.

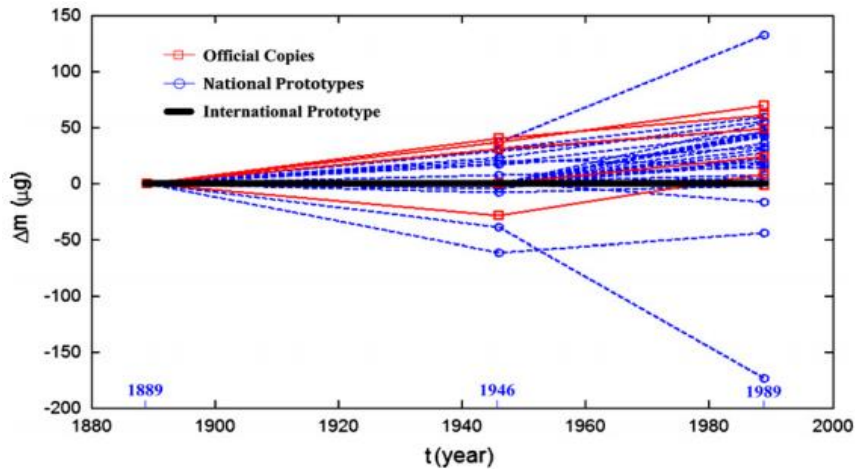


Figure 2-1: The comparison graph of the kilogramme standard artefacts (LI, 2012)

The watt balance is proposed as a solution to replace artefacts for standard of mass definition (Schlamminger et al., 2015). The balance uses equilibrium of electrical force F_E and mechanical force F_M (Geneves , 2006). In watt balance experiments, two phases of experiments are performed: static and dynamic phase (Sanchez, 2014). Figure 2-2 indicates a basic static phase experimental setup with simplified mathematical models governing the experimental setup.

Static phase

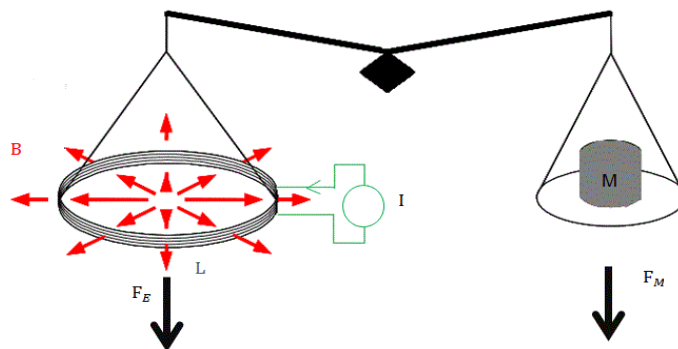


Figure 2-2: Static phase experiment of the watt balance

The electrical force and mechanical force are balanced in the static phase of the watt balance. At the equilibrium of the balance the two forces F_E and F_M are equal, which can be represented as:

$$BLI = mg \tag{2-1}$$

Dynamic phase

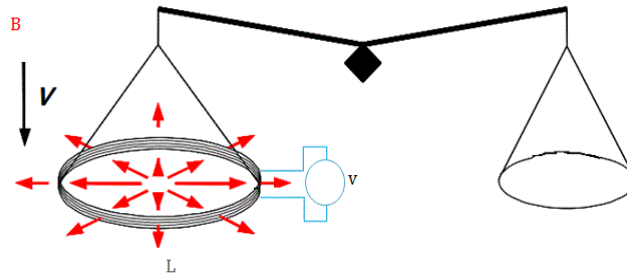


Figure 2-3: Dynamic phase experiment of the watt balance

In the dynamic phase of the experiment, the mass is removed from the balance, the coil is moved in the same magnetic field flux B with a constant velocity V . The output voltage v is measured accurately at the position of the equilibrium, position measured from the static phase. Figure 2-3 indicates the principle of mechanical balance set up for the dynamic phase.

$$v = BLV \tag{2-2}$$

Static phase	$BLI = mg$	g - Gravitational acceleration, m –mass, L -wire length of the coil, B - Magnetic density flux and I current.
Dynamic phase	$v = BLV$	V - Velocity and v -Voltage

The two experimental results are combined by solving the BL term in Equation (2-1) and (2-2). The mass used in the static phase experiment is calculated by using the resultant equation of the two phases of the experiment:

$$m = \frac{VI}{vg} \tag{2-3}$$

2.2 Free fall gravimeter

Free fall gravimeters measure the absolute g at the location of interest, with time and displacement coordinates of the free-falling test mass. In this application method, a free-falling test mass under the gravitational force field is tracked and traced. The displacement-time coordinates history travelled are accurately analysed, deriving the g value (Schubert, 2007).

Free fall gravimeters use interferometry to detect gravitational acceleration; optical and atomic interferometry. In Atomic free fall gravimeters, cold ^{87}Rb atom is used as a free falling object (Gillot

et al., 2009). In optical free falling gravimeters, an optical test mass is used. For the scope of this work, absolute free fall gravimeters will refer only to optical interferometer free falling gravimeters.

Absolute free fall gravimeters were invented in the mid-1900s. Inventing these types of measurement equipment took advantage of the availability of support measurement methods of systems, such as vacuum space generation, displacement measurements systems, time keeping and signal processing methods using digital electronic devices.

The improvements and developments of these methods of measurements are focused on precision and accuracy. The focus is guided by continuous accurate measurements requirements from the fields of applications (D'Agostin, 2008). Various systems are developed by different institutions with distinct operational characteristics. However the designs hold core similar components considered system requirements for the free fall gravimeters. The improvements of this equipment are directed to these sub-systems components, contributing to the overall system improvement (Niebauer et al., 1992; Schubert, 2007).

Free fall gravimeter sub-systems or components are: test mass, vacuum chamber, isolation platform, interferometer and support electronics components. Integrating these components enables the functionality of the system. The functions of each of these components are discussed.

Test mass

In free-falling gravimeters, a test mass is a piece of mass mounted with an optical reflector to form a single mass piece unit. The test mass is launched to fall freely under the influence of the gravity inside the vacuum chamber. The reflector enables the measurements performed by the interferometer using interference (Section 2.5). The reflector is protected by the test mass body against external contacts, impacts and contamination during the test mass handling.

Vacuum chamber

The primary function of vacuum chamber is providing space, enabling vacuum space. The vacuum space is a requirement in free-falling experiments, enhancing the reduction of air resistance on the falling mass. The vacuum chamber also serves as a mounting platform for the test mass controlling mechanisms. The design of NMISA free fall gravimeter prototype focuses on the vacuum chamber with a distinct method of launching and reposition of the test mass. CHAPTER 3 details the full design process of the prototype.

Isolation system

The isolation system is used to isolate the reference reflector from seismic and human induced vibrations that can affect the movement of the reference mirror during experiments. The interferometer in the measurements uses two reflectors, stationary reference reflector and moving reflector, test mass. The moving reflector is placed the vacuum chamber.

Interferometer

The interferometer is the sub-system comprising the optical setup constructed, using laser light and an arrangement of optical components, enabling its functionality. Laser source provides laser beam, and optics provides direction path for the laser beam. This sub-system enables displacement measurements of test mass during experiments, using light wavelength as reference. Section 2.5 presents more detail on the interferometer with the principles of light interference, performing the measurements. This sub-system forms the central integral interface supporting electronics, the falling test mass within the vacuum chamber and stationary reference mirror mounted onto the isolation system are coupled by the interferometer. The interferometer links physical actual measurements of falling test mass to the electronic signals, enabling digital processing.

In free fall gravimeters, two different system setups are used to perform free fall experiments, indicating direct free fall, rise and fall free fall setup (D'Agostino et al., 2007). They both use free-falling test objects measuring g through displacement and time measurements.

The components discussed, serve an identical purpose in both setups. The operating procedure of the two setups varies in launching, repositioning and aligning of the test mass. The direct free-falling setup method drops the test mass from high elevation, releasing the test mass, capturing it at the end of the flight at lower elevation. The rise and fall method launches a projectile upward and capture the projectile after the flight –same elevation for launching and capturing (Faller & Marson, 1988).

2.2.1 Direct free fall

The direct free fall absolute gravimeters refer to the setup which the test mass launched by dropping the test mass. The launching mechanism gently detaches from the test mass, allowing the test mass free fall. The aim is to release the test mass without resultant force on test mass, whilst ensuring test mass is aligned with gravity plumb line and with the laser beam. After the release, only gravitational force must act on the test mass as weight. The test mass is launched and

captured respectively, at the upper and bottom side of the vacuum chamber. Figure 1-3 indicates the general setup of the direct free fall method (CHAPTER 1).

Advantages associated with direct fall compared to the rise and fall method are: the mechanical design is simplified; the automation of the gravimeter system is relatively easily achieved in this process; and reduced human interaction to the system is achieved.

The disadvantage of the direct free fall method indicates the air resistance error arising with this setup (Bell et al., 1973; Cook, 1965). However, with the continuous improvements in the vacuum pumping techniques, the pressure level of 10^{-4} Pa or less was reported with minimum effect, or with negligible effect on the accuracy, providing this setup preference (Alasia et al., 1982; Zumberge et al., 1982).

2.2.2 Rise and fall

The rise and fall absolute gravimeter uses a setup where the test mass is launched up and captured after undergoing free fall –launching mechanism is mounted at bottom side of the vacuum chamber. The test mass separates from the launching mechanism with initial velocity, reaching the peak height and falls back to the launching mechanism where it is captured.

During launching instant, the test mass must be launched precisely in the gravitational plumb line. When the test mass reaches the apex position, it must drop down on the same path taken during up-rise movement. Interferometer measurements require highly accurate and precision control, also enabling capturing the projectile by the launching mechanism. Figure 2-4 indicates the diagram signifying a schematic rise and fall gravimeter.

The advantage associated with a rise and fall method, is that it does not suffer air drag resistance errors. The drag induced time delays are observed in both directions, cancelling when the gravitational force is analysed. In the up-rise motion, the drag slows the projectile in the gravitational force direction. In the downward motion, the projectile is slowed down in the direction opposite from the gravitational force. (Faller & Marson, 1988; Hammond, 1970; Schubert, 2007). The errors due to velocity delays are also minimised (Cook, 1965).

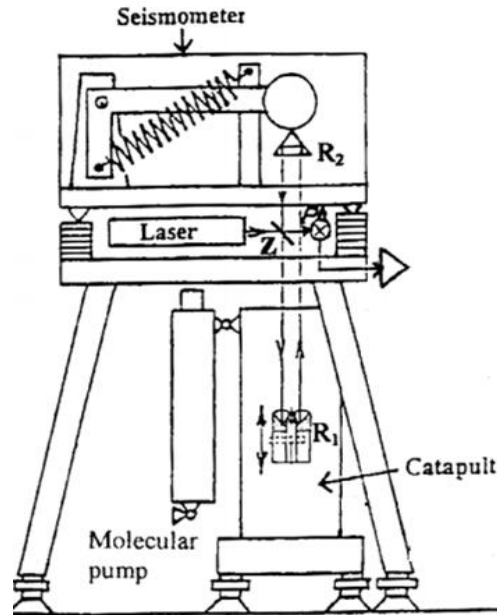


Figure 2-4: Rise and fall basic set up (Zabek et al., 2004)

The disadvantages of the rise and fall gravimeters limiting the usage of this method, is due to mechanical design difficulties of the launching mechanism. Another disadvantage indicates the chances of misaligning the test mass with gravity plumb line, increases in this method during the flight (Gualini, 2002).

2.3 Fundamental governing equations of free-falling motion

Newton's laws of motion are applied to free fall motion of the test mass, enabling acceleration calculation (Torge, 1989). The derivation of the free fall acceleration model is indicated. The acceleration of the test mass is purely assumed to be unidirectional in the gravitational plumb line with the displacement provided as z :

$$m\ddot{z} = mg \quad (2-4)$$

where $\ddot{z} = d^2z/d^2t$ represents the acceleration of the test body towards the centre of the earth.

The displacement and time are accurately measured by principles of interference of light using interferometer and with electronics components, supporting the interferometer. To compute g , Equation (2-4) is integrated, deriving the displacement profile of the test mass as a function of time.

The objects near the centre of the earth holds a higher g compared to the objects far from the centre of the earth, due to gravitation gradient. By integrating Equation (2-4), the displacement

mathematical model derives Equation (2-5) (Niebauer et al., 1995). The equation of motion governing free fall objects in nonhomogeneous gravitational field is:

$$z(t) = z_o + \dot{z}_o t + \frac{g_o}{2} t^2 + \gamma \left(\frac{1}{2} z_o t^2 + \frac{1}{6} \dot{z}_o t^2 + \frac{1}{24} g_o t^2 \right) \quad (2-5)$$

where $t, z(t), z_o, \dot{z}_o, g_o$ and γ represents time(s), distance travelled over time (m), Initial displacement at $t = 0s$, Initial velocity at $t = 0s$, gravitational acceleration (m/s^2) and gravity gradient ($m/(s^2m)$) respectively.

The free fall model of Equation (2-5) is simplified by letting the gravity gradient term be zero, with assumption that the falling height of the free fall is a homogeneous field and a gradient term. It has an insignificant or unnoticeable effect on the gravitational acceleration measurements. The acceptable value of gravity gradient is $3 \mu ms^{-2}/m$ (Torge, 1989). The gravitational acceleration model to be used in the analyses of the results of this project is the simplified mathematical model, because the prototype designed has a total falling length of less than 0.3 m and therefore the order of magnitude of its effect on the measurements is $0.9 \mu ms^{-2}$. Gravity gradient is further evaluated in section 5.2. The mathematical model reduces to:

$$z(t) = z_o + \dot{z}_o t + \frac{g}{2} t^2 \quad (2-6)$$

Two and three trajectory time-displacement coordinates are required for direct, and rise and fall free-fall gravimeters, respectively. The g is calculated using the following equations, rearranged form of Equation (2-6). The initial displacement and velocity of the projectile are taken as zero for direct free fall and at the apex point of the rise and fall (Torge, 1989; Cook, 1965; Bell et al., 1973).

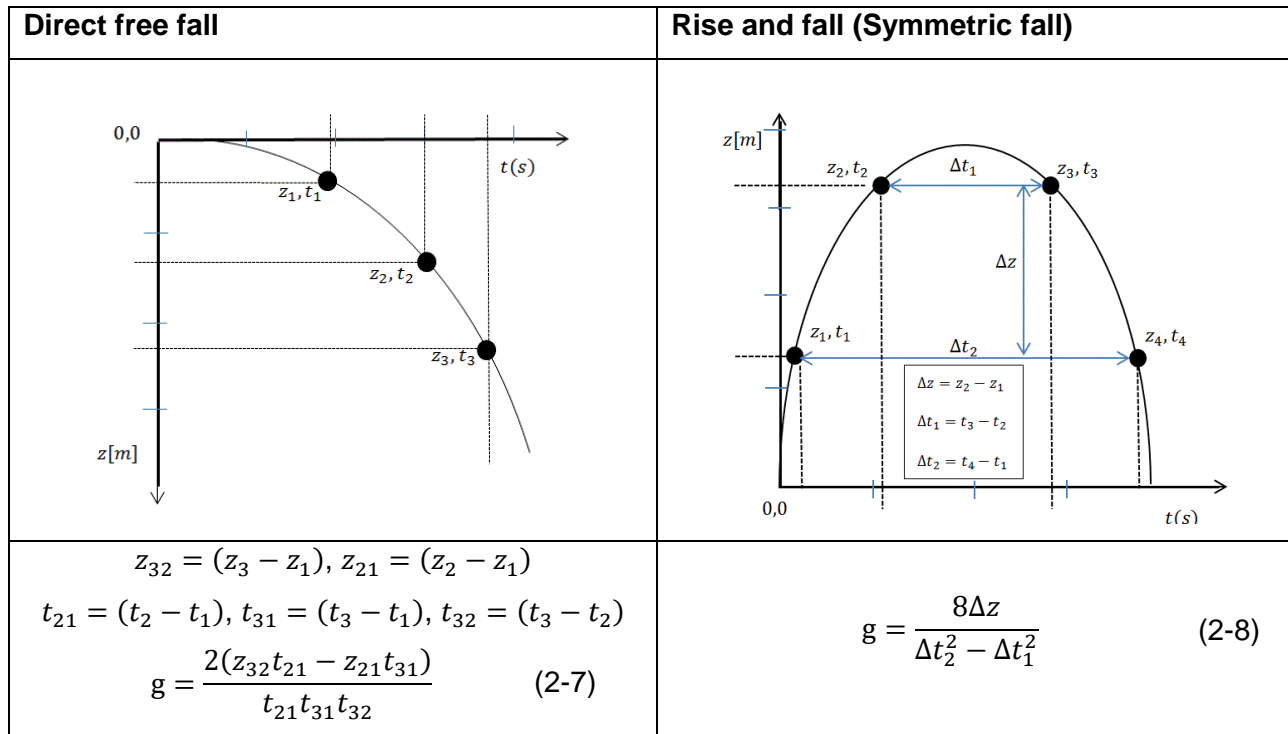


Figure 2-5: Displacement and time graph for free-falling objects and gravitational acceleration models

Comparing the two methods reveals that the accuracy and uncertainty budget indicated in both the setup are comparable. The two methods hold common systematic errors. Major focus on development is directed on these errors. Common errors found in both methods of free fall, are discussed in Section 2.4.

2.4 Free fall systematic errors

The systematic errors of the free fall gravimeters originate mostly from the major components discussed in Section 2.2. These are induced from the vacuum pressure, electromagnetic fields, laser system, supporting electronic components, test mass rotation and translation during the system operation. The systematic errors identified on direct free fall gravimeters are investigated in the report by Rothleintner (2008). The scope of this project does not cover the investigation of these errors on the prototype designed.

2.4.1 Vacuum pressure

The vacuum chamber is used in free fall gravimeters, providing a controlled space in creating vacuum pressure. Vacuum pressure is a requirement eliminating drag force effects on the free-falling test mass. This force depends on the falling velocity of the test mass and density fluid. The

ideal pressure requirements are absolute vacuum, 0 Pa, practically unattainable. However using turbo-molecular and molecular ion pumps, vacuum pressure resulting with negligible air resistant on the test mass is achievable.

2.4.2 Electromagnetic fields

Permanent magnetic or temporal magnetic field inducing components, such as vacuum pump motor and electric conductors around the vacuum chamber contribute to induction of magnetic fields. The electrostatic induced forces due to electric carrying conductors used in these systems, are reported to contribute towards this error. The removal of these components from the measuring system is an ideal solution required to reduction these errors.

The effect of magnetic force field depends on the distance between the source and the vacuum chamber. Placing the vacuum pump away from the chamber indicated great improvement in reducing the uncertainty errors from the magnetic field forces (Niebauer, 2007).

2.4.3 Test mass rotation and translation

The free-falling object is detached from the vacuum chamber during flight. Random rotations and translation movements are induced are mostly due to resultant forces from the launching mechanism. The accurate control of the test mass during launching point is significant in maintaining the orientation of the test mass during flight. The alignment of a test mass is a requirement in free fall gravimeters for the improved interference signal produced by the interferometer.

The factors affecting the motion of the test mass, include air resistance, time spent by the test mass in flight, magnetic forces and geometry of the mass. The method of test mass launching also determines the future motion of the test mass after launching (Faller & Marson, 1988).

2.4.4 Time delays associated with travelling light-wave

The speed of light has been realised to have errors which that be avoided. This must be corrected in the system to improve the accuracy of the system to reach the required accuracy of 10^{-8} m/s² (Rothleitner et al., 2014). Time difference between phase changes –test mass displacement – and the interference time is unavoidable, as the beam travels a certain distance between the two events. The mathematical background describing this error is discussed by Kuroda and Mio (1991). The gravitational acceleration measurements performed on JILA gravimeter with finite speed of light

accounted, indicated gravitational acceleration is measured lesser when the effect of light is not accounted for by $1.1 \times 10^{-7} \text{ m/s}^2$.

The errors discussed above are major contributors to systematic errors found in both the free fall gravimeter setups. The two methods each contain the advantages and disadvantages, guiding development on these methods, based on planned application and purpose for the development.

There are minor systematic errors found in certain designed free fall gravimeters. These errors in MPG-2 portable gravity metre include: laser verticality, accuracy and stability of the laser, laser beam divergence, clock stability, radiation pressure and temperature effect, floor recoils and seismic vibrations, reference height and non-linearity of electronics (Rothleitner, 2008; Rothleitner & Francis, 2010).

2.5 Interferometer

The interferometer is an instrument using light-wave interference, to perform accurate length measurements that are referenced to the wavelength of light (Hirai et al., 2014). In free fall gravimeter applications, accurate measurements of displacement must be achieved with nanometre accuracies. The interferometer applications in dimensional metrology are preferred due to their improved precision measurements and the direct traceability of the SI length standard. The interferometer is the instrument best suited in measuring nanometres displacement changes of motion of the test mass (Hecht & Zajac, 1974).

The white light source was used in developing interferometers from invention. Interferometers are now constructed using laser light due to superior characteristics compared to the conventional white light. This section explains the principles of interference phenomenon used in interferometry and how these apply to the free fall gravitational measurements (Durando & Germak, 2002; Niebauer et al., 1992).

2.5.1 Light interference

Superimposition of two waves combining to form a single wave scientifically explains principles of interference. Interference refers to the observed behaviour of the resultant wave. The interference discussed in this study, focuses on the laser light sources interferometers, in this study referred to as laser interferometers to distinguish the type of light source used. Laser light exhibits most characteristics of conventional light. It is also considered an electromagnetic wave (Hariharan, 2007; Davidson, 1991). Laser light is distinguished from conventional light because of its improved

properties over conventional light. These properties include, monochromaticity, directionality, high intensity and polarisation. (Dushkina, 2014).

Interference can occur when two or more waves originating from a single light source –dependant– or from multiple –independent– sources are superimposed. In interferometry applications, two or more light waves coming from a single monochromatic source, is mostly preferred. The coherence of these waves is important in observing the resulting wave (Davidson, 1991; Halliday et al., 1993; Born & Wolf, 2003).

Laser Interferometer uses comparison of light waves phases to perform measurements of very small displacements differences. The accuracy of the measurements depends on the light source wavelength used. He-Ne Laser light is mostly used for these applications, with the wavelength λ of 633 nm.

Thomas Young discovered this phenomenon, using the well-known experimental setup “Two slit interference”, demonstrating that light can be treated as a wave (Halliday et al., 1993; Steward, 2004).

Constructive or destructive interference can occur during interference, depending on the phase and amplitude of the two waves. The resulting wave carries the properties of the two waves combined. Numerous optical physics books detail the mathematical theory of wave interference as discussed by Young’s two slit experiment. These books include, Fundamentals of Physics by Halliday (1993) and Basics of Interferometry by Hariharan (2007). In this study, only the phenomenon for applying interest of this research is detailed.

Interference of light waves can occur in two ways: division of wave front and the division of amplitude interference (Born & Wolf, 2003; Hecht & Zajac, 1974). Interference by amplitude division is detailed as it is used in the interferometers found in free fall gravimeters.

2.5.2 Division of amplitude interference

In amplitude division interference, phase changes of two monochromatic coherence light waves originating from a single source are monitored. The original beam is divided into two beams and recombined after travelling separate paths. Consider a wave represented by E –electrical field of the electromagnetic wave– provided, propagating in space along displacement z in time t .

$$E(z, t) = a \cos[\omega t - kz] \quad (2-9)$$

Wave amplitude is provided by a , propagation constant $k = \frac{2\pi}{\lambda}$ and angular frequency $\omega = 2\pi\nu$ depended on frequency ν and the wavelength λ in the propagation constant definition is provided by $\frac{c}{\nu}$, with c representing wave propagating speed.

The complex representation of the wave equation is used to simplify mathematical manipulation:

$$E(z, t) = \text{Re} [a e^{(-i\phi)} e^{(i\omega t)}] \quad (2-10)$$

where: phase constant, $\phi = kz = \frac{2\pi z}{\lambda}$

Let $A = a e^{(-i\phi)}$ be complex amplitude

$$E(z, t) = \text{Re} [A e^{(i\omega t)}] \quad (2-11)$$

In amplitude division interferometers, optics are used to divide the amplitude of the laser beam from a single source into two beams that are directed back together to interfere. During interference, a visible light band fringes signal is formed; the light band signal repetitive bright and dark bands. Constructive and destructively interference of the involved two signals result in the bright band and dark band. Figure 2-6 below indicates a typical interferometer setup.

Fringe formation results due to phase difference of the two waves, resulting from the path difference between the two waves. A detector detects light intensity and converts the intensity distribution to an electrical –voltage– signal. An intensity signal links the wave properties of the interfering beams, which displacement measurements are achieved at using wavelength λ of light. Mathematical representation of intensity measured is discussed.

2.5.2.1 Light intensity

Intensity is a measure of light energy delivered over a unit surface area in unit time. The intensity referred describes the intensity of the resulting interference beam. After the beam is divided –using 50/50 beam splitter– into two identical beams, let each beam be represented by E_1 and E_2 . Each beam takes the propagation form of Equation (2-9). At the point of interference, using principle of superposition, intensity of the two waves is given by:

$$\begin{aligned} I &= |A_1 + A_2|^2 \\ &= I_1 + I_2 + 2\sqrt{I_1 I_2} \cos(\Delta\phi) \end{aligned}$$

where $\Delta\phi$ represents the phase difference or change between the two beams and, I_1 and I_2 represents the intensity of each beam, prior to interference.

The third term in the intensity is sinusoidal equation ranges from $(+2\sqrt{I_1I_2})$ to $(-2\sqrt{I_1I_2})$.

The equations provide the maximum intensity I_{max} and minimum intensity I_{min}

$$I_{max} = I_1 + I_2 + 2\sqrt{I_1I_2} \quad (2-12)$$

$$I_{min} = I_1 + I_2 - 2\sqrt{I_1I_2} \quad (2-13)$$

Phase difference of the two interfering waves ($\Delta\phi$) relates to optical path difference (ΔOPD) of the two laser beams by:

$$\Delta\phi = \frac{2\pi}{\lambda} (\Delta OPD) \quad (2-14)$$

The intensity graph observed is used to extract displacement history of the test mass. The two beams travel different paths; one beam travels to a stationary reflector –reference beam– and the other beam travels to the falling reflector –variable/measuring beam. The reference reflector is required to be at absolutely rest, thus ΔOPD result due to movement of only the measuring beam.

The interferometers used in free fall gravimeters are referred to as two beam interferometers; they require the reference and measuring beam to perform measurements. An interferometer can have multiple beams, depending on the number of axis of measurements. In free fall gravimeters only, z direction is the axes of interest, as gravity is assumed and restricted to be in a downward direction only, towards the centre of the earth. The two beam interferometers are then discussed.

2.5.2.2 Two-beam interferometers

The two-beam interferometers are used on the free fall gravimeters applications. Their interference occurs between two light beams, originating from a single source. The two beams travel different paths before they are conveyed together to interfere. The optical path difference of the two beams provides information about the path taken by variable beam. Coherence of the two beams is important at the superimposition site of the two beams, ensuring improved interference.

The basic two beam interferometers methods include Fizeau, Michelson, Mach-Zehnder polarisation and Sagac's interferometers. (Hariharan, 2007). The principle of the Michelson interferometer is used in the NMISA prototype gravimeter development because it comprises a simple optical components configuration. Figure 2-6 describes this configuration with the setup of a simple Michelson interferometer. The detail provide insight in achieving the measurements, using the "Thin film interference" method with amplitude division interference.

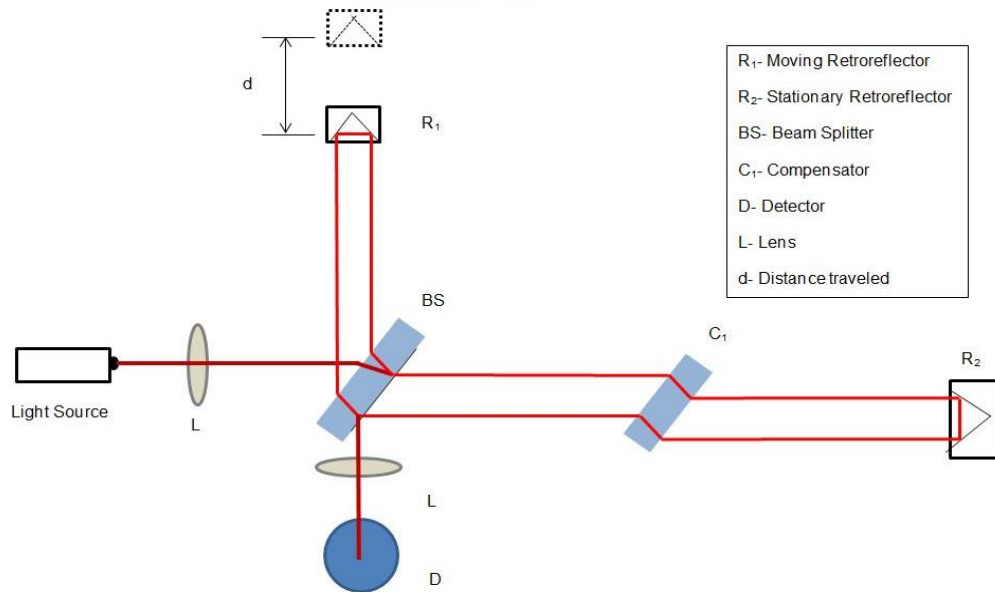


Figure 2-6: Michelson interferometer optical configuration

The basic Michelson interferometer setup comprises a light source, a beam splitter, a reference reflector, a variable reflector and an intensity detector. In free fall measurements, retroreflectors are preferred to traditionally flat mirrors. The retroreflectors retain superior functional advantage when the variable reflector movement is not constrained by physical guides. Using the retroreflectors ensures that the variable beam returns to the beam splitter to undergo interference, even when the falling test mass tilts with small angles during flight.

The 50/50 Beam Splitter (BS) divides the beam incident by light source into two ideally identical halves; One half travels to R_1 and reflects to the BS, and the other half travels to R_2 and reflects to the BS. C_1 is used to equalise the times each beam travels in the beam splitting materials. At the arrival of the two beams at the BS, they interfere as they superimpose. The resulting beam travels to detector D. Interference fringes are observed, stored and analysed. The fringes represent the intensity distribution of the resulting interfering superimposed beams (Hecht & Zajac, 1974).

The Michelson interferometer uses the fundamental phenomenon of thin film in amplitude division interference. The thin film interference theory is provided and the reconstruction configuration of the Michelson setup from thin film interference is discussed.

2.5.2.2.1 Thin film interference

Interference in amplitude dividing is well understood when demonstrated with a light-wave, that incident a thin film of liquid or transparent material of thickness d as indicated in Figure 2-7.

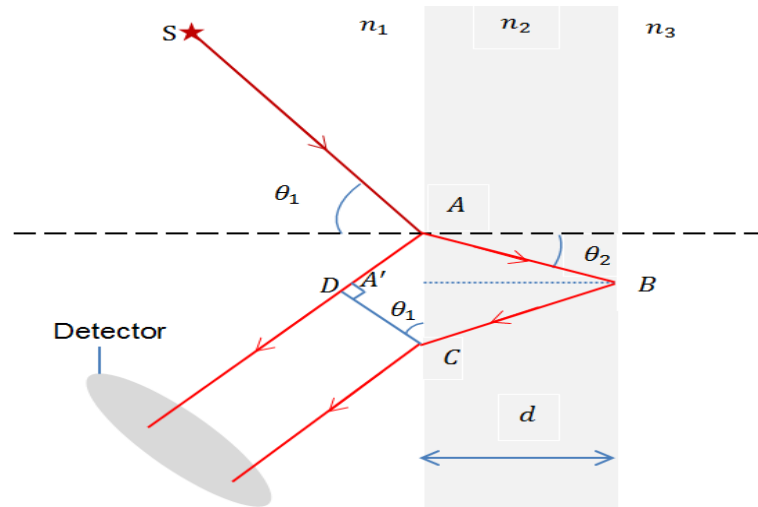


Figure 2-7: Thin Film two beam interference geometry

Thin film interference occurs by division of amplitude interference. The ability to measure phase difference, enables the computation of optical path difference as mentioned above. Optical path difference of thin film is geometrically calculated, using the equation (2-16). On Figure 2-7, the source S produces a light beam that falls onto the film at the point A; light is divided into two components refraction, A-B-C and reflection A-D:

$$\Delta OPD = n_2[AB + BC] - n_1[AD] \quad (2-15)$$

where n_i is the index of refraction of the medium the light beam is travelling through using the mathematical geometry and Snell's law of optical refraction and reflection:

$$\Delta OPD = 2 d n_2 \cos(\theta_2) \quad (2-16)$$

where d is the thickness of the thin film.

2.5.2.2.2 Michelson interferometer conceptual optical configuration

The Michelson interferometer produces interference fringes by using the concept of the thin film optical arrangement discussed in Section 2.5.2.2.1. The conceptual optical rearrangement is indicated in Figure 2-8. Assume an observer placed at the detector and observing the output beams from the BS –the point of interference, as indicated in Figure 2-6. The observer perceives the beam reflected by R_1 and R_2 simultaneously from BS as they undergo interference.

Consider the same arrangement with virtual image R'_1 of R_1 placed parallel with R_2 as indicated in Figure 2-8. Light source S produces monochromatic coherence beam reflected by retroreflector mirror R_2 and R'_1 . Observer observes the two-reflected beam as if they are produced by two virtual separated sources S'_1 and S'_2 . If the two retroreflectors R_2 and R'_1 are separated by distance d , then

$2d$ is the distance between virtual sources S'_1 and S'_2 , refer to Appendix A (Amrita, 2011). If the angle of incidence –angle between viewing axis and the light beam– of the light source is θ_2 , the optical path difference of the two beams from virtual sources S'_1 and S'_2 is

$$\Delta OPD = 2d \cos(\theta_2) \quad (2-17)$$

This equation is similar to Equation (2-16) above, when the index of refraction of medium is taken as 1.

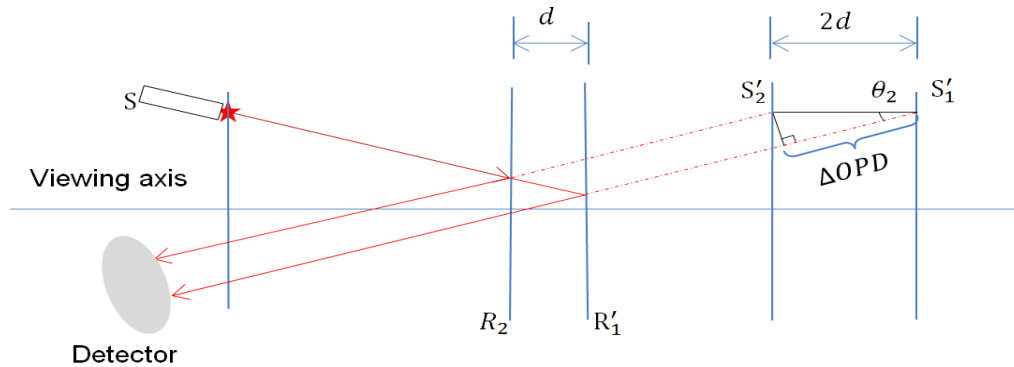


Figure 2-8: Conceptual rearrangement of Michelson interferometer

The two light beams interfere producing fringes of pattern bright (maxima) and dark (minima) light bands depending on the phase difference related to the optical path difference of the beams as discussed in Section 2.5.2.1.

2.5.2.3 Interference patterns of the Michelson interferometer

The phase change of the two beams determines the intensity distribution of the resulting beams. During constructive interference, the two beams are completely in phase and a bright fringe result with maximum light intensity. The total path interference is defined by:

$$OPD_T = m\lambda$$

During destructive interference, the two beams are completely out of phase with dark fringe and minimum light intensity. The total path difference defined by:

$$OPD_T = \left(m + \frac{1}{2}\right)\lambda$$

where $m = 0, 1, 2, 3 \dots$ an integer number of waves.

In Michelson interferometer arrangement indicated in Figure 2-6, the beam travelling from retroreflector R_2 undergoes reflection at the BS, the resulting phase change is π , corresponding to

path difference of $\lambda/2$ (Stokes treatment of reflection and refraction and Fresnel Formulae) combining OPD and $\lambda/2$ to obtain OPD_T .

Constructive Interference	Destructive Interference
$OPD_T = m\lambda + \lambda/2$ $2d \cos(\theta_2) = \left(m + \frac{1}{2}\right)\lambda$	$OPD_T = \left(m + \frac{1}{2}\right)\lambda + \lambda/2$ $OPD_T = m\lambda + \lambda$ <p>The term λ is a constant shift, therefore</p> $2d \cos(\theta_2) = m\lambda$

The interferometer setup is used for free fall gravimeters; the incident angle θ_2 is zero, $\cos(0) = 1$. Constructive and destructive interference occurs when $2d = \left(m + \frac{1}{2}\right)\lambda$ and $2d = m\lambda$ respectively. The phase change of the interfering light is provided by:

$$\Delta\phi = \frac{2\pi}{\lambda}\Delta(2d) \quad (2-18)$$

where Δd represents the change in displacement of the test mass R_1 over the falling height. In the two-arm interferometer with the setup indicated in Figure 2-6, the intensity of the resulting two beams is equal assuming perfect split of 50/50 BS. The intensity equation in Section 2.5.2.1: $I = I_1 + I_2 + 2\sqrt{I_1 I_2} \cos(\Delta\phi)$ becomes

$$I = 4 I_1 \cos^2\left(\frac{\Delta\phi}{2}\right) \quad (2-19)$$

The interfering beam is directed to a detector for the intensity distribution mapping. The photodetector is discussed in this study as one of the major components of the interferometer; this component is the entry component of the electronics components required in enabling signal acquisition of the intensity distribution (Baumann et al., 2015). This component is used to convert fringe signal into an electronic signal, then interpreted to extract test mass R_1 displacement history.

2.5.3 Detector

Interferometer is installed with the light detector that uses photodiodes for fringe signal mapping. Photodiodes are light sensing semiconductors which converts light intensity to electric signal when illuminated. During free fall experiments the intensity distribution of the resulting beam has a sinusoidal distribution signal. The resulting signal is a frequency modulated graph signifying the test mass velocity increase during the fall. The phase changes of 2π (consecutive bright and dark fringe bands) on the intensity graph mapped by the detector as an electrical signal correspond to the change in displacement of $\lambda/2$ of the test mass. An analogue to digital card is used to digitise the

signal at constant sampling frequency enabling digital signal processing for further computations. The digitising card is locked to reference time to allow real time stamping of the samples of the mapped signal.

The resulting signal is analysed to obtain an accurate change in displacement between the two beams, using a well-known method of zero-crossing detection (Hirai et al., 2014). An example of electrical signal produced by an ideal free-falling object is indicated in Figure 2-9. The maximum voltage of the signal corresponds to bright band of the fringe signal, whilst the dark band corresponds to the minimum voltage of the signal.

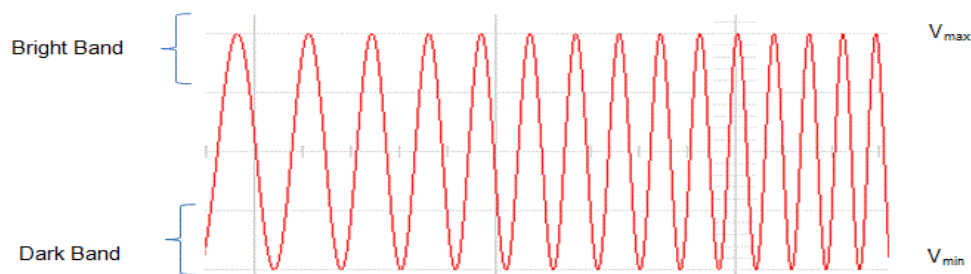


Figure 2-9: Light intensity signal indicating frequency modulated signal

2.6 Zero-crossing detection method

The zero-crossing detection method is a signal processing method that detects the points where the signal crosses the zero-voltage line. This line represents the average intensity value produced –the stage where the fringe intensity changes from dark to bright band. In free-falling gravimeter experiments, it is required to accurately map the voltage signal produced during the fall. This is required enabling accurate detection of the zero-crossing sites of the signal used in test mass displacement mapping.

The ability to detect these points improves the accuracy of mapping the flight history of the test mass directly. As the interferometer enables measuring displacement coordinates, the time coordinates are produced using a real time electronic digitiser.

The improvement in analogue to digital converters (ADC) technology in electronics, reduced the uncertainty budget of the gravimeter from usage of multiple electronic components to a single module (Baumann et al., 2015). The detector explained above, produces a continuous analogue distribution, discretised into a digital signal, using ADC.

The ADC cards are locked to standard of time using high accurate clocks internally. When the experiments are conducted, at the moment of release of the test mass, the ADC is triggered to stamp the time coordinates of the signal corresponding to intensity detected. Each voltage sampled from the analogue intensity signal is provided a sample index number or time stamp, locked to the sampling frequency of the digitiser. The capabilities of the ADC card, that is sampling rate and module time resolution, directly affects the accuracy of the produced data. The signal is reproduced with real time value, allocated to each voltage digit. Each voltage digit is associated to an intensity data point.

The data extracted from ADC is in the form of time-voltage coordinates. Through data manipulation with set reference, all the voltage values above and below the zero-line voltage are assigned positive and negative signs respectively (Svitlov et al., 2010). The zero-voltage data points of signal are detected by searching the voltage coordinates data for sign change of the sign. When the signal sign changes from positive to negative or from positive sign, the signal crossed the zero-line.

The time coordinates corresponding to the point of zero-crossing are stored. If the signal crosses zero-voltage line at non-sample point, linear interpolation is performed, determining the time of the cross. The time coordinates of the crossing points are stored after operating on the entire voltage signal. The displacement profile is reconstructed by addition of a constant of $\lambda/4$ every instant the signal crosses zero point. This operation results with a time and displacement vectors required to perform calculations of Equation (2-7) and (2-8) provided in Section 2.3 above to calculate the g . The zero-crossing method is the only method used, processing the prototype results.

CHAPTER 3 discusses the NMISA prototype design. The physical parameters are defined prior to the electronics modules parameterised. NMISA designed the new concept of measuring gravity, using direct free fall methods, guided by findings from studies performed on free fall gravity measurement systems. This concept uses pneumatic actuators for test mass launching, capturing and reposition mechanical systems. The system is designed, attempting to remove electrical conductors around the vacuum chamber to reduce the effect of electromagnetic force fields. CHAPTER 3 outlines the design and manufacturing process of this system. The NMISA prototype is named NMISA DFFG-O1 –this name used in this study, refers to the prototype at NMISA.

CHAPTER 3

Design and manufacturing of the prototype

An absolute direct free fall gravimeter measurement system was developed in this study, investigating the methods used to perform gravitational acceleration measurements. The prototype was designed, manufactured, constructed and tested. This chapter describes the prototype designed at NMISA in detail.

3.1 Background

The design of the NMISA DFFG-01 is centralised on the invented vacuum chamber mechanism. The vacuum chamber of the prototype is not rigidly stationed, compared to several existing designs, indicating that the vacuum chamber is permanently mounted on a stationary platform. Systems with such vacuum chambers setups are found on the gravimeters developed at JILA and BIPM.

Developing free fall gravimeter is concerned with the continuous development of supporting systems. Systematic errors identified on gravimeters directly links to the errors introduced by the support systems around the vacuum chamber.

The removal of the magnetic fields sources around the vacuum chamber was previously proposed as a method to improve the uncertainty budget on the JILA gravimeter (Rothleitner, 2008). The NMISA DFFG-01 is based on totally removal of the electrical power systems on the vacuum chamber introducing pneumatic power system control for mechanical movement of the vacuum chamber and the test mass. The two methods of control, electrical and pneumatic power systems, were reviewed and compared. The decision of the control actuators was based on the aspects discussed.

Designs of absolute free fall gravimeters require electronics control, allowing full automation of the system for improvement, by reducing errors caused by human interactions (Niebauer et al., 1992). Logic electronic communications of the dependent sub-systems components is important in implementing such measurement processes. The control power methods to be considered indicate the electrical and pneumatic actuators. Evaluating the two methods focuses on their advantages and limitations in selecting the method of control by evaluating the vacuum chamber concept. The method to use for system control depends mainly on the system requirements (Greenfield, 1999).

3.1.1 Electrical controlled actuators

Electrical control actuators are highly preferred due to a large range of applications and simplified control methods, using modulated electrical signals (Walfgang & Macdonald, 2005). Table 3-1 lists the advantages and disadvantages associated with the electric controlled actuators (Branan, 2002).

Table 3-1: Advantages and disadvantages of electrical controlled actuators

Advantages	Disadvantages
<ul style="list-style-type: none"> • Low installation cost • Lower maintenance cost • Higher positioning accuracy • Long distance operations • Digital control compatibility • Continuous movement 	<ul style="list-style-type: none"> • Constant subjection to corrosion • Subjects to electric interference • More difficult to provide for positive fail-safe operation • Magnetic field production • High design cost • Overheating in continuous operations • Continuous vibration during operations

3.1.2 Pneumatic controlled actuators

Pneumatics control systems are traditionally used on the open loop controls with extreme positions control, or hard stops for highly accurate positioning. Over the years, developing electro-pneumatic systems design enabled controlling pneumatic systems to obtain a high accurate motion with closed loops (Bosch, 2006). Using closed loop control system for pneumatic actuators, improved their use in several industrial and research applications (Ritola, 2014). Table 3-2 lists the advantages and disadvantages of pneumatics controls (Branan, 2002).

Table 3-2: Advantages and disadvantages of using pneumatics actuators

Advantages	Disadvantages
<ul style="list-style-type: none"> • Low maintenance • Smooth and precise control • Clean and environmental friendly • Higher accuracy with servo valves and high repeatability motions • Energy in the air can be stored and it is reusable • Zero magnetic field • Speed and force control • Gentle positioning 	<ul style="list-style-type: none"> • Subjected to air systems contaminants • Air leaks • Control speed is limited to velocity of sound • High cost of design

The pneumatic power systems were adopted for control of the vacuum chamber for NMISA DFFG-01 prototype, supporting removal of electrical conductors around the vacuum chamber.

3.2 Overview: Pneumatic systems

Pneumatics designates a branch of engineering sciences, dealing with mechanical properties of compressed gases to generate useful output. Using air as power source dates to the 1800s with applications in several industrial applications. The evolution of electrical power systems advanced and using pneumatics signified more reduction in applications on complex systems. Electricity became a power source of automation in several processes. It was challenging to use pneumatics to automate complex processes (Ilango & Soundararajan, 2007).

Development in the field of pneumatics technology gradually augmented. The development led to invention of equipment that allowed simplified automation of pneumatic systems. These systems increased the operational capabilities to comparable levels with electric powered systems. Today the choice of the power actuation systems depends solely on the application (Beater, 2007; Wojtecki, 1999).

The applications requiring extreme precision in positioning, velocity and acceleration of the actuators, are likely to use the electrical actuators. The major advantage of electric power over pneumatic power systems, is mostly precision control. Pneumatic systems attain high accuracy, though the compressibility factor of the working medium –air– makes it difficult to control the systems with extreme positioning precision (Krivts & Krejnin, 2006; Van Varseveld & Bone, 1997; Sato & Sano, 2014).

Pneumatics systems use pistons at high pressure, to convert potential energy stored in compressed air to linear and rotational mechanical motion. The precision of both linear and rotation actuator of pneumatics systems improved by using embedded sensing technology, providing these applications improved advantages to operate in complex systems. This development in the control methods contributed to the increased pneumatics preference.

Control systems techniques, such as closed loop methods, are incorporated in pneumatic systems enabling their use in complex automation. Using hard stoppers to control pneumatic systems in the past, made it difficult to have these systems performing complex operations. Current methods developed to control pneumatics systems, allow controlling the actuators to high precision, attaining multi stop stages in a pneumatic cylinder system, with a single actuator stroke. This is possible

using electro-pneumatic control valves with improved motion control characteristics (Wojtecki, 1999). Sensing technology enabled the easy of control on the pneumatic systems because of the use of electrical valves, these include solenoid, proportional and servo valves.

Pneumatics systems are mostly suitable for operations, such as robotics and manipulators. These systems require repetitive mechanism movements with high position repeatability, such as pick and place devices. These processes can be performed easily with hard stoppers open loop techniques for control. In these applications, the hard stops control system simplifies the designs in several pneumatic systems, whilst delivering high precision with high repeatability at the end positioning of actuators.

The pneumatic actuation systems include both rotation and linear motion. Piston-cylinder is used for linear motion whilst in rotation, swivel cylinder and, rack and pinion is used (Krivts & Krejnin, 2006).

Launching and positioning the vacuum chamber system involved on the NMISA prototype, requires both linear and rotary actuators respectively. Section 3.2.1 and 3.2.2 describes linear and rotary actuators respectively.

3.2.1 Linear actuators

Linear actuators are the most used types of pneumatic actuators. A standard operating linear pneumatic cylinder schematic is outlined in Figure 3-1 :

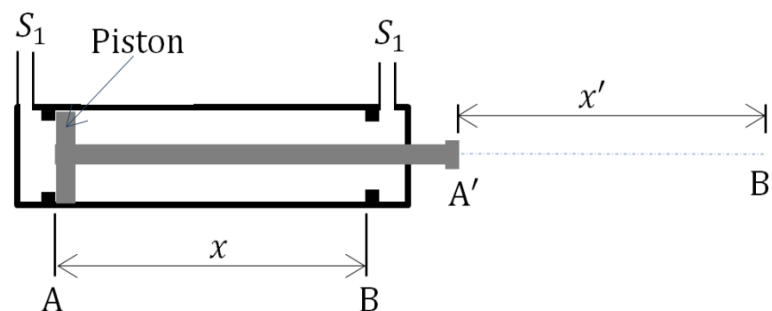


Figure 3-1: Pneumatic linear cylinder actuator

Pneumatic cylinder uses pressurised air to produce linear motion depending on the travel of the piston within the cylinder. The travel distance of the piston x results in the displacement on the output shaft x' , with $x' = x$. When air supply port one S_1 is active and S_2 is deactivated the piston moves from A to B or A' to B' stopping at B due to cylinder restrictions. When S_2 is active and S_1 is deactivated, piston moves from B' to A' . The control of the pneumatic piston can be achieved by using sensing method to gain knowledge of the location of the piston head. Also, the use

displacement encoders on the outside are used for precision control. Terminals S_1 and S_2 are connected to compressed air through electro-pneumatic valves that are electronically controlled (Prede & Scholz, 1997).

3.2.2 Rotary actuator

The rotary actuator converts the potential energy stored in the compressed air, into rotational motion. Rack and pinion rotary actuator uses a similar principle of operation as the linear actuator discussed above.

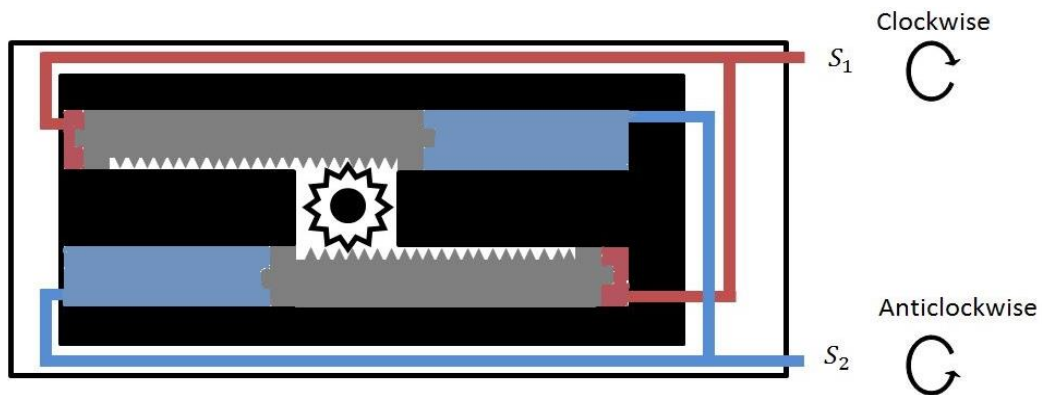


Figure 3-2: Semi-Rotary rack and pinion actuator

Swivel cylinder converts energy stored in compressed air into rotational motion. Figure 3-3 indicates the principle, when air supply port one S_1 is active and S_2 is deactivated the rotary shaft centre (O) rotates anticlockwise, and when S_2 is active and S_1 is deactivated, the shaft rotates clockwise.

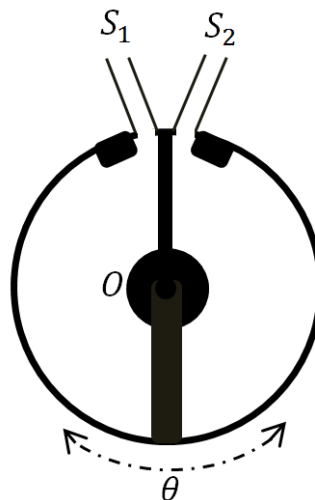


Figure 3-3: Pneumatic swivel cylinder actuator

3.3 NMISA gravimeter

This section describes the design process of the gravimeter to be tested at NMISA.

3.3.1 Conceptual design

The concept of the NMISA DFFG-01 proposed gravimeter focusses on the vacuum chamber mechanism, indicating launching, capturing and aligning of the test mass. The concept and functional overview of the concept are provided.

Rotating vacuum chamber

Vacuum chamber in free fall gravimeters is used to allow vacuum creation, it is also used for positioning the mechanisms for launching, capturing the test mass. The concept of the design uses the vacuum chamber to reposition the test mass. The vacuum chamber is rotated on its symmetrical centre of rotation, to position the test mass at high elevation in preparation for test mass drop. Pneumatic grippers are used to launch, capture and align the test mass. The rotary actuator achieves the repositioning. Figure 3-4 outlines this concept with a functional description.

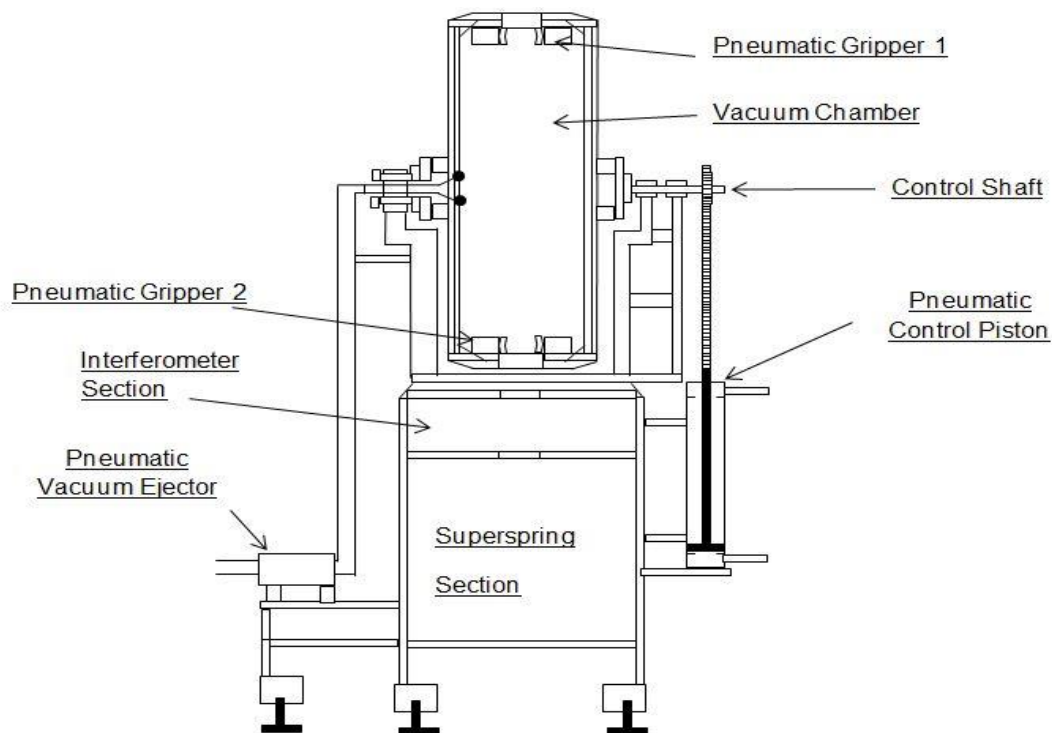


Figure 3-4: Rotating vacuum chamber concept using pneumatic actuators

The pneumatic rotary actuator achieved the prototype, comprising two significant mechanical vacuum chamber space states positions.

Functional overview

The functional process of the conceptualised gravimeter uses the interferometer and isolation system traditionally found in free fall gravimeters, whilst the vacuum chamber is designed to achieve test mass positioning with half circle rotation.

The steps of operational movements are listed in number 1 to 8. At the start of the experiments, the test mass is placed in Gripper 1 as indicated in Figure 3-4.

1. The vacuum chamber starts at a position as indicated in Figure 3-4; Gripper 2 is directly beneath Gripper 1; at the start Gripper 1 releases the test mass.
2. After the test mass has undergone free fall, Gripper 2 arrests the test mass gentle grip.
3. Gripper 2 slowly increases the grip force onto the test mass for firm grip.
4. After the firm grip of Gripper 2, rotary actuator activates to rotate the vacuum chamber 180° –clockwise– with the control shaft. The actuator is set with the hard stoppers at 180° position.
5. After a complete 180° rotation, Gripper 2 is positioned at the position of Gripper 1. Gripper 1 is at the position of Gripper 2 as indicated in Figure 3-4. This position is similar position of the vacuum chamber in Step 1, except the two grippers have interchanged positions. This manoeuvres results with Gripper 1 directly beneath Gripper 2.
6. Gripper 2 releases the test mass.
7. After the test mass undergoes free fall, Gripper 1 captures the test mass.
8. Gripper 1 slowly increases the grip force onto the test mass to firmly hold the mass.
9. The rotary actuator is activated to rotate the vacuum chamber 180° –anticlockwise–, positioning the vacuum chamber at its initial position (Step 1).

The integrated electronic communications between the pneumatic controls, interferometer and data acquisition system automation during experiments, accomplished the steps outlined.

3.3.2 Prototype design

The design of the prototype used was completed using Solidworks. Aluminium and Perspex were identified material to be used in designing the vacuum chamber due to their mass and strength ratio –lower mass and higher strength. Lighter vacuum chamber reduces the moment of inertia of the vacuum chamber, improving the rotary activators' ability to control the vacuum chamber. The construction materials were not specially prepared for vacuum applications during manufacturing and construction phases. This preparation of the material is important especially when surfaces will be exposed to very low pressure of order of magnitudes of less than 10^{-1} Pa.

The material property assignment feature in Solidworks design, enabled computation of theoretical structural properties of the vacuum chamber, failure criteria evaluation during the design phase and the actuator selection process. These included total mass, structural centre of mass and the principle moment of initial. The properties were used during the design to select the required rotary actuators to control the vacuum chamber structure. Figure 3-5 indicates the Solidworks prototype of the vacuum chamber.

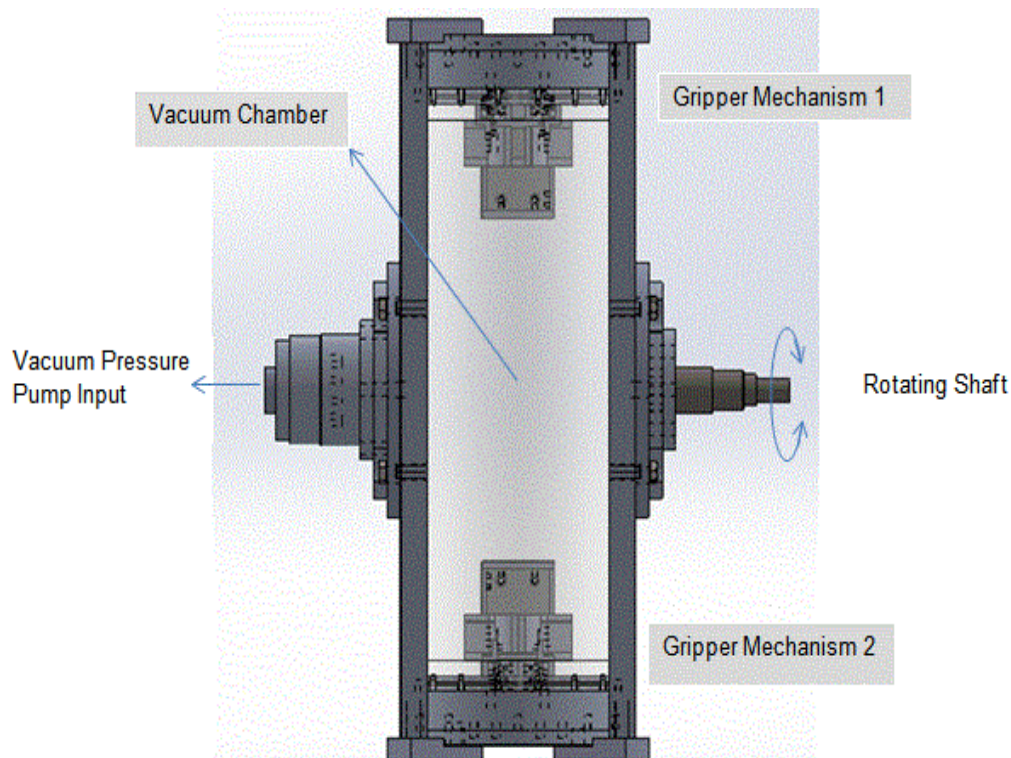


Figure 3-5: Vacuum chamber Solidworks model

FESTO supplied and manufactured the off-shelf components of the rotary actuators and parallel grippers. Double piston rotary actuator and double actuated parallel grippers are used in the design because feasible studies on their functional capabilities. The actuators' improved functional characteristics are discussed.

Rotary actuator

Double actuated rotary actuator provides improved rotation control stability, continuous stable torque and zero backlashes at the extreme end positions. Figure 3-2 indicates the concept of the double actuated rotary actuator. The air is supplied to the two supplier ports S_1 and S_2 is controlled by 5/2-way solenoid control valve.

Parallel grippers

Parallel grippers comprised two symmetrical working jaws. A single linear cylinder powered the jaws. The jaws are interconnected with mechanical links and guides, ensuring parallel symmetric jaw movement and force were equally applied on both jaws. Figure 3-6 indicates an ideal concept of connection used by parallel grippers.

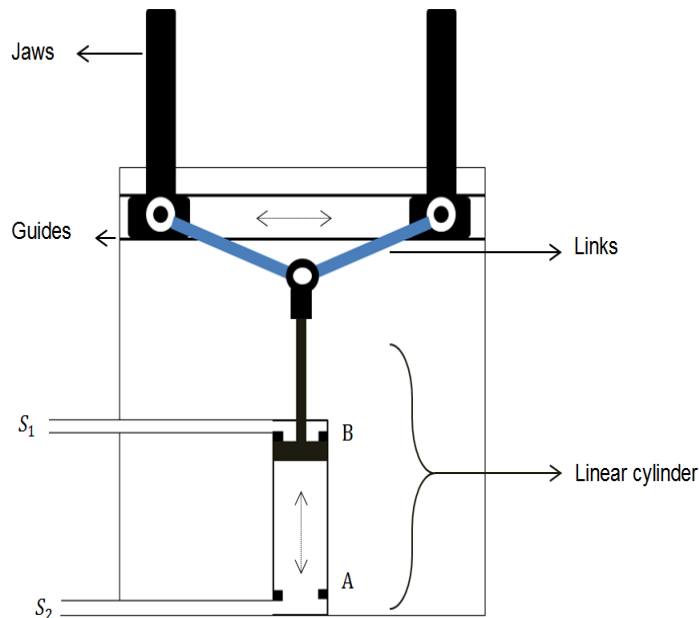


Figure 3-6: Parallel gripper mechanism

The grippers are used for test mass handling on NMISA DFFG-01 prototype. It is critical to have a zero-resultant force on the test mass from the gripper jaws during the release of the test mass. Figure 3-7 indicates the ideal test mass motion during the release. The release direction of the jaws is theoretically designed to be perpendicular to the gravitational acceleration plumb line, assuming that gravitational acceleration is directed in z direction to the centre of earth. During the test mass release, the resultant force from gripper jaws on the test mass must be zero as emphasised above, to minimise initial induced forces which can result in future translation and rotation motion of the test mass during flight. The design of the parallel gripper ensures zero resultant force –sum of forces F_R in the x direction– on the test mass during the moment of release.

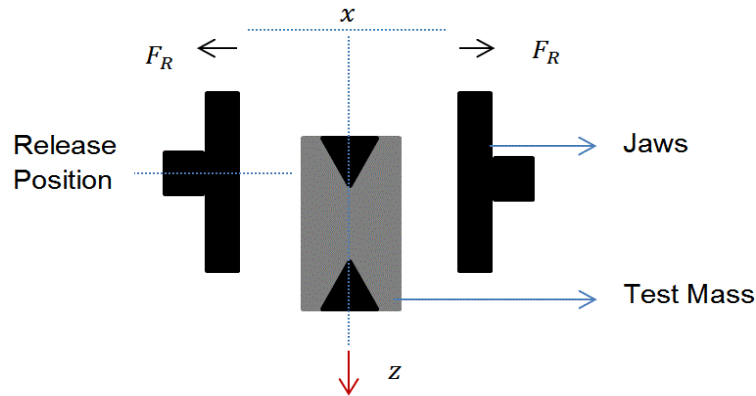


Figure 3-7: The movement of the jaws during the gripping and releasing of the test mass

The capturing of the test mass is equally important in this process, the test mass is required to be handled gently to allow subsequent drop to enable measurements. The method used in the design uses the conical concentric shaped guide. This is used to ensure that if the drop was not successful due to any possible cause, the test mass lands safely in the bottom gripper mechanism. The gripper jaws allow decreasing the velocity of the test mass till it is stopped at the correct rest position of the test mass. The jaws are slowly actuated to provide a tight grip on to the test mass, positioning the test mass in the correct alignment with the measuring beam of the interferometer. The tight grip is essential to ensure that the test mass stays in place during the rotation of the vacuum chamber when actuated to attain the position of release. The process is outlined in Appendix B.

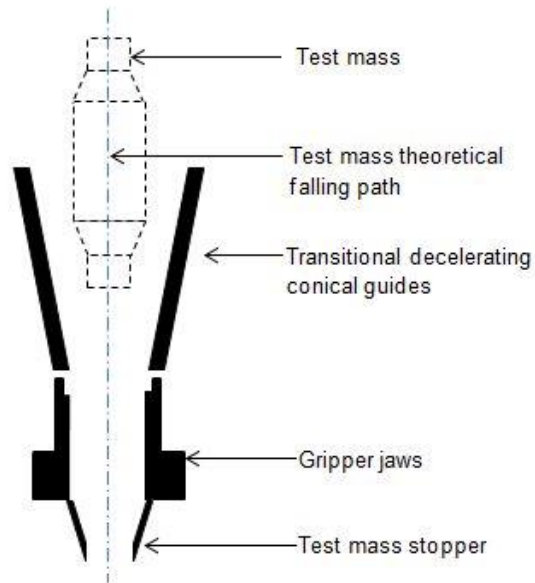


Figure 3-8: The gripper mechanism position during capturing of the test mass

Figure 3-9 indicates the vacuum chamber design with the support structure. The z direction represents the falling direction of the test mass. B_1 –Vacuum pump suction point bearing– and B_2 –Chamber rotating control shaft bearing– represent the bearing housing blocks supporting the vacuum chamber in position. The shaft and suction point of the vacuum pump are designed to be on the middle vacuum chamber to ensure that all the components rotate concentrically during the positioning of the vacuum chamber, reducing inertial actuator load.

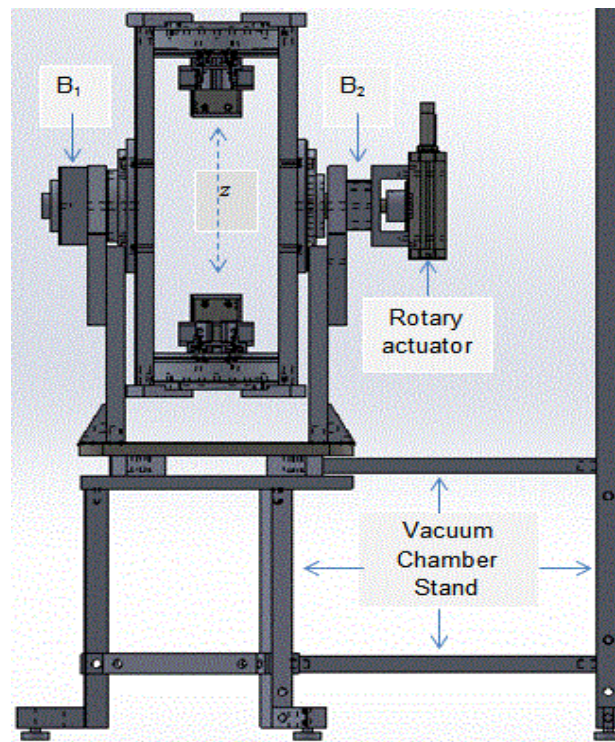


Figure 3-9: The vacuum chamber with the stand indicating all mechanical components

Appendix B indicates the full functional process of the mechanical systems of the vacuum chamber, including the launching mechanisms.

3.3.3 Manufactured prototype

The prototype was manufactured upon the completion of the prototype design. Figure 3-10 indicates the complete vacuum chamber system of NMSA DFFG 01. The figure indicates labels of various vacuum chambers as described in Figure 3-5 and Figure 3-9 above.

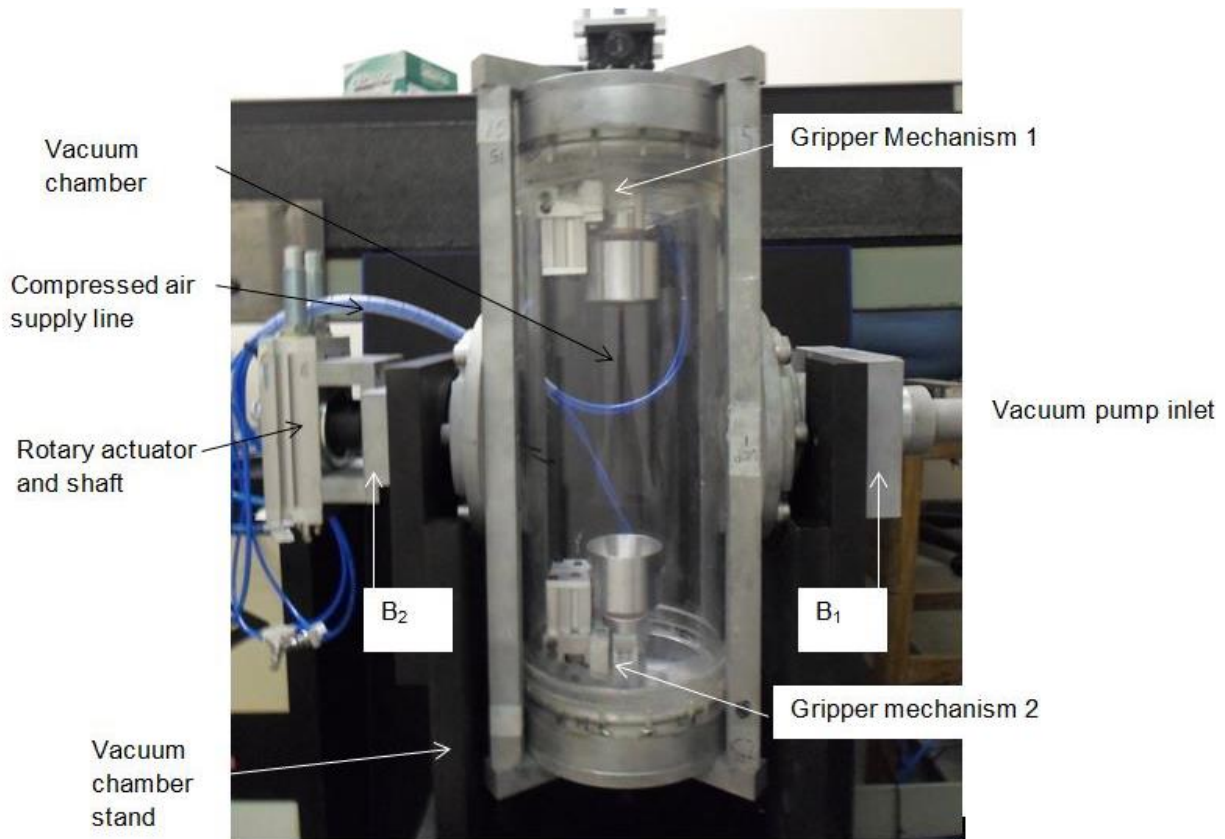


Figure 3-10: Mechanical structure of the vacuum chamber of the developed gravimeters at NMISA

3.4 Test mass

The test mass is the free-falling test object. It comprises of the retroreflector –corner cube– and housing shell. The housing mounts the retroreflector. The retroreflector is positioned within the housing in the orientation enabling the interferometry measurements during free fall. The housing also serves as a shield for the retroreflector against contact with the vacuum chamber components. The design of a double-sided test mass is used to support the functionality procedure of the invented vacuum chamber. Double-sided test mass on the designed vacuum chamber, improves the rate of measurements, compared to using a single sided test mass on the same vacuum chamber under the same procedures.

Figure 3-7 indicates that the NMISA DFFG 01 is designed to operate with the test mass, comprising two retroreflectors mounted on each side of the cylindrical test mass housing. The test mass is designed to have the centre of mass (COM) located at the concentric point and centre point of the cylinder in the dropping direction z , the midpoint distance between the two retroreflectors (Figure 3-11 and Figure 3-12).

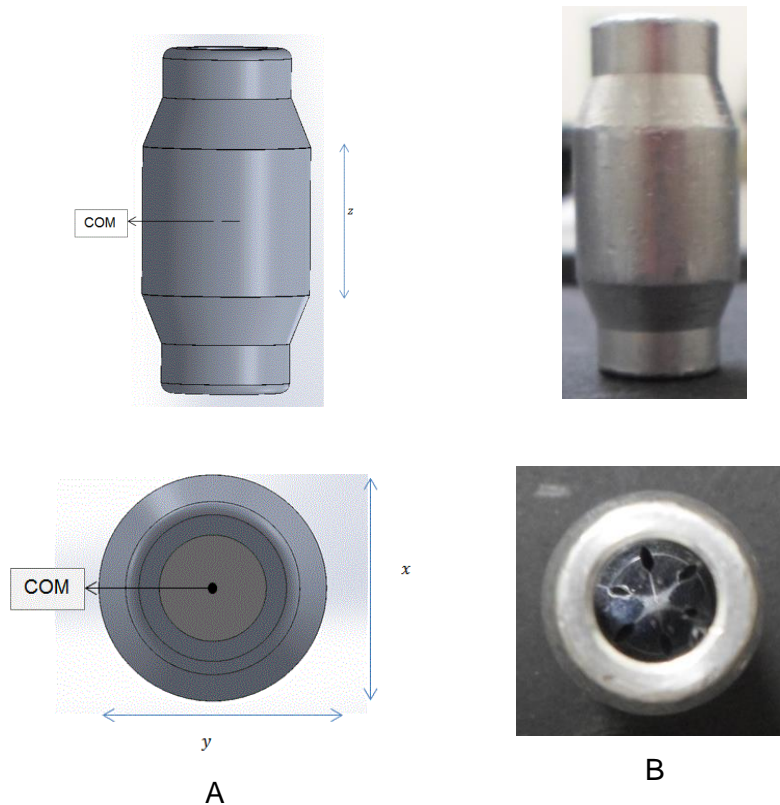


Figure 3-11: Test mass: A, designed concept and B, Manufactured

The results reported in this study are performed using test mass with two retroreflectors on both sides as highlighted above. This feature compromised one requirement for the test mass, as advised on several free-falling gravimeters. The requirement states that the COM of the test mass body must coincide with optical centre (OC) of the retroreflector to aid in reducing the errors induced by rotating test mass during free fall (Rothleitner & Francis, 2010).

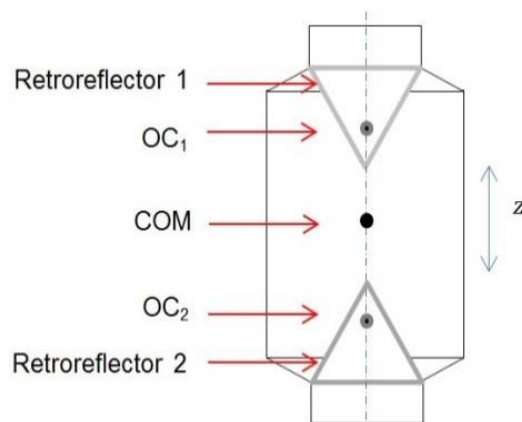


Figure 3-12: Test mass with location of optical center OC_1 and OC_2 , and COM indicated

The rotation point of free-falling object is located at the COM of the falling object. The COM and OC of test mass of the NMISA DFFG-01 does not coincide. This is compromised on both the retroreflectors. The COM and OC in the falling direction of z , are coinciding in the horizontal plane xy , see Figure 3-11. The alignment of COM and OC in the falling direction of the test mass rotation as indicated in Figure 3-12 is therefore minimised in the current test mass (Rothleitner et al., 2007).

The free-falling equations of motion were evaluated to select the supporting electronics components required for data acquisition measurements and to determine electronic parameters.

3.5 System parameters and constraints

The prototype manufactured has a total projectile length of 0.3 meters, measured from the launching gripper to the capturing gripper in the z direction. Test mass dynamic parameters guide the capability of the electronics required to acquire intensity signal expected from the drop length. These include falling distance in the vacuum chamber, time of flight, velocity of the test mass and laser wavelength.

3.5.1 Dynamic parameters

The ideal equations of motion determined the time taken by the test mass in flight and the velocity that the test mass attains during flight. The test mass is released from rest position to fall freely due to gravitational force. The g value of 9.81 m/s^2 is used in determining these parameters. The equations used in determining the dynamic constraints are:

$$V_i^2 = V_o^2 + 2gt \tag{3-1}$$

$$h = V_o t + \frac{1}{2} g t^2 \tag{3-2}$$

where h is the height covered by projectile during the drop, the value of $h = 0.3 \text{ m}$ for the designed vacuum chamber, t is the time taken by projectile in flight from position 0 –launching gripper– to i – capturing gripper–, V_o and V_i are the initial and final velocity respectively. The initial velocity at the release position is zero because the test mass is launched from rest. The final velocity just before the test mass touches the capturing gripper mechanism is calculated.

Using the equations above parameters indicates the time it takes the test mass to cover the height of 0.3 m in free fall is 0.2473 s calculated using (3-1). The final velocity of the test mass at the capturing gripper mechanism is calculated by (3-2) to be 2.2027 m/s . The calculated time and

velocity combined with the displacement covered, will guide the selection of the electronic modules required for the acquisition of the intensity signal produced by the interferometer.

3.5.2 Electronics capabilities

The interferometer discussed in Section 2.5, describes the theory of the interference and outlines the optical components used in amplitude division interference phenomenon. The first component indicated on the interferometer is the laser source, providing light used by the interferometer. The SI standard unit of length and the He-Ne Laser red with wavelength of 633 nm, is used to link the test mass displacement to the global length standard.

The detector is the first component of the required electronics components to acquire the displacement data of the free-falling mass by mapping the intensity signal. Using Equation (2-18) in Section 2.5.2.3 of the phase change ($\Delta\phi$) to reconstruct the waveform of the fringe signal produced during interference, the oscillating electrical signal has an instantaneous decreasing wave period T_f over the flight. Period T_f corresponds to the constant phase change of $\Delta\phi = 2\pi$, whilst phase change 2π corresponds to displacement of the test mass $\lambda_f = 0.5\lambda$, which is 316.5 nm (Figure 3-13).

Light intensity distribution maps the falling distance of test mass, using He-Ne Laser. By interference, the falling displacement can be mapped using nanometre displacement, changing over time. The required number of wavelength N to reconstruct the required 0.3 m falling distance is:

$$N = \frac{h}{\lambda_f} = \frac{0.3\text{m}}{316.5 \text{ nm}} = 947869.2986$$

The interference fringes are mapped as a voltage signal. The voltage signal holds maximum voltage (V_{\max}) and minimum voltage (V_{\min}), corresponding to bright band and dark band respectively as emphasised in Section 2.5, representing the constructive and destructive interference.

The signal is analysed using a method requiring the determination of zero-line crossing time points. A zero-line indicates the point of transition from dark to bright or from bright to dark fringe band on a bright and dark fringes diagram, using the intensity graph. This line represents average voltage value between (V_{\max}) and (V_{\min}). Figure 3-13, used only to demonstrate the phenomenon used in zero-crossing and how the displacement is reconstructed from the fringe signal.

In Section 2.5.3 the zero-crossing method is described; this section details the method used to reconstruct the displacement coordinates using zero-crossings. The free-falling objects are assumed to have a constant acceleration when gravity gradient is negligible. The test mass velocity increases linearly with time during the projectile period. The highest velocity reached is used to set the minimum requirements of the electronics components, ensuring all system parameters selections are determined with safety operation factor.

The final velocity V_i computed above of 2.2027 m/s is used in all the future calculations. This is calculated as highest test mass velocity during the experiments. The frequency of the signal increases with time, resembling velocity of the test mass. This gives rise to a chirp signal with constant amplitude and variable frequency. The time interval between the consecutive zero-crossing interval decreases continuously from the launch of the mass, implying that the period of the signal reduces continuously.

If the current zero-crossing is set to be initial height h_0 of the test mass, at detection time t_0 , and the next zero-crossing will be detected at time t_1 , then the test mass dropped displacement of $\lambda/4$ over elapsed time interval $\Delta t = t_1 - t_0$. The procedure is used to process the entire voltage-time signal whilst reconstructing displacement-time signal.

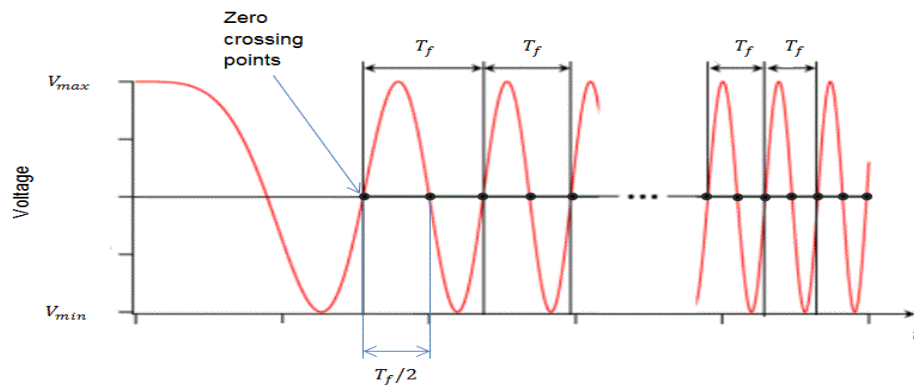


Figure 3-13: Photo-detector output signal (Baumann et al., 2015)

When the change in displacement of the test mass is $\lambda/4$, the phase change difference corresponds with π . The fringe signal crosses zero-line of the intensity distribution, that oscillates between maximum and minimum voltage is twice the number of wavelength N . Number of zero-crossing N_{zc} is provided by:

$$N_{zc} = 2N \approx 1\,895\,738$$

The number of zero-crossings from the fringe signal corresponds to samples of interest from interference distribution graph to reconstruct total displacement history.

The rate of occurrence of the zero-crossing points must be determined to select the sampling rate of the electronic signal acquisition card. The final velocity of the test mass is used to calculate highest frequency of the zero-crossing of the intensity signal. The distance between two zero-crossing points $0.5\lambda_f$ covered by the test mass falling at velocity V_i calculates the frequency of occurrence of the zero-crossing f_{zc} points at the end of the falling height.

$$f_{zc} = \frac{V_i}{0.5\lambda_f} = \frac{2.203\text{ms}^{-1}}{0.25 \times 633 \times 10^{-9} \text{ m}} = 13.92 \text{ MHz} \approx 14 \text{ MHz}$$

The frequency of the intensity signal at capturing gripper is approximately 7 MHz. The electronic devices required to capture the signal must map the intensity signal accurately, enabling accurate detection of the samples of zero-crossing time coordinates during signal processing. The electronic system requirements are detailed, describing the electronics module required.

3.6 Intensity signal processing method

The signal produced by the detector in mapping the resulting intensity signal, is digitised and stored for post-processing. The stored data comprise two arrays of data, time and voltage coordinates. In achieving accurate mapping of the intensity signal, higher sampling frequency and a higher bit resolution card can improve detecting the true crossing time. Improved time detection is a requirement for accurately reconstructing the displacement of the projectile.

Figure 3-13 indicates the output intensity signal from the detector, using the principles of interference discussed in Section 2.5 that every instant the signal crosses zero-line the test mass has travelled a distance of $\lambda/4$. Using voltage-time coordinates, the displacement-time coordinates are generated and these coordinates are used for realising g value. This array is generated by adding the $\lambda/4$ to the reference position. The first detected time point T_1 is taken as reference time and the displacement of the test mass is set to zero. When the signal crosses zero at T_2 , the test mass was displaced by $\lambda/4$. This analyses results with time-displacement data array (Rothleitner et al., 2009).

Time (T_n)	Displacement
T_1	0
T_2	$\lambda/4$
T_3	$\lambda/2$
\vdots	\vdots

3.7 Systems requirements

The signal is processed to extract the zero-crossing points of the signal. ADC digitiser is used to digitise, acquire and store the fringe signal to the computer. The signals stored are later processed to extract time-displacement coordinates.

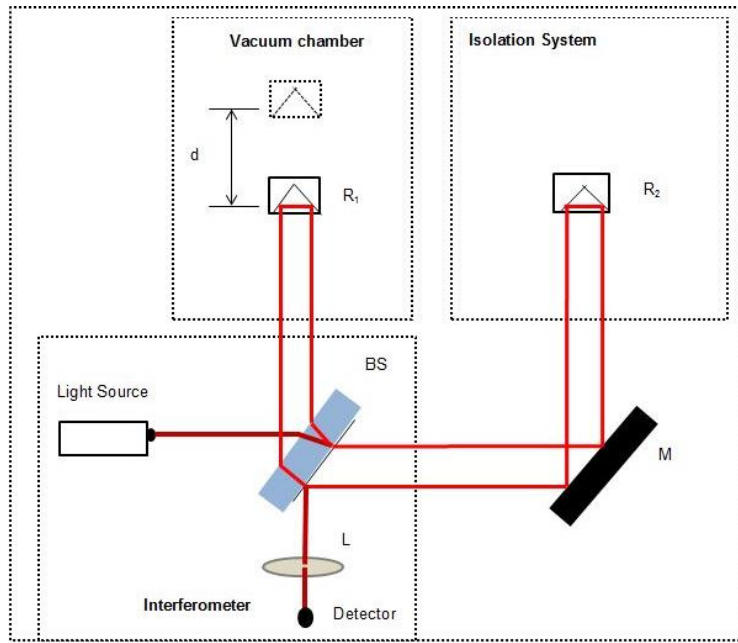
When processing the signals with constant period, Nyquist theorem must be met for minimum sampling frequency, stating that the sampling frequency must be at least twice the highest frequency of the systems (Orfanidis, 2010). In the free fall gravimeters, the signal acquired has a continuously variable decreasing period. The sampling rate required for gravimeters applications is proposed to be seven times more than the maximum zero-crossing frequency (f_{zc}) that the system attains during a single drop. Using high sampling frequency is essential, enabling improved correct detection of the true behaviour of the observed signal, also preventing aliasing in the sampled data (Rothleitner, 2008). The electronic data acquisition components are to be sampled at minimum sampling frequency f_s .

$$f_s = 7f_{zc} = 98 \text{ MHz}$$

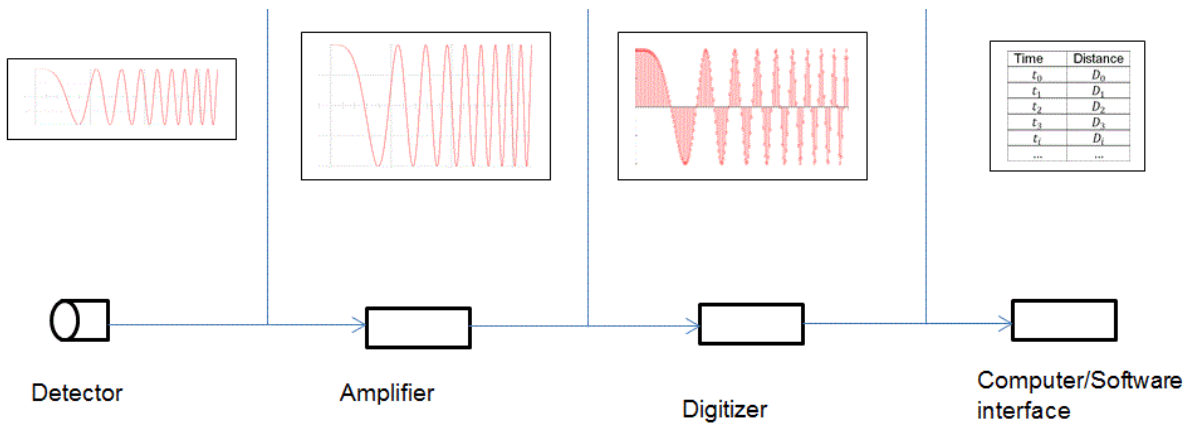
Using electronic digitiser in free fall gravimeters is ideal because digitisers are emended with real time accurate clocks. Digitisers can be coupled to more accurate external clocks to improve their timing capabilities. Further advantages of digital data in gravimeter, is that one signal can be processed using various algorithms. Various methods of analysing can be compared. Using digitisers enables detecting zero-crossing without additional electronics components on the system, minimising systematic errors.

The sampling time t_s of 10ns is proposed as it would reduce time detection with error resulting from linear interpolation. A 100 MHz digitising card with eight bits resolution is selected for data acquisition for the NMISA DFFG-01 in the development phase.

Figure 3-14 indicated the gravimetry components, diagrammed in an integrated system. The detector maps the analogue intensity signal in the form of electrical (voltage) signal. The signal is digitised and stored. The digital voltage-time data is loaded to the software for post-processing, enabling time-displacement extraction.



A



B

Figure 3-14: System setup and electronics: A Hardware and B Electronics and Software

3.8 NMISA DFFG-01 system components

The NMISA DFFG-01 complete gravimeter system integrated mechanical, pneumatic, electrical, and electronics components.

3.8.1 Mechanical and pneumatics components

The mechanical components include, the pneumatic gripper [DHPS-16-A] used for launching, capturing and aligning the test mass. The semi-rotary actuator [DRRD-25-180-FH-Y9A] used in repositioning the test mass.

3.8.2 Pneumatic and electrical interface components

The electrical interface components include the solenoid valves [CPE10-M1BH-5J-M7] coupled with electrical head socket [KMYZ-9-24-SLED-PUR-B] for air control, using electrical signal from the programmable logic controller (PLC). The PLC [FEC-FC30-FST] programmed with FST – FESTO software– was used, controlling the mechanical components.

3.8.3 Electronics components

Polytec OPF 505 sensor head is the interferometer sub-system used for displacement measurement of the free-falling object. The signal is filtered and amplified by vibrometer controller OFV 5000. Data acquisition is performed by NI-USB-5133 digitiser module.

LabView software was used to control the ADC card. The external mechanical trigger was used to initiate the acquisition during manual experimental tests. PLC was used as the trigger signal during measurements. The signal displaying oscilloscope by Agilent technology, was used in observing the quality of the interference signal during system alignment. The acquired signals were stored and processed using Acer, AMD A8-4500M APU, Radeon 1.9 GHz, 8 GB RAM.

3.8.4 Vacuum pump station

The vacuum chamber was connected to a vacuum pump PFEIFFER D-35614 Asslar with a capacity of 10^{-5} Pa maximum attainable vacuum pressure. The sensor head Leybold, Vacuum GmbH D-50968kln, was mounted on the vacuum chamber outlet to monitor the pressure level of the vacuum chamber during experiments.

3.9 Complete prototype system setup overview

The sub-systems of the prototype are indicated in figures of this section, integrating the sub-systems.

3.9.1 System hardware setup

The vacuum chamber of the NMISA DFFG-01 was connected to the stand frame, using bearings on both sides of the vacuum chamber, ensuring proper alignment during rotation as shown in Figure 3-15.

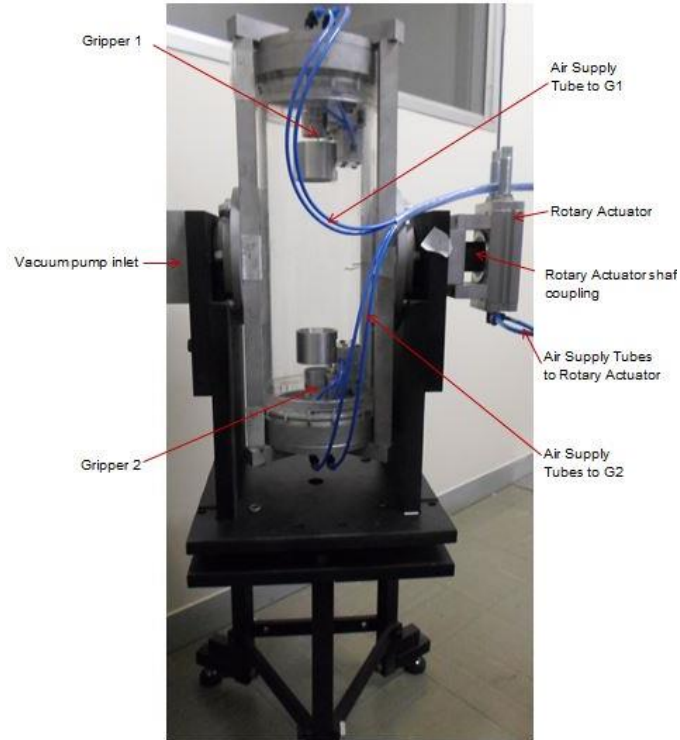


Figure 3-15: Vacuum chamber and structural stand

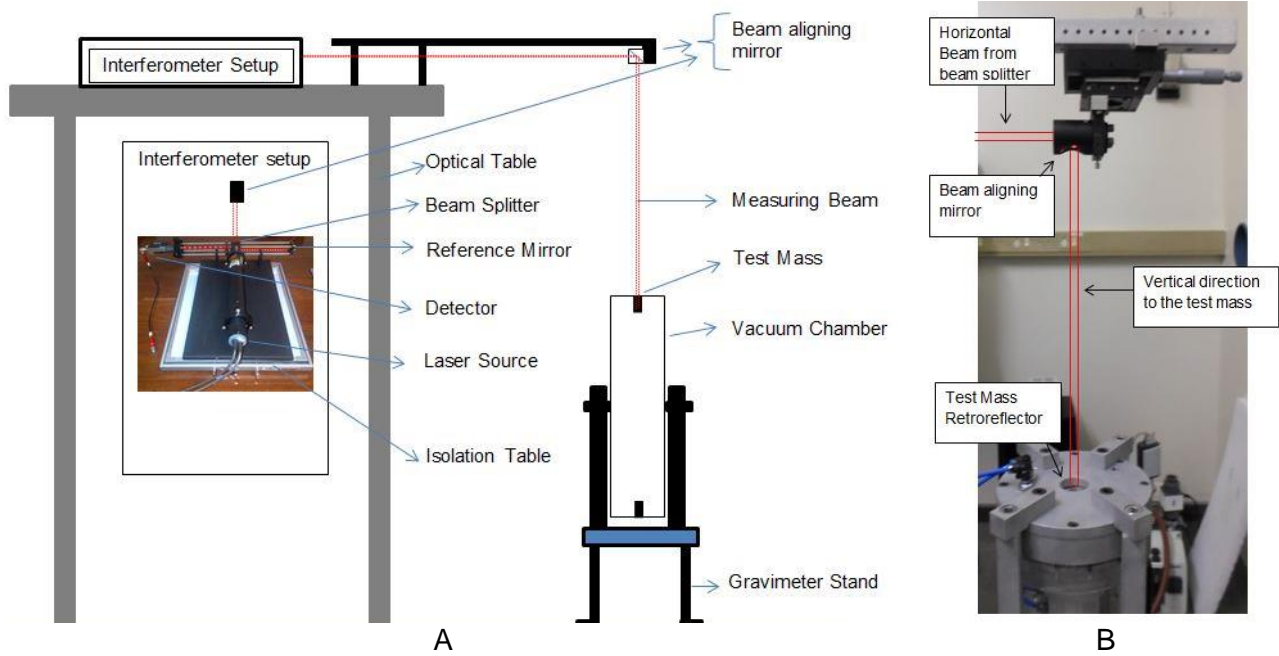
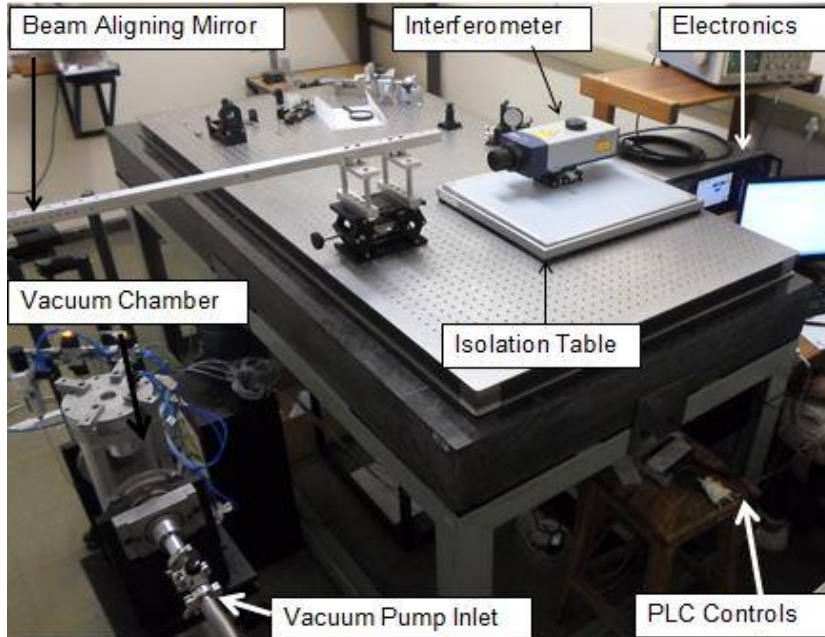
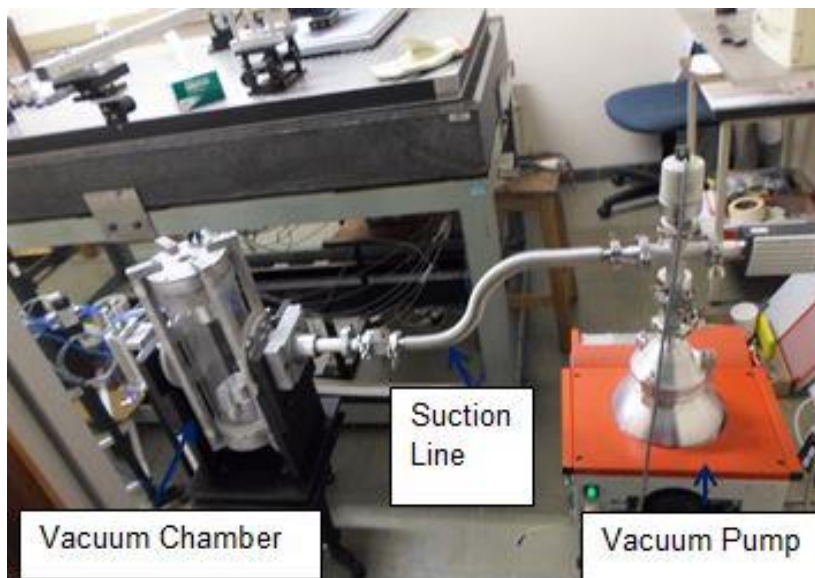


Figure 3-16: Optical table with Interferometer setup, extended to the vacuum chamber: A-The complete setup overview, B-Vertical laser beam alignment

The interferometer used in the continuous system development was set up on the optical table. The process aided in practical skills development on laser systems. The diagram in Figure 3-16 indicates the setup used. The variable leg beam is directed from the table to suit the positioning of the gravimeter vacuum chamber on the laboratory floor. The extending arm is fitted with the adjustable mirror to enhance beam alignment in the vertical gravity plumb line direction.



[A]



[B]

Figure 3-17: NMISA DFFG-01 prototype setup [Partial sub-systems arrangements in A and B]

The final system setup used the interferometer, manufactured by Polytec laser system; optical arrangements were embedded in the laser head. The laser head was rested on top of the passive air isolating table (Figure 3-17 A and B).

The laser interferometer system was supported by the controller used to set and control measurements parameters of the laser.

3.9.2 Sub-systems interface diagram

The NMISA DFFG-01 system included sub-system integration, allowing the functionality of the whole gravimeter system. The sub-system diagram represented the actual layout interface of the prototype (Figure 3-18).

The PLC was used to control the mechanical movements of the vacuum chamber. The special external trigger was designed and integrated onto the PLC to control the digitiser by coupling the electronic to mechanical function. The trigger was operated both manually and automatically to couple and decouple the digitiser to start acquisition when the test mass was released. Signal size was used to control the end of data acquisition. The trigger was coupled to the gripper in a state to release the test mass. When the PLC signalled the test mass release, the same PLC signal was instantaneously used to initiate the acquisition. The digitiser trigger delay period was set to compensate the true time of the gripper mechanism actuation.

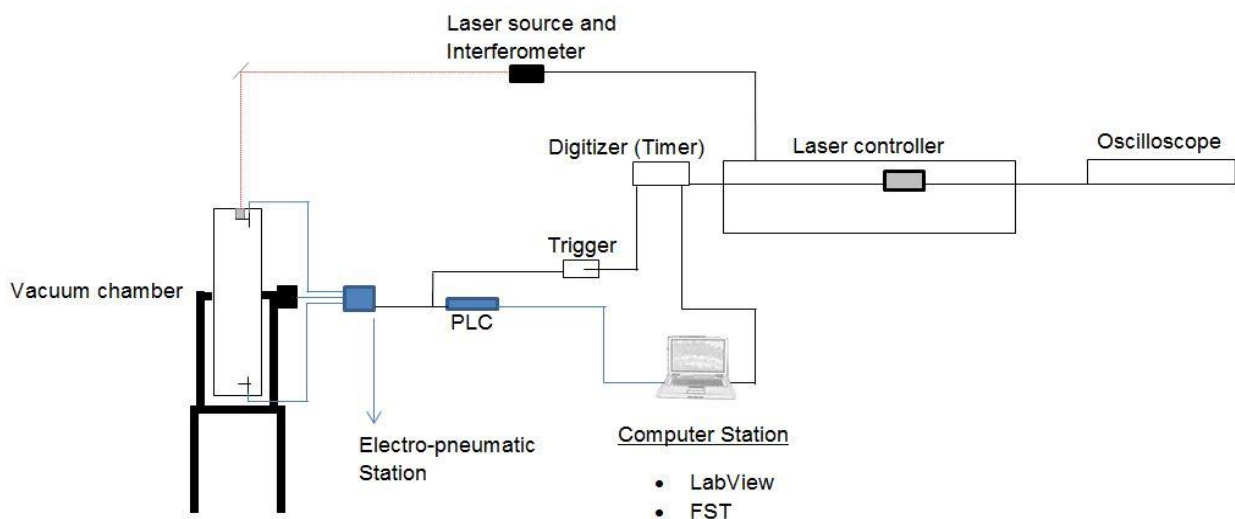


Figure 3-18: NMISA DFFG-01 full sub-system integration network for measurement process control

CHAPTER 4

Simulations

The NMISA DFFG-01 prototype experimental drops results were projected for processing using software codes used in analysing the numerically produced intensity signal. The simulated signals were generated and processed using the zero-crossing method previously explained.

4.1 Simulation setup

LabView was used to generate the intensity signal graph, simulating a free fall photo-detector output, using a two-leg interferometer. Random noise was added to the simulated signal to increase the practicality of the generated signal under effect of gravitational acceleration. The value of 9.786098 m/s^2 , the value used by the mass laboratory at the NMISA site, measured in 2012 by the Council of Geoscience Pretoria, was used in free fall equations (3-1) and (3-2) above for generating parameters. Table 4-1 indicates the numerical parameter values, computed in CHAPTER 3. Gravitational acceleration is assumed to be constant for the falling distance of the prototype. As a result of this assumption, the effect of gravitational gradient is neglected and velocity of the test mass increased linearly during the projectile with proportionality to time spent in flight and displacement travelled.

Table 4-1: Intensity signal major properties

Parameters	Magnitude
$t_i(T)$	0.2473 (s)
f_o	0 Hz (Stationary test mass)
f_i	6.96 MHz

The assumption of a constant gravitational acceleration helped in simplifying the algorithms used to generate the intensity signal numerically. The intensity signal produced during free fall experiments is a frequency modulated signal. As the test object free falls, velocity increases, resulting with a relative frequency increase of the intensity signal.

Voltage $V(t)$ signal resulting from a constant acceleration system with constant velocity can be represented by sinusoidal interference intensity graph as:

$$V(t) = A \cos(\omega_o t + \phi) \tag{4-1}$$

where ϕ is the initial constant phase shift of the signal and A is the amplitude of the electrical signal produced. The signal has an instantaneous phase $\theta(t) = (\omega_o t)$ that varies linearly with time. This signal has a constant radian frequency $\omega(t)$ of:

$$\omega(t) = \frac{d}{dt} \theta(t) = \omega_o \left[\frac{rad}{s} \right]$$

Instantaneous frequency of the signal is provided by $f_i(t)$ as:

$$f_i(t) = \frac{1}{2\pi} \frac{d}{dt} \theta(t) = \frac{\omega_o}{2\pi} \text{ [Hz]} \quad (4-2)$$

The falling test mass generates an intensity signal with a variable frequency from initial frequency f_0 of zero where the test mass is released from rest to final frequency f_i where the test mass is captured. The instantaneous frequency of a non-zero constant acceleration signal is provided by:

$$f_i(t) = \beta t + f_0 \quad (4-3)$$

where β represents the instantaneous frequency slope, provided as:

$$\beta = \left(\frac{f_i - f_0}{t_i - t_0} \right)$$

Let $T = t_i - t_0$ and represents total sweep time of the projectile. Using Equation (4-2) and (4-3), the instantaneous phase of the sinusoidal of intensity signal becomes:

$$\begin{aligned} \frac{d}{dt} \theta(t) &= 2\pi(\beta t + f_0) \\ \theta(t) &= 2\pi \int \left[\left(\frac{f_i - f_0}{T} \right) t + f_0 \right] dt \\ \theta(t) &= 2\pi \left[\frac{1}{2} \left(\frac{f_i - f_0}{T} \right) t^2 + f_0 t \right] + C \end{aligned} \quad (4-4)$$

The voltage signal produces from light intensity distribution in the free fall gravity experiments is mathematically represented by:

$$V(t) = A \cos \left\{ 2\pi \left[\frac{1}{2} \left(\frac{f_i - f_0}{T} \right) t^2 + f_0 t \right] + \phi \right\} \quad (4-5)$$

LabView VI codes and scripts are used to generate data of the intensity signal with the parameters in Table 4-1. Equation (4-5) resulted with approximately 25 Million samples of time and voltage data pairs from the test using sample time step of 0.00000001s –100 MS/s digitiser. The programs are

coded to produce results identical to the results of the ADC card specified in CHAPTER 3 over the period of time of the projectile of t_i .

Digital triggers are set to specify the section of data to be analysed. Time vector is used as the trigger in the numerical simulations. The triggers are necessary to allow the analyses of the required segments of the signal. Signal from the time that the test mass is released, to the time the test mass is captured, can be recorded but the digitising module is controlled to specifically trigger the acquisition of the signal at a provided signal frequency, corresponding to time point. Data size was used to set the end of the acquisition.

Ideal and noisy voltage signals were generated. The ideal signals were processed and the agreement in the gravitational acceleration value displayed a perfect correlation to the exact predefined gravitational value. The noisy signals were processed and their results showed that the processing algorithms processed the signal as intended.

The equations of motions were used to generate the ideal displacement, velocity and frequency graphs. The ideal gravitational acceleration would be constant of 9.786098 m/s^2 . Figure 4-1 indicates the ideal displacement-time graph of the free-falling test mass extracted from simulation. This figure indicates the projectile displacement history from release position to the capturing point. Red vertical graphs A and B represent the position where data acquisition initiates and stops respectively, for signal processing.

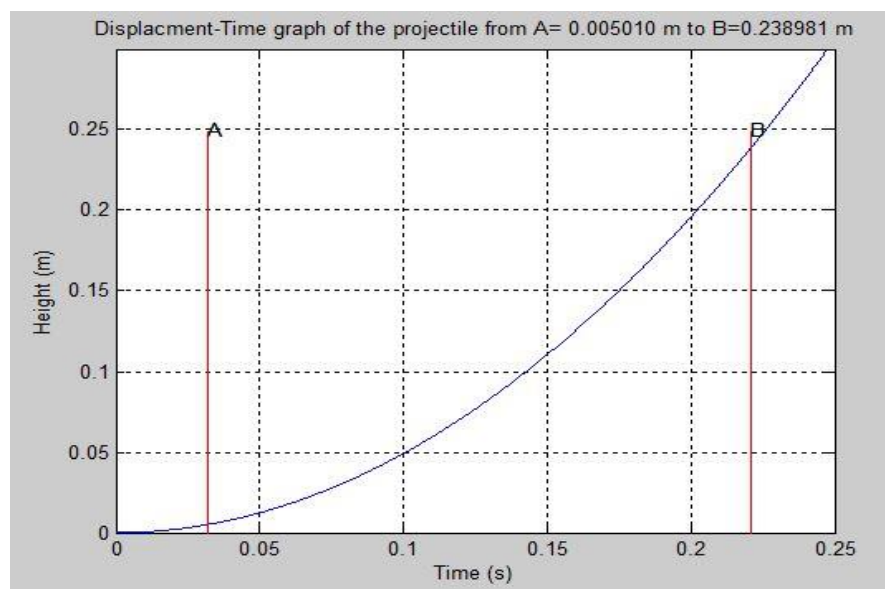


Figure 4-1: Displacement of the test mass over the projectile period

Figure 4-2 and Figure 4-3 indicates the velocity and frequency profile of the test mass. The relationship between the velocity of the test mass and signal frequency of the intensity signal as a function of time during the projectile period, is linear as the gravitation acceleration is assumed constant.

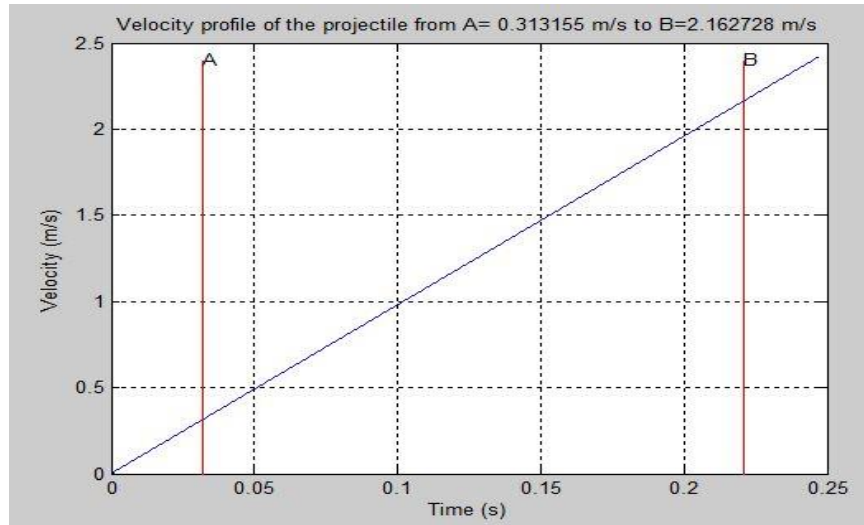


Figure 4-2: Velocity of the test mass over the projectile period

Figure 4-3 indicates the signal frequency profile from the test mass launch up to the end of flight of the test mass. The frequency increased linearly over projectile time from 0 to 6.96 MHz at the end of the test mass flight.

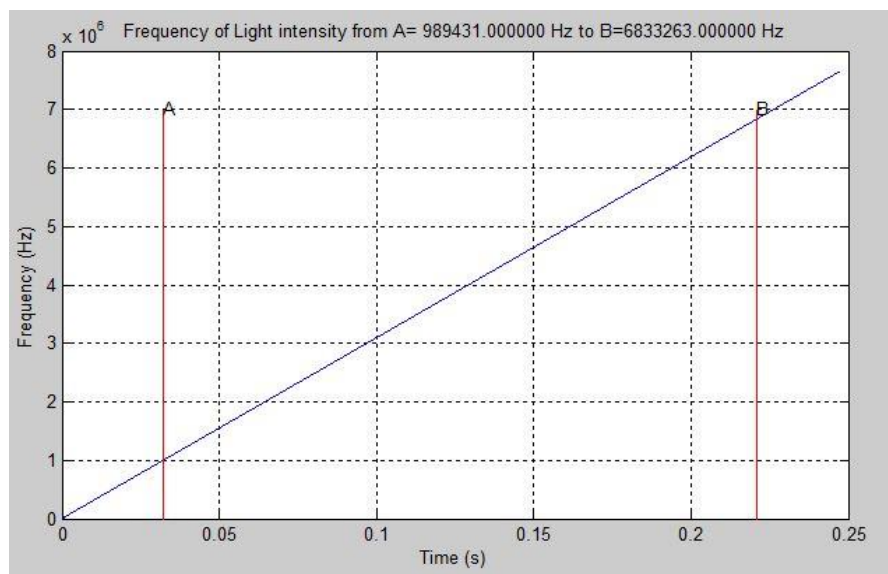


Figure 4-3: Frequency of the light intensity signal over the projectile period

4.2 Simulation results

Gravitational simulation was performed with pure intensity generated graph. This signal serves as the signal for true gravitational acceleration value for comparing all the simulated results. Parameter values in Table 4-1 are applied to the voltage chirp signal with constant amplitude and variable frequency.

4.2.1 Ideal gravitational acceleration calculation

The signal is processed using the zero-crossing method discussed in Section 3.6. Gravitational acceleration computations were performed using the equation introduced in Section 2.3 for direct free fall measurements.

The ideal gravitational acceleration of NMISA's site is 9.786098 m/s^2 . Computing gravitational value from pure generated signal, ideal gravitational acceleration computed using ideal intensity signal output is:

$$9.786098 \text{ m/s}^2$$

The error of between the calculated gravitational value and the site measured gravitational acceleration were within few parts 10^8 . The practical computational values of the simulations were performed and compared with the true value on the current certificate of measured gravitational acceleration at the NMISA site. The agreement of the two values validates the model of the simulations algorithms codes.

The experimental measurements signals of the prototype were projected with noise magnitude because of acquisition systematics errors. Noise induced signals were simulated and processed to compare these results with the pure signals results. Repeated simulations were performed with various noise levels, evaluating the processing method used for filtering noisy signals.

The zero-phase shift filter was applied in filtering the signal to avoid the time distortion of the signal. Preserving the phase of the signal ensure that time coordinates were not altered during filtering. It is a requirement in applying gravitational measurements to have time detected with errors of less than $\pm 0.1 \text{ ns}$, whilst requiring length realisation error of less than of $\pm 0.5 \text{ nm}$ (Torge, 1989). The interpolation introduced a computational error on the system through processing. The error introduced by interpolation was reduced when the digitising card was set to sample at higher frequency.

CHAPTER 5

Prototype evaluations and results

NMISA gravimeter prototype was finally tested with experimental free fall drops to evaluate the mechanical functionality of the prototype and system functionality. The evaluation procedure is outlined in this chapter.

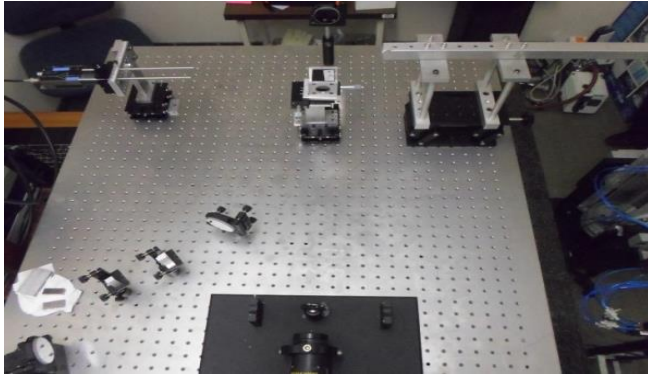
5.1 Experimental procedure

The mechanical system designed was ready for the measurements. The vacuum chamber was tested to be operational and controllable according to the initial design of operation upon the completion of fabrication.

The Integration of the interferometer system on to the mechanical sub-system was initiated. Two setups were used for optical interferometry during the project development. Both interferometers were initially experimented with free fall drops in the atmospheric pressure, checking their functionality prior to final system evaluation.

The project objective was aimed at having the experimental tests performed in an evacuated space after all system tests were completed. This included the mechanical functionalities, mechanical controls, launching and capturing mechanisms, repositioning systems and interferometer incorporation on the system.

Figure 5-1 indicates the first interferometry optical setup used during the development phase and the typical interference signal produced by this interferometer setup. The output interference could not be directed and detected, due to the lack of optical equipment. However despite the difficulties, it was observed that the test mass dropped in the path of the laser beam, aligned with the gravity plumb line.



A

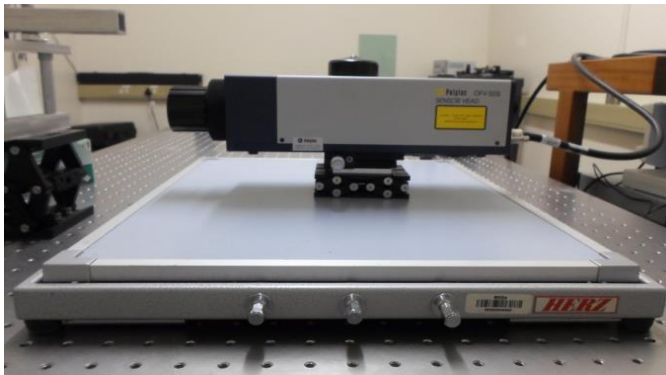


B

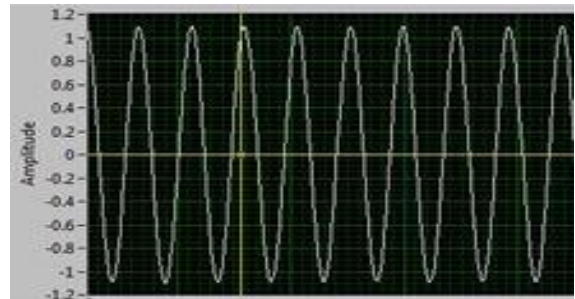
Figure 5-1: A: Interferometer optical setup and B: Produced intensity signal from the initial system setup

The digital processing algorithms were applied to implement filtering of the signals, using median and zero-phase shift filters with numerous filtering parameters. The signals were smoothed and processed. Resulting gravitational accelerations were concluded to be void. They were out of range of practical gravitational acceleration value on earth. The signals produced by this interferometer were not used for further analyses; the interferometer was changed.

The second interferometer used, was the Polytec integrated interferometer system, including the OFV 505 sensor head and OFV 5000 vibrometer controller. The sensor head has a built in optical interferometer setup with the reference mirror and laser source built on the sensor head unit. Figure 5-2 indicates the interferometer optical sensor head and a typical light intensity voltage signal produced by this system.



A



B

Figure 5-2: Second interferometer setup used on the NMISA DFFG-01, A: Polytec optical sensor head setup B: Produced intensity signal

The sensor head was mounted on an isolating table, improving the stability of the reference mirror after observing an average of 50 Hz random vibrations frequencies, resulting from system instabilities during system tests. The DT-4048-A isolation table manufactured by Hertz was used.

External vibrations on the system were evaluated by performing measurements with the isolated and non-isolated interferometer sensor head.

Furthermore, human induced vibrations were evaluated using isolated interferometer head at different times of the day by comparison of measurements taken during the day and night. During the day, ground vibrations were assumed to be high at NMISA as it is situated 600 meters from the N1 and N4 national roads. The volume of the cars passing by at night is decreased. It was decided to perform the measurements at night time, with the system on the isolation table.

Resulting from these system evaluations, it was observed that the prototype produced high magnitudes of vibrations during its operation. Vibrations were induced by the mechanical grippers during launching. Measurements with the system mounted on the isolation table, were performed only during the day.

Experiments were accomplished using the mechanical manoeuvring procedure outlined in Appendix B. The procedure of analysing the results from the measurements was based on statistical analyses of free-falling drops. Free-falling drops were continuously taken by performing multiple drops to form sets. A set comprising multiple of drops, ranged from 8 to 10 launches.

All the drops were stored as voltage-time signals. The stored signals were post processed later by loading each signal to software algorithms codes, to compute gravitational acceleration for each drop in the set. Statistical methods of data analyses were applied onto each set of free fall drops to evaluate the mean gravitational acceleration and the sets' standard deviation, associated with each set.

Free fall signals were acquired and stored using NI-USB 5133 digitising card onto the storage drive for post-processing. A set comprised of signals produced by both Gripper 1 and 2. The evaluation on the two grippers was performed to check if the two grippers produced different signals, resulting in their independency of launching the test mass. The signals indicated only a different time delay from the grippers at the instance of the test mass release, concerning the digitising module trigger time measurements. The delay was due to random friction factors on the mechanical components in the control valve and actuation cylinders however intensity signals were comparable. Gripper 1 and 2 indicated different test mass release time points; this difficulty could not be solved practically. As a result, a digital trigger was implemented to account for the delay. The digital trigger was added to the signal processing algorithms.

A digital trigger was designed to crop the original acquired drop signal produced by Gripper 1 and 2 at a single instantaneous signal frequency. The zero crossing frequency of 5 MHz is used,

corresponding to 0.005 m displacement covered by test mass in free fall motion. This triggering method ensured that the signal produced from the falling test mass released by Gripper 1 or 2 are processed from similar initial velocity conditions, resulting with analyses of the drops performed over the same displacement range. At the completion of evaluating this system integrated with the data acquisition method, the vacuum equipment was integrated to the system and measurements commenced.

The measurements performed on the NMISA DFFG-01 were analysed using statistical methods to realise the gravitational acceleration, by calculating the mean set value. This method evaluated the effects of contributing systematic parameters. The prototype was tested at different operating conditions by changing controllable system operating parameters. At each varied operating parameter, mean gravitational acceleration and standard deviation of the set, were computed for comparison.

Vacuum chamber operating pressure is a major factor affecting the measurement in free-falling gravimeters. As a result, this factor was evaluated during the development. The other conditions and parameters, such as vibrations and laser properties were not quantified during the evaluations because of the lack of skills, knowledge and equipment. The results of measurements taken in the development process of the prototype are summarised in Appendix D. The results discussed in this chapter are the final results measured using the best system setup of the prototype.

Vacuum chamber operating pressure in practice is required to be 10^{-4} Pa. At this level it can be modelled onto the system due to its predictable linear effect on the g measurements, whilst the pressure less than 10^{-5} Pa can be negligible during measurement (Torge, 1989).

The required operating vacuum pressure was pre-determined through numerical evaluation of the error induced by drag force on the test mass and g measurements. Operating pressure was obtained using the mathematics formulae discussed in the following paragraph.

The true gravitational acceleration (g) when measured using free fall gravimeter in the perfect vacuum, depends solely on the gravity force field. However the perfect vacuum is impracticable, therefore the presence of the air particles available in the vacuum chamber results with air resistance friction on to the free-falling test mass. The acceleration measured is the result of the resultant force (F_{Res}) acting on the test mass. To realise g , an error due to drag should be compensated on measured gravitational acceleration at the operating vacuum pressure. The g value of 9.786098 m/s^2 is used in this model. The drag force (F_D) reduces the test mass'

acceleration resulting with resultant acceleration (a_{Res}). F_{Res} is dependent on the mass (m) of the test mass and (a_{Res}). The relationship of this force system is provided by Equation (5-1) :

$$F_{Res} = F_g - F_D \quad (5-1)$$

$F_g = mg$	$F_D = \frac{1}{2} \rho A C_d V^2$ ρ : Air density A : Test mass surface area C_d : Drag coefficient V : Test mass velocity	$F_{Res} = ma_{Res}$
------------	--	----------------------

The drag force depends on the operating vacuum chamber pressure and the velocity of the test mass. The highest velocity the test mass can achieve, was determined ideally using equations of motion to be 2.2027 m/s. This velocity is used to determine the maximum possible error, assuming the test mass maintains the highest velocity in the vacuum chamber results with the highest drag force.

The air density in the vacuum chamber is calculated using the ideal gas equation, related to air density of the operating vacuum chamber pressure P , air temperature T and ideal air constant R .

$$\rho = \frac{P}{T R} \quad (5-2)$$

Table 5-1 indicates the calculated resultant measured acceleration, at pressure 10^{-4} Pa, the resultant acceleration of the test equals the gravitational acceleration used in the model, indicating that the error at that pressure has negligible effects.

Table 5-1: Gravitational acceleration error calculation as a function of vacuum chamber operating pressure

Pressure [Pa]	Density [Kg/m ³]	Drag Force [N]	Resultant Force [N]	a_{Res} [m/s ²]
100000	1.169	1.08×10^{-2}	0.12624276	9.017340
10	1.169×10^{-4}	1.08×10^{-5}	0.13704629	9.789021
0.1	1.169×10^{-6}	1.08×10^{-8}	0.13704736	9.789097
1.0×10^{-4}	1.169×10^{-9}	1.1×10^{-11}	0.13704737	9.789098
1.0×10^{-7}	1.169×10^{-12}	1.1×10^{-14}	0.13704737	9.789098

NMISA DFFG-01 prototype as reported in this study, had limitations due to the vacuum chamber constructed. Dead corners prevented the attaining of lower operating pressure. The time constraints on the academic programme duration limited the improvement of the vacuum chamber manufactured to enable attainment and control of the operating vacuum pressure. The lowest vacuum pressure attained was 0.05 Pa. The PFEIFFER D-35614 turbo-molecular pump was used.

The pump has a maximum pumping capacity of 10^{-5} Pa. Experimental evaluation of operating pressure effect on measured gravitational acceleration were performed with measurements at different controlled operating pressure. Table 5-2 and Figure 5-3 shows the results of the evaluation analysed using 20 drops at each operating pressure.

Table 5-2: Gravitational acceleration measured whilst controlling the vacuum chamber pressure

Operating Pressure [Pa]		Measured g [m/s^2]	Standard deviation [m/s^2]
0.05	P1	9.7864	0.0008
0.1	P2	9.7882	0.0026
0.5	P3	9.7884	0.0024
1	P4	9.7874	0.0022
10	P5	9.7875	0.0015
50	P6	9.7874	0.0020
100	P7	9.7873	0.0015
1000	P8	9.7875	0.0023
10000	P9	9.7869	0.0023
100000	P10	9.7805	0.0025

Figure 5-3 indicates the measured gravitational acceleration with the standard deviation as the error bars calculated at each operating pressure.

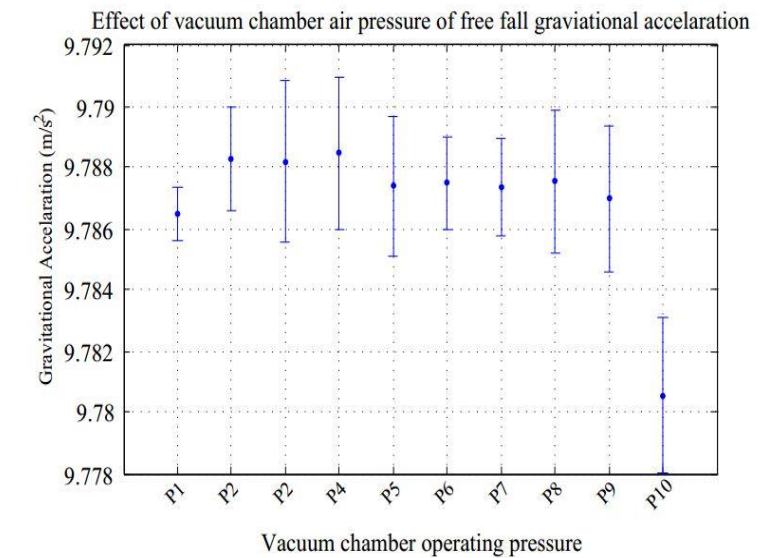


Figure 5-3: Gravitation acceleration measured at different operating vacuum chamber pressure

Figure 5-3 indicates the increase in the chamber pressure result with the increase in drag resistance on the test mass. The gravitational acceleration decreases at high vacuum operating pressure with the measurements standard deviation increasing.

5.2 NMISA DFFG-01 results

The test pressure of 0.05 Pa was used to evaluate effects of the position or the velocity of the test mass. This experiment was set to evaluate whether various signal frequency magnitude produced at different projectile heights produced changed measurements. The three displacement-time coordinates were selected from various heights corresponding to the free fall signal. This experiment was also performed to experimentally evaluate the effect of linear interpolation over the entire signal frequency. During the projectile, velocity increases from the moment of release, therefore the signal frequency also increases. The accuracy of zero detection is affected due to change in frequency. Gravity gradient was also investigated during these experiments.

The total falling height of 0.2 m was divided into five segments, Segment 1, 2, 3, 4 and 5. Segment 1 corresponds to 10 to 20% of the intensity signal after the digital trigger –the segment percentage does not relay the percentage of the falling height but the percentage of the size of the analysed signal. Frequency trigger from 2.5 to 12.5 MHz zero-crossing frequency was set to crop the total signal to be used in the analyses. This is labelled point A and B respectively on Figure 5-4. Segments 2, 3, 4 and 5 correspond to 25 to 35, 45 to 55, 60 to 70, and 70 to 80% of the intensity signal respectively. The full range corresponds to 10 to 80 % of the signal.

The three displacement-time coordinates were taken from each signal segment according to Figure 5-4 and each segment's g value was calculated. The letter R and C represents the test mass release and capture point position respectively, whilst A and B represents points where the intensity signal is cropped to be processed.

Segment	Displacement-time coordinates		
	z_1, t_1 (%)	z_2, t_2 (%)	z_3, t_3 (%)
1	10	15	20
2	25	30	35
3	45	50	55
4	60	65	70
5	70	75	80
Full range	10	50	80

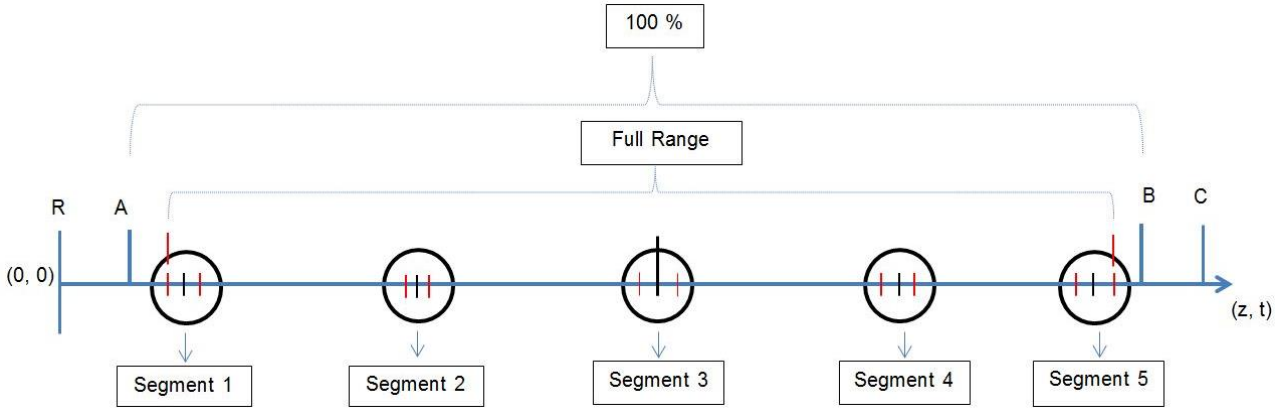


Figure 5-4: Segments used in evaluating the effect of the signal frequency on the calculated gravitational acceleration and measurements standard deviation

The six sets of measurements used during these experiments, were the final measurements reported for this study. The set were processed for mean gravitational acceleration and standard deviation, whilst processed in each segment. Figure 5-5 and Figure 5-6, represent the gravitational acceleration and standard deviation calculated from each set.

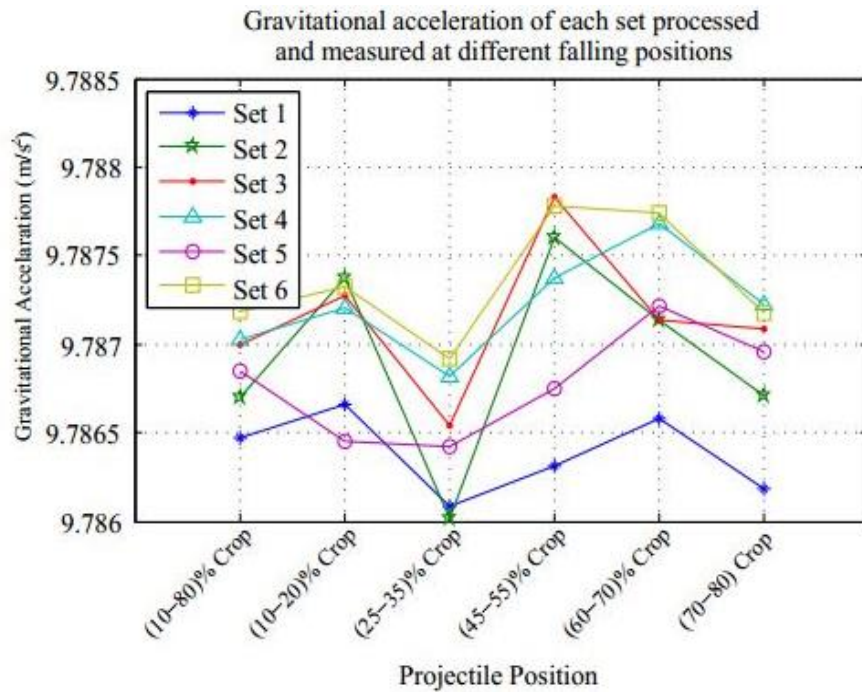


Figure 5-5: Gravitational acceleration of set signals, analysed at different falling positions

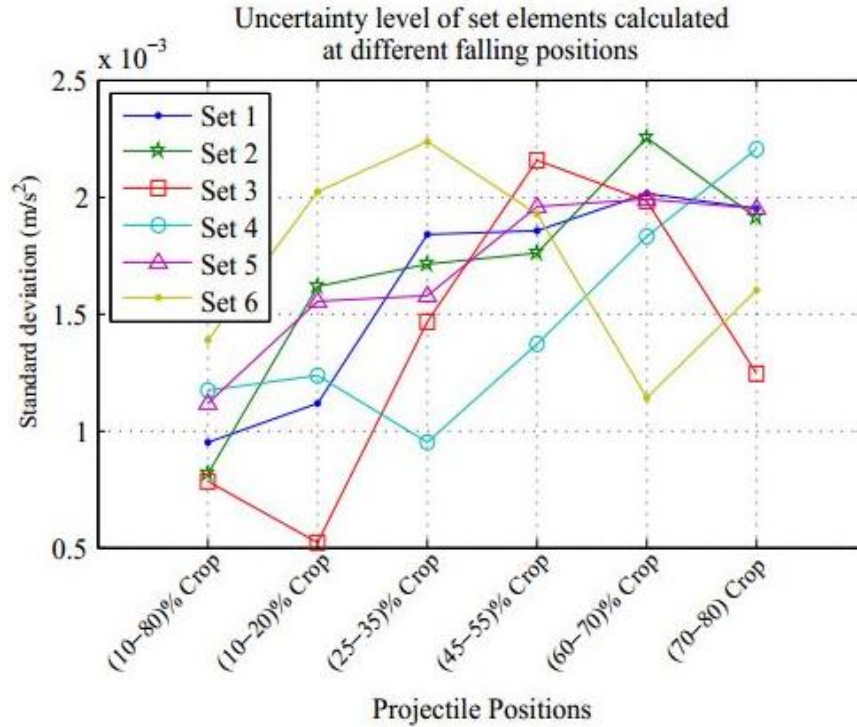


Figure 5-6: Standard deviation of set signals analysed at different falling positions

The full range signal was adopted for further signal processing to realise gravitational acceleration measured using the prototype. The mean gravitational acceleration is observed to be constant as indicated in Figure 5-5. The gravity gradient could not be observed from the current measurements. Figure 5-6 indicates that the average standard deviation of the measurements and full range segment is observed to have the lowest measurements variation. The standard deviation increases with increasing signal frequency. At high frequency zero crossing detection error is increased also the signal is mapped inaccurately.

Peaks and valleys of the intensity signal were detected instead of using the zero-crossings method. The two methods were implemented in LabView. The trajectory displacement change was mapped with a resolution of $\lambda/2$ instead of $\lambda/4$ from zero-crossing method. The results of the three methods were compared. Figure 5-7 indicates the gravitational acceleration and standard deviation of the measurements analysed using zero crossings, peaks and valleys detection.

Processing method	Gravitational acceleration [m/s ²]	Standard deviation [m/s ²]
Zero-crossing ZC	9.786885	0.000217
Peak detection P	9.786746	0.000198
Valley detection V	9.786748	0.000200

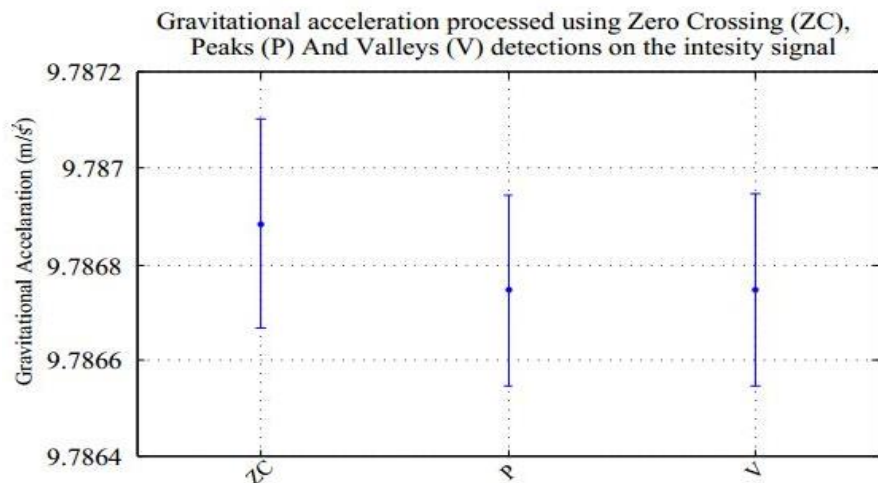


Figure 5-7: Comparison of the three-processing method used on NMISA DFFG-01

The results of the peak and valley detection showed comparable results to each other. The resolution of the displacement detection guided the final decision to use the zero-crossing as the decrease in gravitational acceleration could not be substantiated as observed using peaks and valleys detection. Table 5-3 reports the final results of the prototype measurements.

Table 5-3: Gravitational acceleration measurements drops performed at 0.05 Pa pressure during day time on the isolation table

Gravimeter operating conditions					
Operating pressure [Pa]		0.05			
Time of the day		Day time			
Set	Number of drops	Measured g [m/s ²]	Standard deviation [m/s ²]	Average Error [-]	
1	19	9.78638	0.00089	3.523x10 ⁻⁵	
2	17	9.78679	0.00086	6.068x10 ⁻⁶	
3	15	9.78704	0.00087	3.204x10 ⁻⁵	
4	16	9.78682	0.00092	9.908x10 ⁻⁶	
5	16	9.78650	0.00066	2.342x10 ⁻⁵	
6	15	9.78683	0.00133	1.062x10 ⁻⁵	
Inclusive average [m/s ²]		9.78673	0.00092	1.951x10 ⁻⁵	
Set's 'g' standard deviation [m/s ²]					0.00022
g = 9.78673 ± 0.00022 m/s²					

5.3 Results comparisons and validations

During the process of the prototype development, two techniques of validation of measurements were used:

- Normal gravity equation defined on ellipsoid shape of earth (Universal gravity equation).
- Gravimeter from the Council for Geoscience, Pretoria.

5.3.1 Universal gravity equation

The universal gravitation equation is used in geophysics to roughly determine the gravitational acceleration of any location around the earths' surface as the function of latitude (L) and Height (H) above sea level of the location of interest. This equation holds an accuracy of 0.5 % to the true value of the gravitational acceleration (NPL, 2007).

$$g = 9.780327[1 + A \sin^2(L) - B \sin^2(2L)] - (3.086 \times 10^{-6}H) \text{ [m/s}^2\text{]} \quad (5-3)$$

where $A=0.0053024$ and $B=0.0000058$

The prototype is stationed at the CSIR, building 5, the latitude of 25.74680946° south and height of 1373 m above sea level. The gravitational acceleration is calculated using Equation (5-3) to be:

$$g = 9.78582 \pm 0.00049 \text{ m/s}^2$$

This value was used as rough estimation guide during the development when initial measurements were performed.

5.3.2 Council for Geoscience gravimeter

The Council of Geosciences, Pretoria is responsible for measuring gravitational acceleration for NMISA laboratories. The decision for the Council of Geosciences to perform the measurements, allowed the comparison of concurrent measurements value of gravitational acceleration with the value measured using our prototype.

The result of the measurements performed by the Council of Geosciences using a relative gravimeter, CG-5 Autograv, is:

$$g = 9.7860981 \pm 0.0000005 \text{ m/s}^2$$

5.3.3 CG-5 Autograv VS NMISA DFFG-01

Table 5-3 reports the NMISA DFFG-01 measurement results, measured with the NI-USB system setup. The NI-USB digital card was used as a primary design acquisition card during the development. Figure 5-8 indicates the results of this setup, compared to the measured gravitational acceleration discussed in Sections 5.3.2 with the error bars showing the standard deviation calculated in Table 5-3.

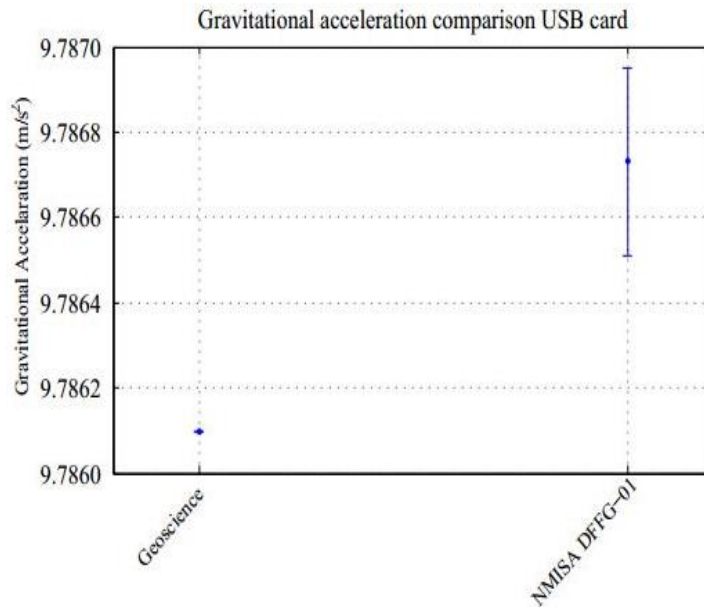


Figure 5-8: Gravitational acceleration comparison graph with uncertainty measurements

The gravitational acceleration measured using the prototype is greater than the measured value by the Council of Geoscience certified gravimeter by $6.315 \times 10^{-4} \text{ m/s}^2$. The standard deviation bar calculated for the prototype did not cover the true NMISA gravitation acceleration value. This was evaluated to confirm the finding as the results indicated that the system measured erroneous gravitational acceleration.

Further prototype evaluation was performed to confirm the measured results; a different digitising card was used. This was performed by acquiring the intensity signal with a higher bit resolution card with a more stable accurate clock. During the change of the digitising card, a different vibrometer controller was used, due to the difficulties using the initial vibrometer in the NI-USB system setup. The vibrometer then formed a new system component to be evaluated.

5.4 System improvements

The processing method used in analysing the intensity signal produced, required accurate detection of zero-crossing time coordinates; the displacement is mapped and reconstructed using these time coordinates. The accuracy in detecting these coordinates depends on the parameters of the electronics for signal acquisition. The sampling rate, bit resolution and timing module of the digitiser, were significant in mapping the time-voltage intensity signal, resulting with an improved realisation of time-displacement data, used to realise gravitational acceleration (Svitlov et al., 2012).

Results reported in Section 5.2 were measured using a NI-USB 5133 digitising card with 100 MHz sampling rate at 8 bits resolution. The decision was taken to evaluate the prototype with more accurate improved digitising card PXI-5122 with 100 MHz sampling at 14 bits resolution and with improved on-board timing module. Higher bit resolution would thus improve detecting zero-crossings, as the intensity signal is mapped accurately (D'Agostino et al., 2004).

Using a PXI-5122 card was expected to produce improved results, due to improved bit resolution and sampling clock. The two-digitising cards were tested and compared to each other to evaluate their differences. In the experiments the effect of bit resolution was practically evaluated on the two digitising cards, USB and PXI, by storing a single fringe signal from a single drop using both the cards. Ten drops were launched. The signals were stored separately. The signals were processed to compute gravitational acceleration and standard deviation. Figure 5-9 indicates the results from this experiment.

Drop	USB [m/s²]	PXI [m/s²]
1	9.78608	9.78605
2	9.78516	9.78514
3	9.78668	9.78665
4	9.78530	9.78529
5	9.78510	9.78507
6	9.78638	9.78642
7	9.78549	9.78546
8	9.78481	9.78477
9	9.78826	9.78824
10	9.78514	9.78514
Mean [m/s²]	9.78584	9.78582
Standard deviation [m/s²]	0.000994	0.000999

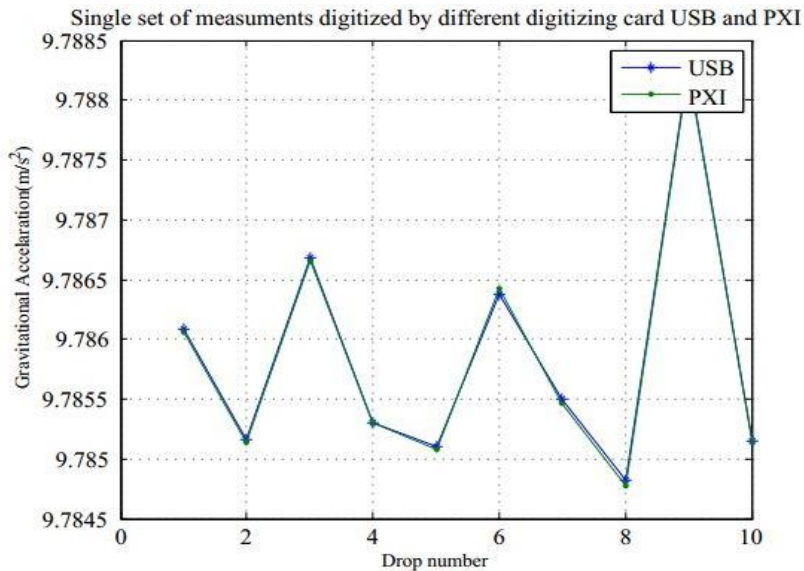


Figure 5-9: Gravitational acceleration computed from intensity comparison of the USB and PXI

The two digitising cards indicated agreement in the measured acceleration, with the different cards averaged to five parts in 10^5 m/s^2 . The uncertainty error of the two signals is averaged to six parts in 10^7 . Deducing from these findings, the bits difference of the two digitising cards does not have a major effect in realising the gravitational acceleration at the accuracy attained by the prototype at the current setup.

In evaluating the higher bit resolution card, a different OFV 5000 vibrometer controller to the initially used during USB setup was used for the PXI setup. The improvement in the results was then deduced to depend on the controller module. For the purpose of this study, it was decided to name the controller used with the USB digitising card with results discussed in Section 5.2, CUSB and the controller used in the experimental results of the current Section 5.4, CPXI.

The evaluation of the simulation algorithms were validated by fitting the actual drop displacement to the ideal models used in the simulations. The residual of the actual displacement against the ideal displacement was plotted and the results indicate that the actual measurement deviates from ideal model, the ideal graphs from the model are shown in CHAPTER 4. The model which was used assumes ideal free fall. The graph showing the comparison of the ideal and actual displacement plot is shown in Figure 5-10.

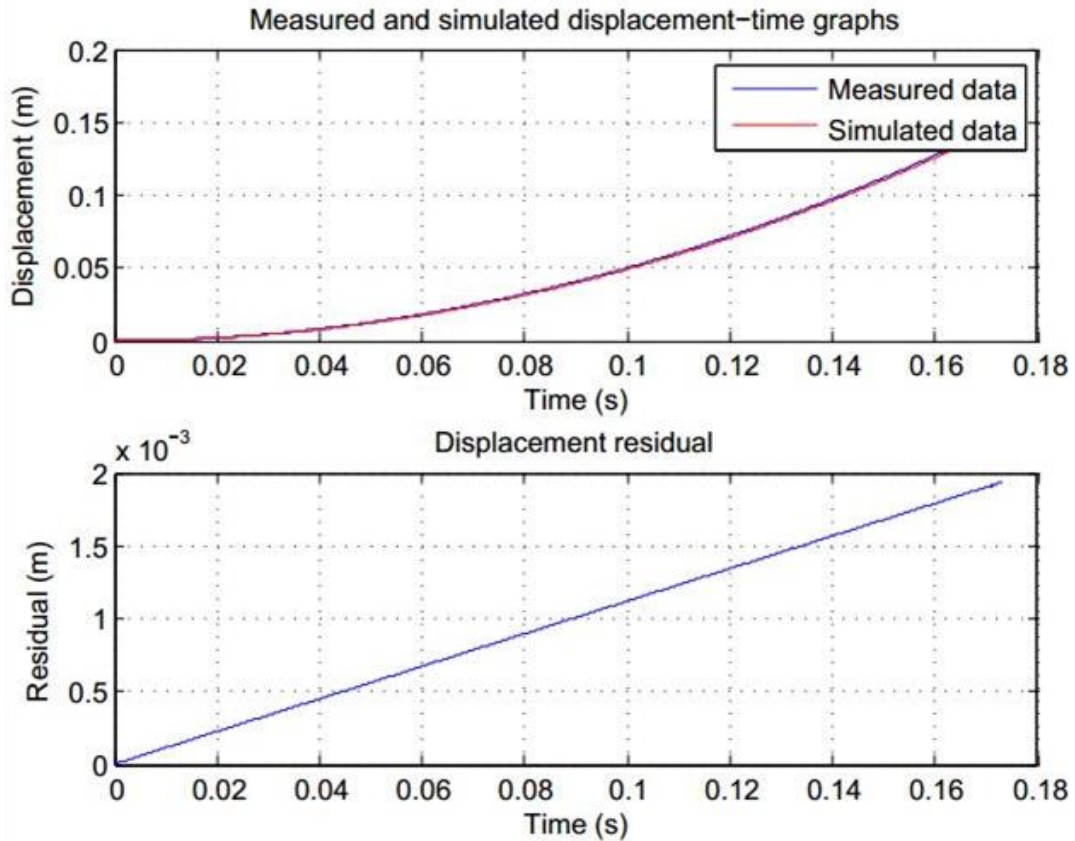


Figure 5-10: The displacement-time residual graph

During the CPXI prototype setup evaluation process, vacuum chamber stable operating pressures ranging from 0.05 Pa to 2.5 Pa were achieved. The results from these experiments indicated improved standard deviation in sets measurements with decreasing vacuum chamber operating pressure, also improved realisation of the true site's gravitational acceleration value was achieved.

The comparison of results at each operating pressure were within uncertainty error with each other at different operating pressure with an increase in gravitational acceleration and reduced standard variation in set measurements when the pressure decreased. This observation was expected, as randomness air particle movement was reduced at lower pressures. Figure 5-11 indicates the results of the experiments using CPXI.

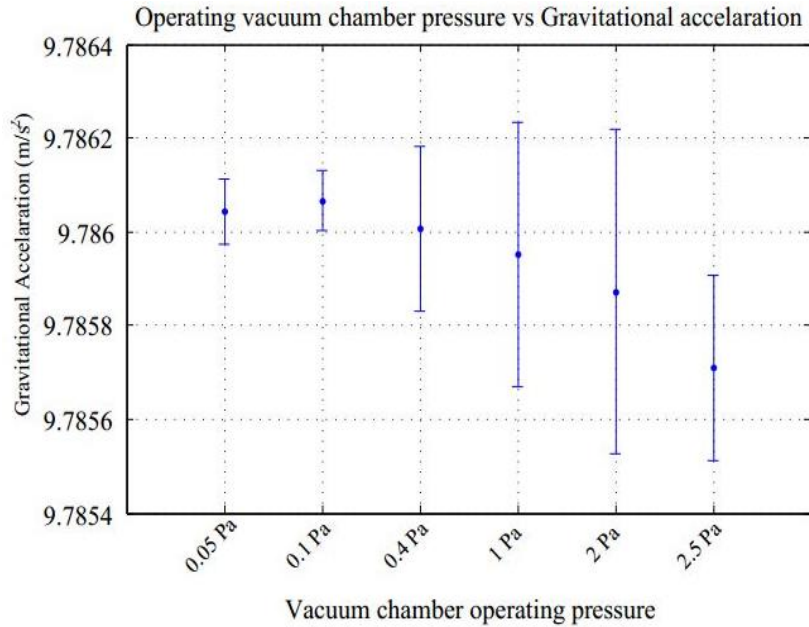


Figure 5-11: Gravitational acceleration comparison graph with uncertainty measurements over changing operating pressure

Table 5-4 indicates the experimental measurements performed were considered the best system measurements for the prototype at the vacuum chamber operating pressure of 0.05 Pa.

Table 5-4: Gravitational acceleration measurements performed at 0.05 Pa pressure during day time on the isolation table using PXI digitising card

Gravimeter operating conditions				
Operating pressure [Pa]		0.05		
Time of the day		Day time		
Set	Number of drops	Measured g [m/s ²]	Standard deviation [m/s ²]	Average Error [-]
1	8	9.78616	0.00128	1.208x10 ⁻⁵
2	9	9.78594	0.00063	9.908x10 ⁻⁶
3	8	9.78606	0.00122	2.046x10 ⁻⁶
4	8	9.78597	0.00065	6.758x10 ⁻⁶
5	8	9.78608	0.00075	3.992x10 ⁻⁶
6	9	9.78602	0.00087	1.450x10 ⁻⁶
Inclusive average [m/s ²]		9.78604	0.000905	6.039x10 ⁻⁶
Set's 'g' standard deviation [m/s ²]				0.0000705
g = 9.78604 ± 0.0000705 m/s²				

Figure 5-12 indicates the improvement in the standard deviation of measurement sets reaching up to seven parts in $10^5 m/s^2$. The results of the prototype measurements as compared to the true measured NMISA site's gravitational acceleration are comparable.

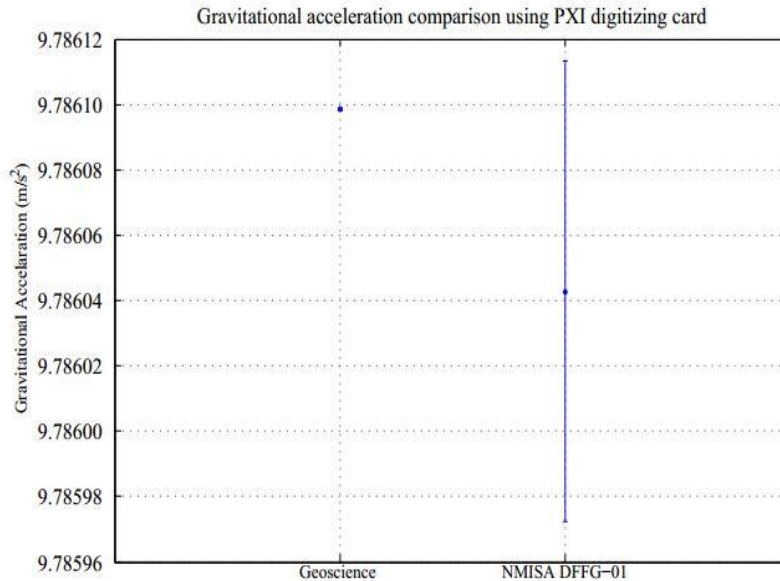


Figure 5-12: Gravitational acceleration comparison graph with uncertainty measurements

The gravitational acceleration results comparisons of NMISA DFFG-01 and CG-5 Autograv indicates measurement agreement with an error of 5.5 parts in a million parts.

The gravimeter performance parameters are given in Table 5-5. These are based on the accuracy of the agreement of the measurements and precision of the gravimeter as a parameter based on the time spent performing measurements.

Table 5-5: Performance specification

Accuracy		$59\mu m/s^2$
Precision	3 minutes	$9.05 \times 10^{-4} m/s^2$
	8 hours	$7.05 \times 10^{-5} m/s^2$

The two-system setup CUSB and CPXI displayed large differences in measuring the true gravitational acceleration from similar gravimeter operating conditions. Both the measured gravitational acceleration and standard deviation of the measurements fluctuated between the two setups.

The comparison of the two final results using both methods, is indicated in Figure 5-13. In the CUSB setup, higher g value was measured and set standard deviation of a few parts in 10^4 m/s^2 , whilst in CPXI, comparable g value lower than the true measured value was measured. The prototype calculated also an improved measurement standard deviation of a few parts in 10^5 m/s^2 .

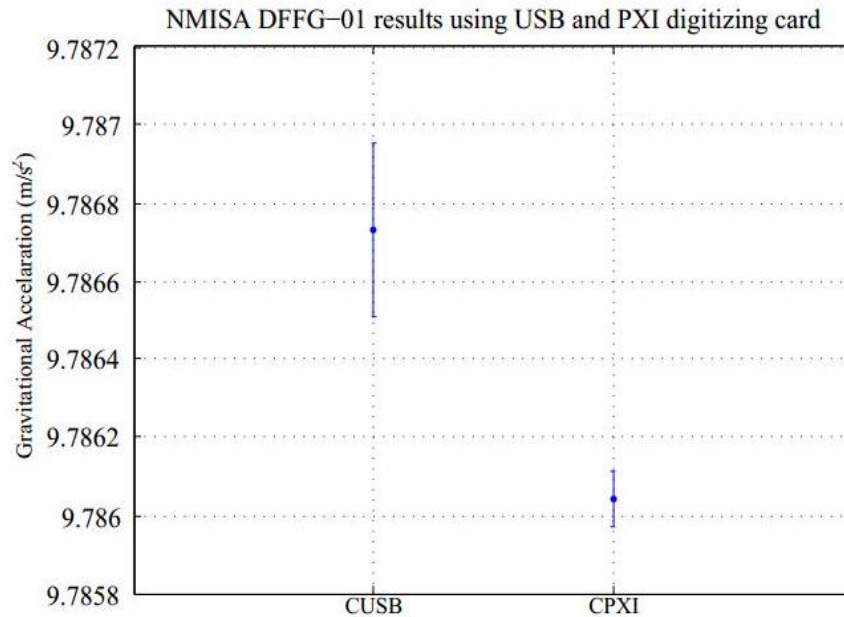


Figure 5-13: CUSB and CPXI measured gravitational acceleration value and their standard deviation

The CPXI results were captured as the final prototype results and the outcome of the project. The reduced measurement deviation and the comparable results to the true sites measure g value by the geosciences gravimeter guided the conclusion on the results from the CPXI measurements.

5.5 Prototype results discussions

The NMISA DFFG-01 gravimeter comprised five sub-systems, continuously developed and tested as part of this project. Each system required analyses and evaluations to investigate its effect onto the system, whilst the other sub-systems were controlled. This was not performed on the work presented in this study; only the vacuum chamber was provided and focussed on, as it formed the base topic of this study.

The initial experimental results presented in Section 5.2 were the first prototype tests. The response of the system under various operating pressures using CUSB setup displayed unexpected system performance. Gravitational acceleration decreased with the decrease in operating pressure. This observation indicated that system had an unreliable response. The decrease in vacuum chamber decreased the drag force on the test mass, therefore gravitational acceleration must increase.

Measurements performed using CPXI, indicated a positive system response to the operating pressure. The drag force decreased in the vacuum chamber, gravitational acceleration increased and standard deviation of the measurements also decreased.

The mathematical modelling of gravitational acceleration as a function of pressure, was constructed using the operating pressure testing the prototype. Figure 5-14 indicates the response of this model, compared to the actual prototype CPXI response.

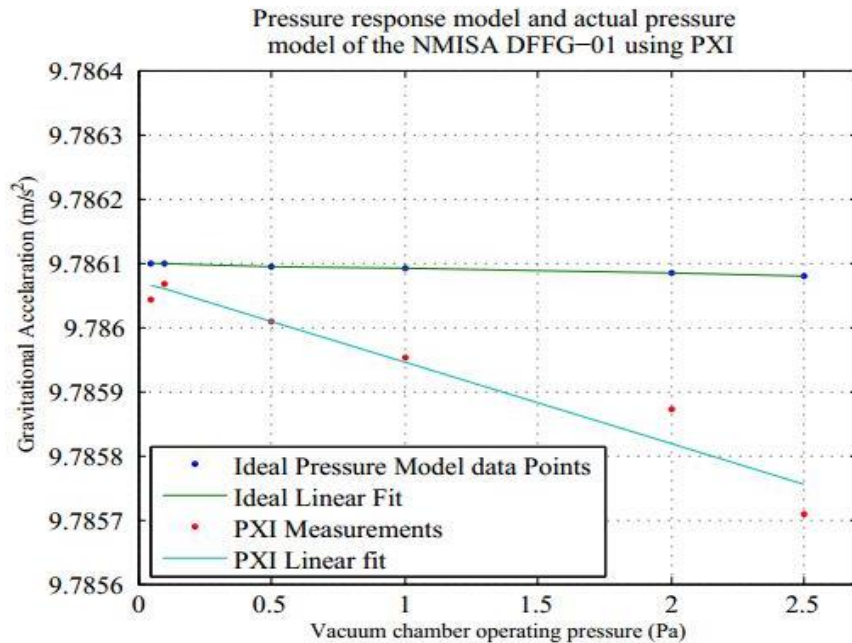


Figure 5-14: Pressure comparison graph of actual measurements performed using the prototype and CPXI system setup with variation in pressure

Figure 5-14 indicates fitted linear model through data points of CPXI measurements. The fitted model is represented by the equation $g_{CPXI} = -0.000126 P + 9.7860713 (m/s^2)$, where P represented the vacuum chamber operating pressure. The slope of the ideal pressure model and CPXI liner fit is different. The differences result because of the additional systematic uncertainty contributors of the erected prototype. CHAPTER 6 discusses these contributing factors projected for investigation evaluation for future.

NMISA DFFG-01 indicated several systematic challenges, resulting with large variation in the measurements. In Section 5.1, the operating pressure effect of the CUSB digitising card setup was evaluated. The setup indicated that the decrease vacuum chamber pressure resulted from the increase in gravitational acceleration beyond the true g value at NMISA, further decreased, indicating a sudden decrease on measured g value with improved measurement standard deviation. However the lower error bar covered the true g value of the site. The results from this experiment

were not conclusive to deduce any meaningful behaviour of the prototype. The results from Section 5.3 Table 5-3 are not conclusive and could not be used in concluding the prototype measurements results.

The measurements performed by the CPXI digitising card were taken with a different vibrometer controller, for results reported in Section 5.4. The two vibrometer controllers used as described in Section 5.2 and 5.4, indicated inconsistency in measuring the gravitational acceleration on the same location. After evaluating the two digitising cards, it was concluded that the two vibrometer controllers held operational differences.

The vacuum chamber was designed and constructed, enabling the mounting of the actuating gripper mechanisms, whilst factors such as dead corners of the chamber were not considered. Minor vacuum chamber leaks caused difficulties in vacuum pressure control; constant vacuum could not be maintained during vacuum measurement. The vacuum chamber construction materials were not prepared for application, this factor might have had a huge impact on the pressure in our system, through the process of degassing of the vacuum exposed surfaces. The coupling of the vacuum pump to the vacuum chamber resulted with high vacuum chamber structural vibration.

Systematic errors associated with free fall gravimeters as outlined in Section 2.4, were not considered in the current manufactured prototype, as their uncertainty effect on the gravitational acceleration were noticed at levels in a few parts of 10^8 (Rothleitner, 2008). The uncertainty of measurement on the NMISA DFFG-01, is at the level of few parts in 10^5 of gravitational acceleration. The system improvement aimed at improving the current mechanical challenges before addressing the systematic errors. Systematic malfunctions and errors were noted for future development and investigation. CHAPTER 6 discusses these errors; corrective measures are suggested.

CHAPTER 6

Conclusions and recommendation

The free fall gravimeter prototype designed, tested and constructed at NMISA marks the first step in the development plan for research in support of the watt balance project underway. The prototype is continuously evaluated and developed. These evaluations are centralised on the various sub-systems of the project, mechanical design, interferometry setup, isolation system, software and electronics support components.

Chapter 5 presents the results from the initial experimental tests results. This chapter documents the conclusions and recommendations for future work based on the findings of the current system.

6.1 Conclusions

The prototype was conceptualised, designed and constructed as a possible solution for NMISA to support the research mandated by the organisation. This project covered a large spectrum of scientific research disciplines. As a result, components of the project were not covered in-depth because of the time constraints and deliveries for the academic programme. The lack of expertise in various fields, capabilities and knowledge on gravimetry at NMISA limited the full system evaluation and development.

The current study reported the direct free fall gravimeter that uses the pneumatic power actuator to control all mechanical movement of the invented vacuum chamber. The vacuum chamber semi-rotates, enabling tests mass repositioning using both grippers to allow the continuous gravitational acceleration measurement through a complete 180° rotation. The vacuum chamber conceptualised for this project resulted with the implementation of the double-sided test mass. The double-sided test mass enhanced the rate experimental drops were performed by a factor of two, compared to single side retroreflector mounted test mass, used in the designed vacuum chamber.

The use of pneumatic actuators as the resolution to remove using electrical actuators around the test mass and the vacuum chamber was successfully implemented. This design provides a total removal of all sources of the electromagnetic forces around the vacuum chamber.

The concept has indicated the potential for further development for the organisation as a gravitational acceleration measurements system. The final NMISA site gravitational acceleration measured using the prototype of 9.78604m/s^2 was achieved with the standard deviation of 0.0000705 m/s^2 . The true value of the gravitational acceleration of the experimental site is within the standard deviation of the measured value, using the prototype.

6.2 Recommendations

During developing of the NMISA DFFG-01, systematic difficulties were encountered and noted as challenges for future development. The system requires collective sub-system evaluation and development. As the researcher, designer, manufacturer, constructor and tester of this system during this study, several systematic requirements in most literature were learnt. Using experience gained during this study, and inputs from skilled individuals about various methods that can be used to improve the system, several ideas are outlined for investigations. These ideas require in-depth evaluations.

6.2.1 Vacuum chamber pressure regulation and control

The vacuum chamber constructed, included several design blunders, identified during system evaluation. The pump used was tested prior to the system evaluation to check if it can attain its maximum pumping capacity. Tests indicated that the pump could attain 10^{-5} Pa . When the pump was coupled to the vacuum chamber, the best lowest pressure of 10^{-2} Pa was achieved. To improve the vacuum chamber, the design must avoid dead corners. This could be achieved by designing dome ends vacuum chamber and the size of the vacuum chamber must be minimised. This will improve the time taken during system evacuation.

The current system setup results indicated that the operating vacuum chamber pressure has a direct detectable effect on the system measurements. Figure 5-11 indicates the effect of the operating pressure on the free fall motion of the test mass. Reducing the vacuum chamber operating pressure result reduces the variation of measurements and improves the realisation of the measured accelerations.

The pressure maintenance, regulation and control method need to be robust during testing. The feedback controllable vacuum pump is required for controlling and maintaining the pressure level. The method used, required the operator to observe the pressure sensor head, and either start or stop the measurements when predefined vacuum pressure thresholds were achieved.

6.2.2 Mechanical improvements

The mechanical design of the prototype must first address safety aspects of usage by any trained personnel. Operational safety was not evaluated on the prototype designed.

The prototype designed used multiple small mechanical parts identical for the test mass gripping jaws. These components were not manufactured accurately due to the lack of experience and capabilities on the side of the author in the manufacturing procedures used. The vacuum chamber constructed, had undetectable air leakages that could have been avoided by using correct vacuum components manufacturing procedures.

Experienced manufacturing laboratories must manufacture the components where precision is important, especial in metrological purposes. This is a mechanical manufacturing priority requirement as the test mass will be released from two independent grippers. The two grippers identically release the test mass; this will reduce the measurement variation due to their independency.

Mechanical components reduction and systems manufactured from multiple components often result in misaligned components. Three-dimensional manufacturing capabilities must be used to manufacture complex parts. The gripper jaws in the current prototype used multiple components in which certain components were redundant. The components could be removed from the setup with minor modification of other components.

The method of using tapered cones to gently capture the test mass must be reviewed and improved as it showed the good characteristics in handling the test mass. The correct taper angle of the cone needs to be determined to allow gentle test mass capturing without inducing high impact loads. Using a damaged test mass may result in unwanted rotation and translation motions of the test mass during a fall.

The vacuum chamber must be manufactured from aluminium material, however this must be prepared for vacuum service. The current prototype uses a Perspex vacuum chamber body; the limitation from this chamber is that it is sensitive to localised impact forces. These forces can cause damage that can result in remanufacturing of the vacuum chamber as the cracks propagate easily in brittle plastics. The body of the vacuum chamber upon completion of a reliable fully functional system must avoid the use of Perspex but use aluminium.

The vacuum sensors on the current setup were mounted on the suction line 0.5 m from the vacuum chamber. The vacuum monitoring sensors must be mounted on the vacuum chamber to allow accurate vacuum chamber pressure detection and control.

The mechanical design of the vacuum chamber should be reviewed to improve the ergonomic factors directed at assembling and disassembling the vacuum chamber to have access to the test mass. This must ensure that the procedure of placing the test mass into the vacuum chamber does not result in total disassembling of the vacuum chamber. Disassembling the vacuum chamber can result in alteration and misalignment of the grippers.

The stand of the vacuum chamber was directly attached to the vacuum chamber using bearings. The stand was designed with a three-standing leg. Adjustment and levelling was performed using these legs. The method of levelling the gravimeter of the current prototype was not robust. It is recommended that the structure and the vacuum chamber contain their own adjusting station. This would simplify the alignment during system setup.

The current system is mechanical overdesigned. For future work, vacuum chamber design must be optimised with finite element analyses prior to manufacturing. This would improve the system by reducing vacuum chamber weight, allowing improved vacuum chamber control through the rotary actuator.

6.2.3 Test mass improvement

The current test mass uses a 10 mm retroreflector diameter however only 8 mm of the retroreflector is accessible by the beam during measurements. The laser beam of the current interferometer overfills the retroreflector active area. A bigger retroreflector of diameter 15 mm or 20 mm is recommended for future projects to prevent over-filling of the active area.

Section 3.4 discussed that the OC of both the retroreflectors of the study's test mass would be displaced from its COM. The requirement to coincide the OC and COM on the same location on the test mass, reduces errors due to rotation of the test mass, that cannot be avoided during projectile of free-falling objects. The current test mass design comprises two retroreflectors, mounted on both sides of the test mass. In order to achieve coinciding of the COM and OC, a high tolerance sliding ring around the test mass is recommended to allow changing of the COM of the test mass on the falling axis. A double-sided test mass with a variable position ring around the test mass can be used to enable the variable COM.

6.2.4 Optical system improvement

The method used for aligning the measurement beam leg of the interferometer of the prototype ensured only short-range beam alignment. The plumb line alignment of the beam was manually achieved using a string hanged perfectly in gravitational plumb line, whilst the beam was directed to fall on the path of the string. Using the reflective liquid pool (mercury or ethanol) method for perfect laser alignment in gravity plumb line is recommended (Rothleitner, 2008).

Laser beam diameter control is required, for a beam expander, enabling the accurate control of the beam size, is required on the interferometer to control the beam size and evaluate the effect of the size on the measurements. It was realised that during experiments, various beam dimensions and orientations, such as diverging or converging beams, affected the measurements results. Using parallel beam propagation must be achieved by minimising the divergence or convergence angles.

6.2.5 Electronics and software

The electronic modules used must be evaluated for their accurate measurements capabilities. These sub-systems must be calibrated to ensure that signals acquired were not distorted. The evaluation will ensure that correct compensations were added onto the measurements.

The interferometer system used in the experimental results reported in this study, used a vibrometer controller, filtering the interference signal prior to the acquisition and storage. The filtering technique used by the controller must be evaluated for time delays. The delays must be compensated in the signal processing codes (if found). The knowledge of the fundamental functional procedure of the controller is significant to qualify its measurements.

The method of zero-crossing detection to extract the displacement history of the test mass, introduces an error due to linear interpolation to detect the zero-crossing time. Various sampling frequencies and resolutions must be investigated to evaluate the effect of these parameters on the final free fall gravitational acceleration. The sampling clock embedded in the module for time points stamping must be calibrated against the national standard and compensation must be included in the analyses.

The software used in the prototype was based on a total post-processing method. Labview was used to load the measurements and to process the signal for zero-crossing. The measurements were stored and processed later in time. Improving the procedure of measurements must include concurrent processing, indicating the measured gravitational acceleration. It is recommended that

whilst the measurement data is stored, it must be streamed and analysed immediately after each drop was launched.

6.2.6 The Isolation system

The isolation system in the application of free-falling gravimeters, serves a significant purpose of isolating measurements from the external vibrations. This device isolates the reference mirror from the long-period seismic earth movements and the human induced vibrations. A detailed study of vibration encountered on the system, is needed to determine the parameters required to achieve the isolation.

The interferometer system used during prototype evaluation, includes the reference mirror attached to the sensor head. The design of the isolation system must account for the total weight of the sensor head.

The NMISA DFFG-01 is not a complete product. Numerous system improvements are required to achieve a reliable system, which can be certified for use by any physical metrologist trained to use the system. NMISA is advised to invest resources into improving the system, using the conceptual method implemented.

REFERENCES

- Alasia, F., Cannizzo, L., Cerutti, G. & Marson, I., 1982. Absolute gravimeter acceleration measurements: Experience with a Transportable Gravimeter. *Metrologia*, 18, pp.221-229.
- Ambaum, M.H.P., 2008. General relationship between pressure, weight and mass of a hydrostatic fluid. *Proceedings of The Royal Society*, 464, pp.943-950.
- Amrita, 2011. *Micheloso's Interferometer -Wavelength of laser beam*. [Online] Available at: vlab.amrita.edu/?sub=1&brch=189&sim=1106&cnt=1 [Accessed 16 November 2015].
- Ando, B. & Carbone, D., 2009. A labview environment to compensate temperature-driven fluctuations in the signal from continuously running spring gravimeters. *Computers and Geosciences*, 35, pp.2129-2136.
- Baumann, H., Pythoud, F., Flas, D., Sibiryakov, S., Eichenberger, A. & Klingele, E.E., 2015. *Experimental assessment of the speed of light perturbation in free-fall absolute gravimeters*.
- Beater, P., 2007. *Pneumatic Drives: System Design, Modeling and Control*. New York: Springer.
- Bell, G.A., Gibbings, D.L.H. & Patterson, J.B., 1973. An absolute determination of the gravitational acceleration at Sydney, Australia. *Metrologia*, 9, pp.47-61.
- Bewoor, K.A. & Kulkarni, A.V., 2009. *Metrology and Measurements*. Tata Mc Graw Hill.
- Born, M. & Wolf, E., 2003. *Principles of optics: Electromagnetic theory of propagation, interference and diffraction of light*. 7th ed. Cambridge University Press.
- Bosch, R., 2006. *Rexroth Bosch Electricity, Hydraulic, Pneumatics*. [Online] Bosch Rexroth Corporation Available at: www.dc-america.resource.bosch.com [Accessed 28 April 2015].
- Branan, C., 2002. *Rules of thumb for chemical engineers: A quick, accurate solutions to everyday process engineering problems*. 3rd ed. London: Curl.
- Bucher, J.L., 2012. *The metrology handbook*. Wisconsin: ASQ Quality Press.
- Cook, A.H., 1965. The absolute determination of acceleration due to gravity. *Metrologia*, 1(3), pp.84-113.
- D'Agostin, G., 2008. The new IMG-02 transportable absolute gravimeter: measurement apparatus and applications in geophysics and volcanology. *ANNALS OF GEOPHYSICS*, 51(1), pp.39-49.
- D'Agostino, G., Desogus, G., Germak, A., Origlia, C. & Barbato, G., 2004. A new method to estimate the time-position coordinates of a free falling test mass in absolute gravimetry. *Journées Luxembourgeoises de Géodynamique*.
- D'Agostino, G., Germak, A., Origlia, C. & Quagliotti, D., 2007. *Perturbation in absolute gravimetry*. Turin: National Institute of Metrological Research.
- Darling, D., 2006. *Gravity's Arc : The story of gravity from Aristotle to Einstein and beyond*. New Jersey: John Wiley and Sons.

- Davidson, 1991. *The History of Optics and Interferometry*. [Online] Available at: http://www.phy.davidson.edu/stuhome/cabell_f/diffractionfinal/pages/history.htm [Accessed 05 October 2015].
- Dicke, R.H., Princeton, N.J., Block, B., Pleasant, S., Weber, J. & Chase, C., 1969. Superconducting Gravimeter. *United States Patent office*, 28 January.
- Durando, G. & Germak, A., 2002. A New Method of Acquiring Data of Absolute Gravimeter. *INRIM Istituto Nazionale di Ricerca Metrologica*.
- Dushkina, N., 2014. Fundamentals of Optical elements and devises. *Handbook of optical metrology*, pp.66 -81.
- Faller, J.E. & Marson, I., 1988. Ballistic Methods of Measuring g- the Direct Free-Fall and Symmetrical Rise and Fall Methods Compared. *Metrologia*, 25, pp.49-55.
- FESTO, 2009. *Festo*. [Online] Festo Coparation Available at: http://www.festo.com/net/SupportPortal/Files/286804/Basic_vacuum_Technology_Principles.pdf [Accessed 16 April 2015].
- Francaise, L.M., 2009. *Metrology in France*. [Online] Available at: <http://www.french-metrology.com/> [Accessed 25 April 2015].
- Galilei, G., 1632. *Dialogue Concerning the Two Chief World Systems*. Translated by S. Drake. 1953.
- Geneves , G., 2006. The French watt balance Project. *Simposio de Metrología*.
- Gillot, P., Cheng, B., Merlet, S. & Pereira Dos Santos, F., 2009. The LNE-SYRTE cold atom gravimeter. In *PSL Research University*. Paris, 2009. PSL Research University.
- Greenfield, D., 1999. *How to decide between pneumatic and electrical actuators*. [Online] Automation world Available at: www.automationworld.com [Accessed 28 April 2015].
- Gualini, M.S., 2002. Methods of absolute laser measurements of gravity-constant "g". *Quarterly Sceience Vision* , 8(1), pp.7-18.
- Halliday, D., Resnick, R. & Walker, J., 1993. *Fundamentals of Physics*. New York: John Wiley and Sons.
- Hammond, J.A., 1970. *A laser-interferometer system for the absolute determination of the accelaration of gravity*. PhD Thesis. Colarad: JILA University of Colorado.
- Hariharan, P., 2007. *Basics of Interferometry*. 2nd ed. Sydney: Elsevier.
- Hecht, E. & Zajac, A., 1974. *Optics*. Addison-Wesley Publishing Company.
- Hinderer, J., Crossley, D. & Warburton, R.J., 2007. Gravimetric Methods – Superconducting Gravity Meters. *Elsvier B V*, pp.65-122.
- Hirai, A., Majima, M. & Telada, S., 2014. *Handbook of optical metrology: Principles and Application*. 2nd ed. CRC Press.
- Ilango, S. & Soundararajan, V., 2007. *Introduction to Hydraulics and Pneumatics*. India: Prentice-Hall of India Private Limited.

- IPAC, 1986. *Cool Cosmos*. [Online] Available at: coolcosmos.ipac.calteck.edu [Accessed 29 February 2015].
- Krivts, I.L. & Krejnin, G.V., 2006. *Pneumatic actuating systems for automatic equipment: Structure and Design*. New York: CRC Press.
- Krynski, J., 2012. Gravimetry for geodesy and geodynamics - brief historical review. *Reports on Geodesy*, 92(1), pp.1-16.
- Kuroda, K. & Mio, N., 1991. Correction to interferometric measurements of absolute gravity arising from the finite speed of light. *Metrologia*, 28, pp.75-78.
- Li, S., Han, B., Li, Z. & Lan, J., 2012. Precisely measuring the Planck constant by electromechanical balances. *Elsevier*, 45, pp.1-13.
- Marson, I., 2012. A short walk along the gravimeters path. *International Journal of Geophysics*, 2012, p.9.
- Meyer, T.J., 2006. Miniature freefall Mechanism. *United States Patent*, p.12.
- Nabighian, M.N., Ander, M.E., Grauch, V.J., Hansen, R.O., LeFehr, T.R., Li, Y., Pearson, W.C., Pierce, J.W., Phillips, J.D. & Ruder, M.E., 2005. Historical development of the gravity method in exploration. *Geophysics*, 70(6), p.27.
- Niebauer, T., 2007. Gravimetric Methods - Absolute Gravimeter: Instruments Concepts and Implementations. *Migro-g Solutions*, 3, pp.43-64.
- Niebauer, T.M., Hollander, W.J. & Faller, J.E., 1992. Absolute Gravity Inline measuring Apparatus incorporating Improved operating Features. *Micro-g Solution*, 45(US005351122A), pp.1-18.
- Niebauer, T.M., Sasagawa, G.S., Faller, J.E., Hilt, R. & Klopping, F., 1995. A new generation of absolute gravimeters. *Metrologia*, 32, pp.159-180.
- NPL, 2007. *National Physical Laboratory*. [Online] Available at: <http://www.npl.co.uk/> [Accessed 25 Augustus 2016].
- Orfanidis, S.J., 2010. *Introduction to Signal Processing*. Pearson Education.
- Prede, G. & Scholz, D., 1997. *Electropneumatics*. Festo Didactic.
- Ritola, D., 2014. *Electronic Controls Deliver Precise Pneumatic Motions*. [Online] Available at: <http://www.hydrolicspneumatics.com> [Accessed 28 April 2015].
- Rothleitner, C., 2008. *Ultra-High Precision, Absolute Earth Gravity Measurements*. Dissertation. Max Plank Research Group.
- Rothleitner, C. & Francis, O., 2010. On the influence of the rotation of a corner cube reflector in absolute gravimetry. *Metrologia*, 47, pp.567-574.
- Rothleitner, C., Niebauer, T.M. & Francis, O., 2014. *Measurements of the speed of light perturbation of free-fall absolute gravimeters*. Luxembourg: Micro-g Lacoste Inc, University of Luxembourg.
- Rothleitner, C., Svitlov, S., Marimeche, H. & Wang, J., 2007. A method for adjusting the centre of mass of a freely falling body in absolute gravimetry. *Metrologia*, 44, pp.234-241.

- Rothleitner, Ch., Svitlov, S., Merimeche, H., Hu, H. & Wang, L.J., 2009. Development of new free-fall absolute gravimeter. *Metropoligia*, 46, pp.283-297.
- Sachie, S., 2008. Testing gravitational physics with superconducting gravimeter. *Progress of Theoretical Physics*, (172).
- Sato, K. & Sano, Y., 2014. Practical and Intuitive controller design method for precision positioning of a pneumatic cylinder actuator stage. *Precision Engineering*, 38(2014), pp.703-710.
- Schlamming, S., Steiner, R.L., Haddad, D., Newell, D.B., Seifert, F., Chao, L.S., Liu, R., Williams, E.R. & Pratt, J.R., 2015. A summary of Planck constant measurements using a watt balance with a superconducting solenoid at NIST. *Metrologia*, 52, pp.L5-L8.
- Schubert, G., 2007. Geodesy: Treatise and Geophysics. *Massachusetts Institute of Technology*, 3.
- Seigel, H.O., 1995. *A guide to high precision land gravimeter surveys*. Toronto: Scintrex Limited.
- Steward, E.G., 2004. *Fourier Optics: An Introduction*. 2nd ed. London: Dover Publications, INC.
- Stock, M., 2011. The watt balance: determination of the Planck's constant and redefinition of the kilogram. *Philosophical Transactions of the royal society*, 369, pp.3936-3953.
- Svitlov, S., Maslyk, P., Rothleitner, Ch., Hu, H. & Wang, L.J., 2010. Comparison of three digital fringe signal. *Metrologia*, 47(2010), pp.677-689.
- Svitlov, S., Rothleitner, C. & Wang, L., 2012. Accuracy assessment of the two-sample zero-crossing detection in a sinusoidal signal. *Metrologia*, 49, pp.413-424.
- Torge, W., 1989. *Gravimetry*. New York: Walter de Gruyter.
- Van Varseveld, R.B. & Bone, G.M., 1997. Accurate position Control of a Pneumatic Actuator Using On/Off solenoid Valves. *Transactions on mechatronics*, 2(3), pp.195-204.
- Walgang, A. & Macdonald, D., 2005. *Practical Process Control for Engineers and Technicians*. Oxford: Elsevier.
- Wallard, A., Magana, M.J.-F. & Squirrell, M.A., 2006. *Common statement and declaration by BIPM, OIML and ILAC on the Relevance of Various International Agreements on Metrology to Trade Legislation and Standardisation*. BIPM; OIML; ILAC.
- Wojtecki, R., 1999. *Air Logic Control for Automated Systems*. New York: CRC.
- Wolfram, S., 2002. *A new kind of science*. Canada: Wolfram Media.
- Zabek, Z., Knap, T. & Kielek, W., 2004. Algorithm for deriving the value of the Earth's gravity using the ZZG ballistic absolute gravimeter. *Metrologia*, 41, pp.414-420.
- Zumberge, M.A., Rinker, R.L. & Faller, J.E., 1982. A portable apparatus for absolute measurements of the earth's gravity. *Metrologia*, 18, pp.145-152.

APPENDICES

Appendix A

Optical path difference

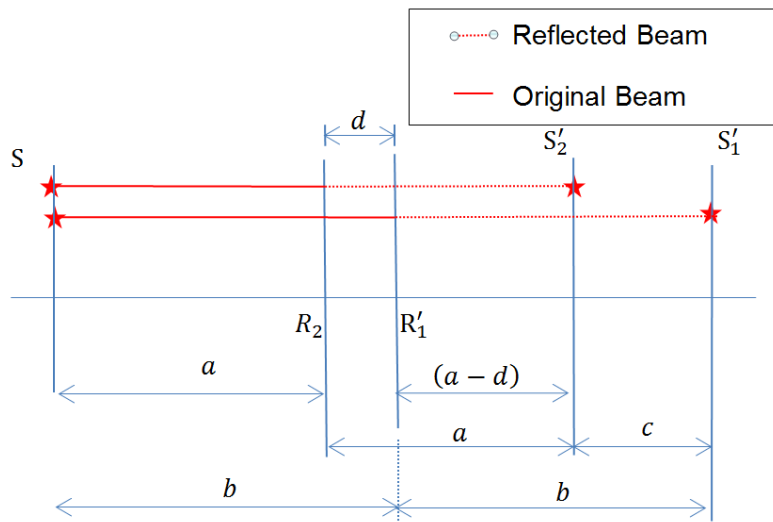


Figure A-1: Geometrical proof of optical path difference

Figure A-1 above is used to prove that the path difference of the two mirror of Section 2.5 is $2d$ if the angle θ_1 is zero, the proof is performed with reference to Figure A-1 above.

$d = b - a$	$c = b - (a - d)$ $= (b - a) + d$ $= 2d$
-------------	--

Appendix B

Vacuum chamber

Gravitational acceleration is computed using the standard of length and time in free-falling experiment. Bodies free-falling with in atmospheric pressure are observed to be falling with different magnitudes of acceleration. This observation is due to air resistance. It has been experimentally proved that objects regardless of their shapes, materials and sizes will fall freely with identical magnitude of acceleration when falling freely in perfect absolute vacuum space. In the absolute gravity measured by free fall methods, vacuum chamber is used to provide vacuum space to aid in removal of air resistance.

In the absolute gravimeter vacuum chamber is therefor used for multifunction, the two main functions are: 1) to generate vacuum space and 2) to position mount the mechanisms used for launching and capturing of the test piece. Other function which the vacuum chamber achieved is to shield magnetic fields during tests (Rothleitner, 2008)

Appendix B is aimed to detail the concepts on the vacuum chamber used in NMISA DFFG-01, which the concept is discussed in CHAPTER 3 Section 3.3 of this study. The positions, motions and control processes of the vacuum chamber are based on the names and symbols defined in this section. The variables used in the controller software are also defined in detail in this section.

Components naming

Table B-1: Vacuum chamber components names

Component	Representation
Vacuum chamber	VC
Gripper 1	G1
Gripper 2	G2

The components defined in Table B-1 are involved on the mechanical operations of NMISA DFFG-1. G_1 and G_2 are responsible for launching, capturing and aligning the test mass. The VC is responsible for reposition the test mass at predefined positions to allow continuous measurements.

Vacuum chamber positions

Vacuum chamber will have two important state positions, position 1 (P_1) and position 2 (P_2) represented as VCP_1 and VCP_2 .

Vacuum chamber movements

The two positions provided above define a state where measurements will be taken during gravimeter operations. Vacuum chamber alternates between these two positions by rotating 180° from one position to the other position. Chamber is rotated 180° in clockwise [CW] (Positive) direction from VCP_1 to VCP_2 and it is rotated 180° anticlockwise [CCW] (Negative) from VCP_2 to VCP_1 enabling the initial state, during the operation, the two positions are the testing states of the gravimeter. The test mass will be launched when the vacuum chamber is at position VCP_1 or VCP_2 ; these positions are indicated in Figure B-1.

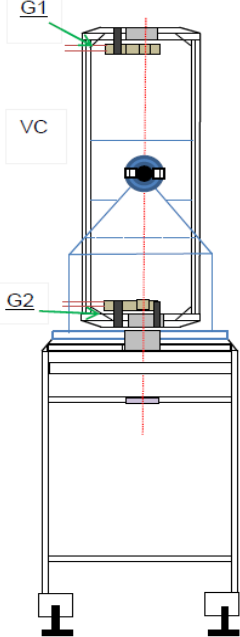
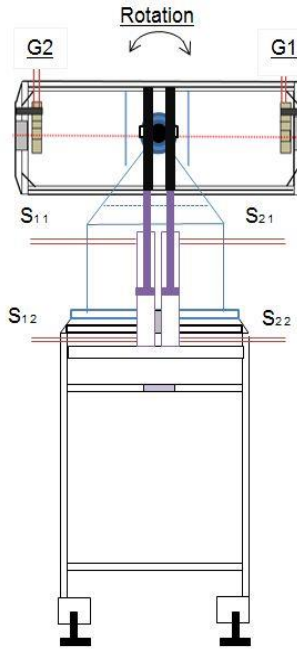
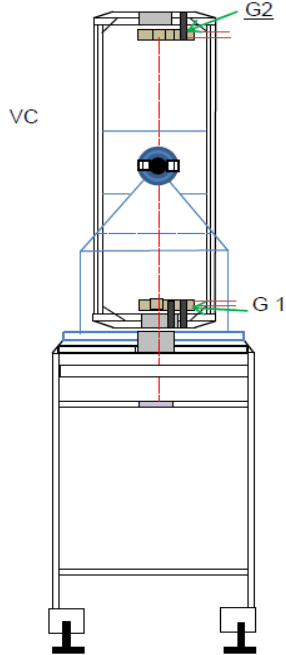
VCP1	(Intermediate Position IVCP)	VCP2
		
<p>Description</p> <ul style="list-style-type: none"> • Gripper 1 at the top • Gripper 2 at the bottom 	<p>Description</p> <ul style="list-style-type: none"> • Changing the position of the vacuum chamber between VCP1 and VCP2 • Interchanging positions of G1 and G2. 	<p>Description</p> <ul style="list-style-type: none"> • Gripper 1 is at bottom position • Gripper 2 is at top position

Figure B-1: Vacuum chamber positions

Positions in Figure B-1 define the states of the two grippers and vacuum chamber provided in Table B-1 above. The rotation movement is provided by a pneumatic piston with a rack and pinion of the design discussed in Section 3.2.2 to convert linear piston motion to rotary vacuum chamber movement.

Gripper's positions and movements

The pneumatic grippers are used in the design of this gravimeter for launching, capturing and aligning of the test mass. Most sensors used for pneumatic actuators for position detection are magnetic sensors. These sensors enable close loop controls systems which offer great advantages over open loop control systems. NMISA DFFG-01 is designed with open loop control positioning method. The design was simplified so it can be operational with this method. The decision also supports the removal of magnetic fields errors which contributed to uncertainty budget in IMGC-01 and IMGC-02 (D'Agostin, 2008).

Grippers used in the vacuum chamber are conceptualised to attain three defined stop positions during operation. The three positions are designed comprising two internal extreme cylinder boundaries represented by A and B on Figure 3-1 in Section 3.2.1 and one external mechanical hard stop to provide a defined piston position between the two extremes A and B. The gripper positions are discussed in operation with test mass on the gripper and without the test mass on the gripper.

Consider at the start of the process vacuum chamber is at position VCP_1 .

Operation process initiates

Step 1: represent moment when test mass is held by Gripper 1, this position is shown by T_0 in Figure B-3 below. The moment when the test mass is in the jaws of Gripper 1, gripper 2 is at position B_1 shown in Figure B-2. After the release of the test mass by Gripper 1, test mass undergoes free fall and drop into gripper 2. At the instant of release of the test mass, Gripper 1 goes to position B_2 , shown in Figure B-2.

Step 2: at the instant when the test mass reaches Gripper 2, the test mass is gently arrested to stop and the position of Gripper 2 becomes T_1 .

Step 3: Gripper 2 closes the grip to tight hold the test mass, moving from position T_1 to position T_0 . Whilst Gripper 1 closes, it moves from position B_2 to B_0 .

Step 4: The position of the vacuum chamber changes from VCP_1 to VCP_2 –rotary actuator is used to change the positions between VCP_1 and VCP_2 . After 180 degree rotation angle

[CW], vacuum chamber is at VCP_2 . When VCP_2 is reached, gripper 1 moves from position B_0 to B_1 .

Step 5: Changing from VCP_1 to VCP_2 changes the position of the grippers, their functions also swaps with positions changing (Step 5)

Step 6: Gripper 2 releases the test mass, with Gripper 2 position changing from T_0 to B_2 at the instant of release (Step 1)

Step 7: at the instant when the test mass reaches Gripper 1, the test mass is arrested gently to stop and the position of Gripper 1 becomes T_1 (Step 2).

Step 8: Gripper 1 closes the grip to hold tight to the test mass, moving from position T_1 to T_0 . Gripper 2 closes, moving from position B_2 to B_0 (Step 3)

Step 9: the position of the vacuum chamber changes from VCP_2 to VCP_1 . After 180 degree rotation angle [CCW], vacuum chamber is at VCP_1 . When VCP_1 is reached, Gripper 2 moves from position B_0 to B_1 .

After step 9 the system repeats the steps from 1 till 9, this becomes measurement process. The positions are schematically represented in following paragraph.

Gripper positions and movement without test mass

Position description

Both grippers G_1 and G_2 attain identical positions during manoeuvring of the gravimeter. The gripper positions are indicated in Figure B-2 for gripper without test mass and Figure B-3 for the gripper with test mass.

Gripper positions without the test mass

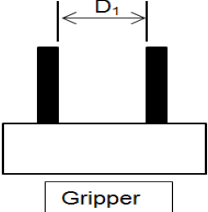
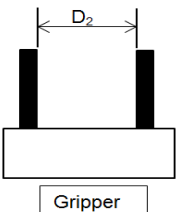
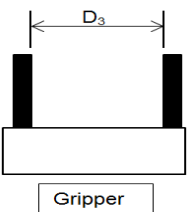
	Positions		
Without Test Mass			
Representation	B0	B1	B2

Figure B-2: Positions of the grippers without test mass

Table B-2 and Table B-4 give representation of the positions of the grippers provided in Figure B-2 and Figure B-3 respectively. These two tables assign the representation names to each position on each gripper.

Table B-2: Position of Gripper 1 and 2 without test mass representation symbols

Position Description	Representation	Gripper 1 [G1]	Gripper 2 [G2]
Closed	B0	G1B0	G2B0
Intermediate	B1	G1B1	G2B1
Opened	B2	G1B2	G2B2

Manoeuvring sequence

The movement of grippers as described above in this section involves steps which occur repeatedly during experiments process of automation, all possible movement of the grippers are indicated. These movements are given in Table B-3 for gripper without test mass and in Table B-5 for gripper with test mass.

Table B-3 : Movement sequence of grippers without test mass

Description of gripper movement	Representation
From B0 to B1	GB01
From B0 to B2	GB02
From B1 to B0	GB10
From B1to B2	GB12
From B2 to B0	GB20
From B2 to B1	GB21

Gripper positions and movement with test mass

Gripper positions with test mass.

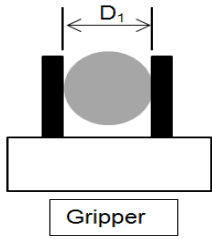
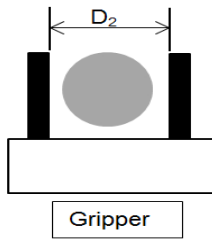
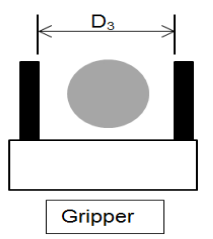
	Position		
With Test Mass			
Representation	T0	T1	T2

Figure B-3: Positions of the grippers with test mass

Positions of Gripper 1 and 2 with test mass on the jaws

Table B-4: Position of Gripper 1 and 2 with test mass representation symbols

Position Description	Representation	Gripper 1 [G1] Rep	Gripper 2[G2] Rep
Tight Grip	T0	G1T0	G2T0
Gentle Grip	T1	G1T1	G2T1
Release Grip	T2	G1T2	G2T2

The possible sequential movements of the grippers from position to position with test mass.

Table B-5: Movement sequence of grippers without test mass

Description of gripper movement	Representation
From T0 to T1	GM01
From T0 to T2	GM02
From T1 to T0	GM10
From T1 to T2	GM12
From T2 to T0	GM20
From T2 to T1	GM21

Intermediate external stoppers

The gripper positions are conceptualized to have three defined state stop positions, it is shown that two of these positions are provided by working cylinder boundaries and one is provided by external mechanical stoppers. This section explains the method used as external stoppers. The external stoppers provides the grippers with stopper to enable attainment of positions B_1 and T_1 indicated in Figure B-2 and Figure B-3 respectively during operations. Positions (T_0 and B_0) and (T_2 and B_2) are attained when the gripper working piston is at position A or B respectively. Positions (T_1 and B_1) are achievable when the intermediate stoppers are activated.

This method uses a mechanically guided stopper that uses weight to activate and deactivate the obstructing stoppers. Parallel grippers used in the design consist of two jaws individually, the intermediate stoppers are placed on each jaw, two stoppers at each gripper operating in identical manner. Table B-6 below gives the symbolic representation of the state position of obstructing knobs in the vacuum chamber.

Table B-6: State representation of mechanical knobs for each gripper

Obstructing knobs description	Representation symbol		State of the mechanical knobs	Representation symbol
Gripper 1 stoppers	MK1		Activated	A
Gripper 2 stoppers	MK2	Deactivated	DA	

In Figure B-1 above, vacuum chamber positions are represented as VCP_1 and VCP_2 . At position VCP_1 , Gripper 1 and Gripper 2 mechanical hard stoppers attains [B] and [C] respectively as represented in Figure B-4. At position VCP_2 , Gripper 1 and Gripper 2 mechanical hard stoppers attains [C] and [B] respectively.

Knobs achieve intermediate position by obstructing the path of the gripper jaws externally. This obstruction courses the working piston of the gripper cylinder to stop between the positions A and B indicated in Figure 3-6 of CHAPTER 3. The use of weight to activated hard mechanical knobs reduces the travel distance of the bottom gripper. At positions VCP_1 , G_1 travels between D_3 and D_1 with position D_3 corresponding to piston position B_1 and D_1 corresponding to piston position A in Figure 3-1.

G_2 travels between the D_1 and D_2 , with position D_2 corresponding to external stoppers knobs. At positions VCP_2 , G_2 travels between D_3 and D_1 . G_1 travels between the D_1 and D_2 . D_1 , D_2 and D_3 are position symbols names of the gripper jaws in the VC_1 .

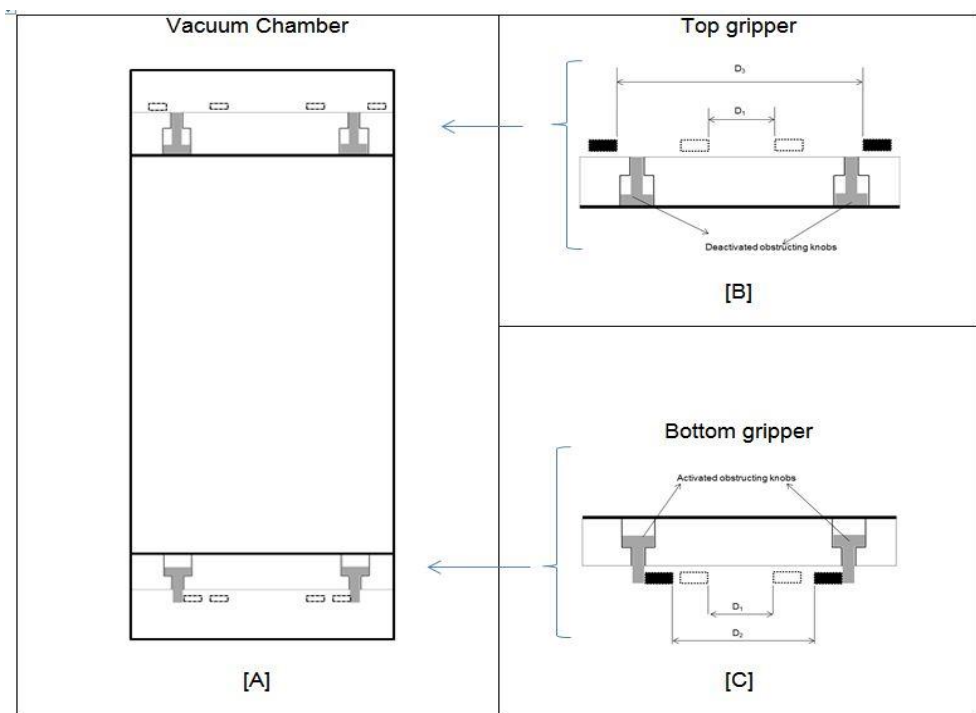


Figure B-4: A-Vacuum chamber, B- Deactivated knobs, and C- Activated knobs

The mechanical knobs attain similar positions interchangeably each time the vacuum chamber changes states from either VCP_1 or VCP_2 . Table B-7 provides a summary of the knobs state with vacuum position. Positions D_2 and D_3 are achievable during open stroke of the actuating piston and position D_1 is achieved during close stroke.

Table B-7: Position of the vacuum chamber and state of the mechanical knobs

Knobs state	Vacuum chamber position	
	VCP1	VCP2
MK1	DA	A
MK2	A	DA

The mechanical automation procedure for the vacuum chamber is discussed in details

Automation and control procedure of the vacuum chamber system

The automation requirement of the vacuum chamber describes the movements and sequence of the movements that will allow the system to function under continuous logical operations by halt process.

Starting position

- VCP₁ with test mass in G₂
- G₁ is at position G₁B₀ (Initialising)
- G₂ is at Position G₂T₀ (Initialising)

Automation process start

Setting up process [AA]

G₁ is at position G₁B₀

Repositioning of the test mass [AA] by initial vacuum chamber rotation

- VC rotates CW from VCP₁ to VCP₂
- G₂ is at position G₂T₀

Mechanical knobs

Instant when VCP₂ is reached

- MK₁ activates and MK₂ deactivates.

Projectile launch

Positioning G₁ for capturing position

- G₁ moves GB₀₁ (#Intermediate position)

Launching test mass from G₂

- G₂ moves GM₀₂ (#Launching the test mass)

The test mass falls gradually in to G₁, G₁ becomes G₁T₁.after the test mass has been stopped.

G₁ tight grips the test mass

- G₁ moves GM₁₀ (#Tight gripping the test mass)

G₂ Moves to prepare for next capturing

- G₂ moves GB₂₀ (#Closed position)

Repositioning the test mass [BB]

- VC rotates CCW from VCP₂ to VCP₁
- G₁ is at position G₁T₀

Mechanical knobs

Instant when VCP₁ is reached.

- MK₁ deactivates and MK₂ activates.

Projectile launch

Positioning G₂ for Capturing Position

- G₂ moves GB₀₁ (#Intermediate position)

Launching Test mass from G₁

- G₁ moves GM₀₂ (#Launching the test mass)

The test mass falls gradually in to G₂, G₂ goes to position G₂T₁

G₂ Tight grips the test mass

- G₂ moves GM₁₀ (#Tight gripping the test mass)

G₁ Moves to prepare for next capturing

- G₁ moves GB₂₀ (#Closed position)

The process occurs interchangeably between [AA] and [BB] for automated design

.

Appendix C

Pneumatic actuators

Actuating mechanism selection process

The current development of gravimeter uses the vacuum chamber as a method to reposition the test mass by rotation. The ability of the rotary actuator to rotate the load (Torque required) depends on the time taken to rotate from VCP₁ to VCP₂.

The table below indicates the relationship between time, angular acceleration, angular velocity and torque. Figure B-1 above indicates the two positions of the vacuum chamber, and the IVCP is the instant of high angular and angular acceleration. The vacuum chamber covers the angular displacement θ of 180° (π rad) from/to position VCP₁ to/from VCP₂. The angular velocity ω and angular acceleration α of the vacuum chamber is calculated using the equations below respectively:

$$\begin{aligned} \text{Angular velocity [rad/s]} \\ \omega = \frac{\Delta\theta}{\Delta t} \end{aligned}$$

$$\begin{aligned} \text{Angular acceleration [rad/s}^2\text{]} \\ \alpha = \frac{\Delta\omega}{\Delta t} \end{aligned}$$

The total mass of the vacuum chamber to be rotated is designed to be 20 Kg with 7 kg added for safety on calculation. This is to account for real world imperfections and bolts which were not include in the Solidworks model design. The center of mass of the vacuum chamber was calculated to be at 0.002 m from the axis of rotation of the vacuum chamber.

The calculated static torque T_s produced around the axis of rotation by weight of vacuum chamber at the center of mass is:

$$\begin{aligned} T_s = Wz &= 200 * 0.002 \\ &= 0.4 \text{ Nm} \end{aligned}$$

The theoretical principle moment of initial is calculated using the following equation

$$I_x = \frac{T_x}{\alpha_x}$$

Table C-1 below indicates the results of angular velocity, angular acceleration and moment of initial.

Table C-1: Motion parameters of the vacuum chamber as a function of time

Time [s]	ω [rad/s]	α[rad/s²]	I_x [Kgm²]
VCP₁ to/from VCP₂			
0.5	6.283185	12.56637	0.031831
1	3.141592	3.141592	0.127324
1.5	2.094395	1.396263	0.286479
2	1.590796	0.795398	0.502893
2.5	1.256637	0.502655	0.795774
3	1.047198	0.349065	1.145918

The moment of initial of the vacuum chamber about the rotating axis is defined a measure of vacuum chamber resistance to rotate. The principle of moment of principle moment of initial $P_{xx} = 0.09267 \text{ kg/m}^2$ calculated using Solidworks mode. The rotation time of the vacuum chamber can be anything from 1 second or higher. The required rotating movement of the chamber should be slow to avoid mechanical shocks of rotary actuator with high impacts of the piston boundaries.

The selection of the rotary actuator for the position of the vacuum chamber is based on maximum torque the actuator can produce and the allowable mass moment of initial from the actuator output shaft. The model DRRD-25-180-FH-Y9A double actuated semi-rotatory actuator is used with theoretical torque output of 5.1 Nm and Moment of inertia of 0.15 Kgm².

Appendix D

Systematic development results

Atmospheric pressure results

The prototype was first tested in the atmospheric pressure and reports the results of experimental drops performed on the system during day time with the isolation system and without isolation system installed.

Table D-1: Gravitational acceleration measurements drops performed in the atmospheric pressure during the day time without the isolation system

Gravimeter operating conditions				
Operating pressure [Pa]		100000 (Atmospheric pressure)		
Time of the day		Day time		
Set	Number of drops	Measured g [m/s²]	Standard deviation [m/s²]	Average Error
1	20	9.7831	0.0044	1.74x10 ⁻⁵
2	20	9.7803	0.0028	2.99x10 ⁻⁴
3	20	9.7801	0.0069	3.20x10 ⁻⁴
4	20	9.7771	0.0026	6.28x10 ⁻⁴
5	19	9.7836	0.0039	3.46x10 ⁻⁵
6	20	9.7803	0.0028	2.99x10 ⁻⁴
7	15	9.7851	0.0052	1.85x10 ⁻⁴
8	20	9.7769	0.0028	6.55x10 ⁻⁴
9	14	9.7822	0.0032	1.08x10 ⁻⁴
10	13	9.7799	0.0021	3.40x10 ⁻⁴
11	13	9.7831	0.0026	1.77x10 ⁻⁵
12	15	9.7831	0.0039	1.27x10 ⁻⁵
13	17	9.7907	0.0032	7.59x10 ⁻⁴
14	10	9.7868	0.0059	3.63x10 ⁻⁴
15	17	9.7892	0.0034	6.11x10 ⁻⁴
16	20	9.7846	0.0034	1.34x10 ⁻⁴
17	20	9.7837	0.0031	4.51x10 ⁻⁵
18	20	9.7830	0.0033	3.22x10 ⁻⁵
19	20	9.7839	0.0032	6.62x10 ⁻⁵
20	20	9.7827	0.0025	6.17x10 ⁻⁵
21	9	9.7817	0.0021	1.63x10 ⁻⁴
22	20	9.7840	0.0030	7.91x10 ⁻⁵
23	20	9.7842	0.0031	9.20x10 ⁻⁵
24	20	9.7845	0.0038	1.27x10 ⁻⁴
25	19	9.7842	0.0035	9.72x10 ⁻⁵
Inclusive average [m/s ²]		9.7833	0.0011	2.13x10 ⁻⁴
Set average standard deviation [m/s ²]			0.0029	
$g = 9.7833 \pm 0.0029 \text{ m/s}^2$				

Table D-2: Gravitational acceleration measurements experimental drops performed in the atmospheric pressure during day time with solation system

Gravimeter operating conditions				
Operating pressure [Pa]		100000 (Atmospheric pressure)		
Time of the day		Day time		
Set	Number of drops	Measured g [m/s²]	Standard deviation [m/s²]	Average Error
1	20	9.783247	0.00286	2.22x10 ⁻⁵
2	20	9.782797	0.00226	6.81x10 ⁻⁵
3	19	9.783346	0.00200	1.20x10 ⁻⁵
4	20	9.783313	0.00223	1.54x10 ⁻⁵
5	17	9.783924	0.00202	4.69x10 ⁻⁵
6	16	9.782324	0.00238	1.16x10 ⁻⁵
7	17	9.782685	0.00201	7.97x10 ⁻⁵
8	17	9.783008	0.00257	4.66x10 ⁻⁵
9	18	9.783513	0.00292	4.90x10 ⁻⁶
10	15	9.784144	0.00263	6.94x10 ⁻⁵
11	17	9.784301	0.00264	8.54x10 ⁻⁵
12	20	9.784574	0.00227	1.13x10 ⁻⁴
13	14	9.783863	0.00236	4.07x10 ⁻⁵
14	20	9.785042	0.00343	1.12x10 ⁻⁴
15	20	9.783882	0.00271	5.72x10 ⁻⁶
16	20	9.783919	0.00337	2.26x10 ⁻⁶
17	20	9.784319	0.00264	3.86x10 ⁻⁵
18	20	9.785846	0.00399	1.94x10 ⁻⁴
19	20	9.784591	0.00323	6.64x10 ⁻⁵
20	20	9.784525	0.00350	5.96x10 ⁻⁵
21	20	9.784776	0.00259	8.53x10 ⁻⁵
22	20	9.783775	0.00330	1.69x10 ⁻⁵
23	20	9.782924	0.00198	1.03x10 ⁻⁴
24	20	9.783850	0.00218	9.28x10 ⁻⁶
25	20	9.783152	0.00293	8.06x10 ⁻⁵
26	20	9.784472	0.00296	5.42x10 ⁻⁵
27	20	9.784528	0.00272	5.99x10 ⁻⁵
28	20	9.785121	0.00346	1.20x10 ⁻⁴
29	20	9.784379	0.00330	4.47x10 ⁻⁵
30	20	9.784079	0.00397	1.41x10 ⁻⁵
Inclusive average [m/s ²]		9.78394	0.002785	6.49x10 ⁻⁵
Set average standard deviation [m/s ²]		0.00079		
g = 9.78394 ± 0.00079 m/s²				

The measurements were accomplished at night time to evaluate the vibrations induced by human factors.

Table D-3: Gravitational acceleration measurements experimental drops performed in the atmospheric pressure during night time with solation system

Gravimeter operating conditions				
Operating pressure [Pa]		1000000		
Time of the day		Night time		
Set	Number of drops	Measured g [m/s²]	Standard deviation [m/s²]	Average Error
1	20	9.78194	0.00336	5.88x10 ⁻⁶
2	20	9.78125	0.00225	7.61x10 ⁻⁵
3	20	9.78184	0.00290	1.60x10 ⁻⁵
4	20	9.78153	0.00295	4.72x10 ⁻⁵
5	20	9.78418	0.00569	2.23x10 ⁻⁴
6	20	9.78168	0.00312	3.22x10 ⁻⁵
7	20	9.78141	0.00190	6.01x10 ⁻⁵
8	20	9.78128	0.00301	7.28x10 ⁻⁵
9	20	9.78169	0.00236	3.16x10 ⁻⁵
10	20	9.78236	0.00446	3.70x10 ⁻⁵
11	20	9.78309	0.00560	1.11x10 ⁻⁴
12	20	9.78101	0.00265	1.01x10 ⁻⁴
13	20	9.78233	0.00294	3.44x10 ⁻⁵
14	20	9.78175	0.00273	2.47x10 ⁻⁵
15	20	9.78153	0.00229	4.79x10 ⁻⁵
16	20	9.78229	0.00322	3.03x10 ⁻⁵
17	20	9.78184	0.00153	1.64x10 ⁻⁵
18	20	9.78191	0.00297	8.99x10 ⁻⁶
19	18	9.78357	0.00383	1.61x10 ⁻⁴
20	20	9.78245	0.00429	4.62x10 ⁻⁵
Inclusive average [m/s ²]		9.78200	0.00322	5.857x10 ⁻⁵
Set average standard deviation [m/s ²]		0.00076		
$g = 9.78200 \pm 0.00076 \text{ m/s}^2$				